AN ABSTRACT OF THE THESIS OF

Linda Engelbrecht for the degree of Doctor of Philosophy in
Electrical and Computer Engineering presented on March 18, 2011.

Title:
Modeling Spintronics Devices in Verilog-A for use with Industry-Standard Simulation Tools

Abstract approved: _____

Albrecht Jander

As the semiconductor industry works to integrate increasingly more "non-CMOS" devices onto CMOS ICs, compact model development has become an important step in the circuit/system verification tool flow. This research focuses on the two- and three-dimensional modeling of the physical phenomena that occur in nanoscale magnetic devices. This includes the continuous time dynamics of the changing magnetization state in magnetic thin film spintronic devices such as GMR spin valves, toggle MRAM bits and magnetic tunnel junctions (MTJs). The various torques responsible for magnetization change are modeled in Verilog-A modules and have been simulated for several static and dynamic cases. Device behavior is verified using current-in-plane Oersted fields and current-perpendicular-to-plane, spin transfer torque (STT) as stimulus. All device compact models have electrical I/O and are being developed to provide accurate device terminal behavior when used in a circuit simulation environment with standard CMOS circuits.

Modeling Spintronics Devices in Verilog-A for use with Industry-Standard Simulation Tools

by

Linda Engelbrecht

A THESIS

submitted to

Oregon State University

in partial fulfillment of
the requirements for the
degree of

Doctor of Philosophy

Presented March 18, 2011
Commencement June 2011

Doctor of Philosophy thesis of Linda Engelbrecht presented on March 18, 2011.

APPROVED:

Major Professor, representing Electrical and Computer Engineering

---

Director of the School of Electrical Engineering and Computer Science

---

Dean of the Graduate School

I understand that my thesis will become part of the permanent collection of Oregon State University libraries. My signature below authorizes release of my thesis to any reader upon request.

Linda Engelbrecht, Author

ACKNOWLEDGEMENTS

Magnetics is a strange and wonderful subject, but not an easy one to grasp. I would like to thank Dr. Albrecht Jander and Dr. Pallavi Dhagat for their knowledge, , helpful criticisms, their insistence on precision and quality, and most of all, for their patience.

TABLE OF CONTENTS

Page

1 Introduction 1

1.1 Literature review . . . 2

1.2 Spintronic devices . . . 5

1.2.1 Spin valve . . . 6

1.2.2 Toggle MRAM . . . 7

1.2.3 Spin transfer torque (STT) devices . . . 9

1.2.4 Summary . . . 12

2 Magnetic properties and phenomena 13

2.1 Magnetic moment and magnetization . . . 13

2.2 Anisotropy . . . 14

2.2.1 Magnetocrystalline anisotropy . . . 14

2.2.2 Shape anisotropy . . . 15

2.3 Exchange . . . 17

2.3.1 Exchange bias . . . 18

2.3.2 Interlayer exchange coupling . . . 20

2.4 Spin polarization . . . 22

2.5 Magnetoresistance . . . 23

2.5.1 Giant magnetoresistance (GMR) . . . 23

2.5.2 Tunneling magnetoresistance (TMR) . . . 25

2.5.2.1 TMR bias voltage dependence . . . 27

2.6 Dynamics . . . 27

2.6.1 Precession and precession frequency . . . 28

2.6.2 Spin relaxation or damping . . . 30

2.6.3 Spin transfer torque (STT) . . . 31

3 Materials and device considerations 36

3.1 General device/material geometries . . . 36

3.2 Antiferromagnetic materials . . . 37

3.3 Ferromagnetic materials . . . 38

3.4 Interlayer materials . . . 39

3.5 Summary . . . 40

TABLE OF CONTENTS (Continued)

Page

4 Effective fields and torques 41

4.1 Effective fields . . . 41
4.1.1 Relationship of torque to effective field . . . 42

4.2 Energy and torque for two-dimensional models . . . 43
4.2.1 Applied field . . . 43
4.2.2 Shape anisotropy . . . 44
4.2.3 Uniaxial crystalline anisotropy . . . 45
4.2.4 Effect of combined applied field and crystalline anisotropy . . . 46
4.2.5 Interlayer exchange coupling (IEC) . . . 46
4.2.6 Dipole coupling . . . 48

4.3 Two-dimensional magnetization dynamics . . . 50

4.4 Effective fields of three-dimensional systems . . . 53

4.5 Mathematical development of a three-dimensional system equation . . . 53

4.6 Energy and effective fields for three-dimensional models . . . 59
4.6.1 Uniaxial crystalline anisotropy . . . 60
4.6.2 Applied field or Zeeman energy . . . 62
4.6.3 Shape anisotropy . . . 63

4.7 Spin transfer torque (STT) . . . 64

4.8 The 3-D model . . . 67

5 Spin valve, toggle MRAM, and STT systems 69

5.1 Spin valve . . . 69
5.1.1 Quasi-static behavior . . . 70
5.1.2 The spin valve model . . . 71

5.2 Toggle MRAM . . . 74
5.2.1 Dynamic operation and response . . . 76
5.2.2 Model differences from the spin valve: TMR, dipole and exchange coupling 78

5.3 Spin transfer torque spin valve . . . 80
5.3.1 STT-driven magnetic reversal of spin valve free layer . . . 80
5.3.2 Steady-state precession using STT . . . 81

6 Simulating in Spectre/Spice 84
6.0.3 Verilog-A and magnetics . . . 85
6.0.4 Spectre/SPICE simulation . . . 87
6.0.4.1 Transient Analysis . . . 88

TABLE OF CONTENTS (Continued)

Page

6.0.4.2 The system solving algorithm: Newton-Raphson 89

7 Simulation results and discussion 92

7.1 2-D Spin valve 92
7.1.1 Transient simulations of the spin valve used as an MRAM cell 92
7.1.2 Hysteresis loops 95

7.2 2-D Toggle MRAM 96
7.2.1 Static response 97
7.2.2 Dynamic response 98
7.2.3 Hybrid spintronic-CMOS circuit 100

7.3 3-D Spin valve with Oersted field switching 102
7.3.1 Oersted field sustained precession 104
7.3.2 Applied field and uniaxial crystalline anisotropy 106
7.3.3 Easy axis not set to a principle axis 108
7.3.4 Including the shape anisotropy, $\mathbf{H_d}$ 110
7.3.5 3-D static and dynamic response 111

7.4 3-D Spin valve using spin transfer torque 114
7.4.1 Switching the FM free layer from AP to P with STT 117
7.4.2 Switching the FM free layer from P to AP with STT 119
7.4.3 Steady-state precession initiated with STT from AP state. 122

7.5 Model comparisons to published data 127
7.5.1 Magnetization reversal using Oersted fields 127
7.5.2 Magnetization reversal using an STT current 129

8 Conclusion 134

8.1 Appendix 1: Symbols used in manuscript 136

8.2 Appendix 2: Verilog-A module code 138

Bibliography 152

LIST OF FIGURES

Figure Page

1.1 a) Spin valve structure with electrical connections to conductors I_x and I_y creating fields in y and x respectively. Sensor readout is across rp and rn. b) Illustration of how free layer magnetization affects the output GMR signal: AP or antiparallel magnetization = high MR, P or parallel magnetization = low MR. 8

1.2 (a) Toggle MRAM bit cell with writeline conductors, and (b) a cross-point architecture for a bit cell array (the activated bit is shown in red). 10

1.3 Simplified spin transfer torque system 11

2.1 A spinning electron with angular momentum, $\mathbf{L_s}$, results in a spin magnetic moment $\mu_{m_{spin}}$. 14

2.2 Some examples of shape anisotropy. 16

2.3 *Bethe-Slater curve* showing the energy dependence of exchange interaction. a) Energy of combined atoms and their electrons with antiparallel or paired spins ($\uparrow\downarrow$) , or parallel spins ($\uparrow\uparrow$) vs. interatomic separation (r_{ij}). b) The energy difference proportional to the exchange constant plotted against r_{ij} normalized to the radius of a d-orbital, r_d. 18

2.4 Example hysteresis loop, M vs. H, for a pinned FM layer exchange coupled to an AFM layer. 19

2.5 Interlayer exchange coupling acting in Fe/Cr layers showing parallel ($\Delta R/R$ low) and antiparallel ($\Delta R/R$ high) layer magnetizations with Cr spacer thickness. [Reprinted figure with permission from S. Parkin, N. More, and K. Roche, Phys. Rev. Lett. Vol. 64, 2304 (1990). Copyright (1990) by the American Physical Society.] 21

2.6 Resistive paths and their combination for P and AP FM layers. The blue arrows indicate the magnetization (and the majority carrier) of the FM layer. R_1 represents the resistance seen by a spin-up(down) electron at the boundary of a layer with majority spin-up(down) carriers, and R_2, the resistance seen by a spin-up(down) electron at the boundary of a layer with the opposite spin majority carrier. . . . 24

LIST OF FIGURES (Continued)

Figure Page

2.7 Tunneling of electrons between electronic states (shown as DOS diagrams) in FM films 1 and 2. Spin-up (solid green arrow) and spin-down (dashed green arrow) conduction channels are shown being independent. With P magnetization majority spins tunnel to majority spin states and minority spins to minority spin states. For AP magnetization of the films, majority spins in film 1 become minority carriers in film 2 and tunnel to minority spin states in film 2. Minority spins in film 1 tunnel to majority spin states in film 2. 26

2.8 Magnetic precession. 29

2.9 Precession frequency 30

2.10 The action of damping described by the Gilbert damping torque. 31

2.11 A spin valve using spin transfer torque to switch the free layer magnetization from AP to P with the polarizing/pinned layer. Electrons with magnetization $\mathbf{m_p}$ are transported across the spacer layer due to the junction current I_s, and transfer their angular momentum to the free layer electrons at the spacer/free layer interface. The free layer will reverse its magnetization to be P with the polarizing/pinned layer with a sufficient I_s magnitude and pulse width. 33

2.12 The process of reversing the free layer moment from a P state. The majority electrons in the free layer (spin-up, $\uparrow$) find states in the pinned layer and are transmitted across the spacer with the electron flow (solid arrow). The minority electrons of the free layer are confined in the spacer and upon reflection at the spacer/FM interfaces, transfer spin torque back to the both layers (dotted lines). When the magnitude and pulse width of I_s is great enough, the free layer's minority electrons will transfer enough angular momentum to switch the free layer AP to the polarizing layer. 33

2.13 The effect of STT on magnetization trajectory. STT torque opposes damping torque and can increase the cone angle, θ, past 90° which will reverse the magnetization. Alternatively, the STT torque can balance with the damping torque causing the magnetic moment to undergo steady-state precession. 35

3.1 Spin valve with typical layer geometry 37

4.1 Uniaxial crystalline anisotropy torque present in a thin-film ferromagnetic layer. The uniaxial anisotropy causes two energy minima (upper graph) on the long or easy axis at 0° and 180°, while the torque (lower graph) is zero at the energy minima. 45

LIST OF FIGURES (Continued)

Figure | Page

4.2 Effect of an applied field combined with uniaxial anisotropy. The plots of the single-domain particle energy vs. θ_M under the indicated applied field conditions show that in zero field, the uniaxial anisotropy controls the magnetization of the film. With non-zero fields stable magnetization angles are found at local minima (θ_1 and θ_2), but with a large critical field applied, only one global minimum or stable magnetization ($\theta_1^{'}$) exists. 47

4.3 Ferromagnetic layers coupled by dipole fields $\mathbf{H_{12}}$ and $\mathbf{H_{21}}$ with parameters noted on each layer. The ellipsoidal layers illustrate the $\mathbf{H_{21}}$ field from layer 2 producing a torque on $\mathbf{M_1}$ 49

4.4 2-D effective damping in precessional dynamics. The precessional term is pushed out of the thin film plane, but the large out-of-plane demagnetizing field pulls it back in-plane in the direction of the damping. 51

4.5 Single model block containing all interaction equations for the 3-D device model. 54

4.6 Spherical coordinate system and angles: θ is the polar angle with respect to the **z**-axis, and φ is the azimuthal angle in the x-y plane. 54

4.7 Transfer of angular momentum from spin-polarized electrons to a FM layer magnetized antiparallel to the pinned layer. 65

5.1 Spin valve system with test connections and current inputs. 70

5.2 A Stoner-Wohlfarth hysteresis curve showing switching characteristics of a single domain magnetic particle; normalized magnetization against the applied field normalized to the coercive field, M/M_S vs. H/H_c. The green, square highlighted curve is for only $H = H_x$ applied ($H_y = 0$), the red dashed highlighted curve is for only $H = H_y$ applied ($H_x = 0$), and the gold highlighted curve is the case where $H = H_x + H_y$ and $H_x = H_y$. 72

5.3 Block diagram of the spin valve and its modules. 73

5.4 A Toggle MRAM bit. a) physical structure and b) model block diagram showing two free FM layers interacting via exchange and dipole coupling blocks. The output magnetoresistance is implemented with a magnetic tunnel junction between the bottom free layer and the pinned layer. 75

5.5 Toggling of the free layer magnetizations using a "box field" sequence. 77

5.6 Block diagram of an spin valve system using STT. $I_{spin}$is the injected CPP current. 80

LIST OF FIGURES (Continued)

Figure | Page

5.7 Phase diagram of spin transfer dynamics - for a fixed field H, a bistable region labeled A/B exhibits the A state when I is scanned from left to right, and the B state when I is scanned from right to left. Reference [17] has $10^8\,\mathrm{A/cm^2} \leftrightarrow 10\,\mathrm{mA}$. Green and red highlights have been added for clarity. [Reprinted figure with permission from J. Xiao, A. Zangwill, M. D. Stiles, Phys. Rev. B. Vol. 72, 014446 (2005). Copyright (2005) by the American Physical Society.] 82

6.1 Torques or Angular_Force as flow natures, summing at the torque balance node (θ_M) in the 2-D single domain block. θ_M is the block output and resultant moment angle which is a potential of the same discipline as the torques (rotational). . . . 87

6.2 A graphical representation of Newton's method. 90

7.1 a) 2-D spin valve block diagram and b) physical multilayer representation of block diagram in (a). 93

7.2 Spin valve simulated as an MRAM cell with word- and bit- line pulses. 94

7.3 Hysteresis curves for field applied along the easy axis (square loop), hard axis (diagonal - no hysteresis) and at a 45° to both axes (rounded loop). 95

7.4 Response of free layer moments (bottom and top free layers) in the toggle MRAM model in response to a 45° field ($H_x = H_y$). The spin flop transition and saturation fields are smaller for the r=0.2 attenuation case and larger for the r=0.7 case. . . 97

7.5 Hysteresis curve for the MRAM bit model stimulated by increasing and decreasing 45° field ($H_x = H_y$). P designates parallel moments in each layer, AP – anti-parallel, S – scissoring, → Hsf – going into spinflop field, → Hr – returning to AP state. 98

7.6 Response of the toggle MRAM model to three box field sequences with successively faster pulse edge timings: 2 ns, 300 ps and 50 ps. Circle figures at the top indicate directions of the free layer magnetizations at key time points in the sequence. The final pulse sequence fails to toggle the bit. 99

7.7 (a) Hybrid spintronic-CMOS schematic of the read/write circuit used to simulate a set of boxfield toggle sequences. The toggle MRAM symbol contains the model shown in the block diagram of (b). 101

LIST OF FIGURES (Continued)

Figure Page

7.8 Simulation results for the spintronic-CMOS read/write circuit. Three repeated toggle sequences are shown, and in each sequence the magnetic moments of the top and bottom layers switch to directions opposite their starting angle and switch 180°. opposite each other. The sense amplifier output, ‘‘Output”, is high for a high MR, and low for a low MR. The bias effect in the TMR module is enabled, consequently the TMR values are about 3% lower than with the bias effect disabled. 102

7.9 Spin valve cell using the 3D-single domain LLG block. 104

7.10 Top plot: 3-D xyz plot of sustained precession using applied field in the $\hat{\mathbf{z}}$ direction with easy axis set also in the $\hat{\mathbf{z}}$ direction (0, 0, 1); damping is set to zero. Bottom plot: H_z applied and the precession response of θ and φ over 4 precession cycles. 105

7.11 3D precession with applied field in the $\hat{\mathbf{y}}$ direction for (a) 50 ns, and (b) 100 ns, with easy axis set to the $\hat{\mathbf{x}}$ direction (1, 0, 0). In both (a) and (b), the magnetization dynamic in the xyz plot on the left, during the applied field pulse, is shown in green. The blue xyz curves occurs during the time that H_y=0. The H_y field pulse on the right is also shown in green. 107

7.12 Easy axis set to (1, 0, 1) and applied field in $\hat{\mathbf{y}}$ direction, then removed. the magnetization dynamic in the xyz plot on the left, during the applied field pulse, is shown in green. The blue xyz curve occurs during the time that H_y=0. The H_y field pulse on the right is also shown in green. 109

7.13 Comparison of applied field (a) $H_y < H_d + H_k$ and (b) $H_y > H_d + H_k$. 112

7.14 3-D magnetostatic response. The black square magnetization loop is due to a field in the $\hat{\mathbf{x}}$ axis, the blue diagonal line without hysteresis is the response to an applied field in the $\hat{\mathbf{y}}$ direction, and the curved, dashed red line shows the magnetization response to a field 45° to the easy axis. 113

7.15 3-D dynamic response with shape anisotropy included, H_k,$H_d \neq 0$. 115

7.16 3-D model dynamic response with $\alpha = 0.2$, but $H_d = 0$. 116

7.17 Spin valve block diagram using rp and rn ports to input spin current for STT simulation. 116

7.18 Spin valve layers with spin current (spin-polarizing electrons) originating from the polarizing layer, crossing to the NM spacer / free FM layer interface. 117

LIST OF FIGURES (Continued)

Figure Page

7.19 AP to P switching with I_s. Time domain graph (top) zoomed to switching region and 3-D xyz (bottom) plot. 118

7.20 Layers with spin-polarizing electron current from the FM free layer. 120

7.21 P to AP switching with I_s. 123

7.22 Conditions and setup for steady-state precession beginning in an AP state. . . . 124

7.23 Steady-state precession AP -> IPP, $I_s = 9\,\mu A$. 125

7.24 Steady-state precession AP -> IPP, $I_s = 11\,\mu A$. 126

7.25 Magnetization reversal (P to AP to P) experiments using parameters and fields of a reported physical device. (a) Reversal using a bias field along the easy axis ($\hat{\mathbf{x}}$ axis) of 4.8 $\left(\frac{\text{kA}}{\text{m}}\right)$, with a switching field of $H_x = -19.2$ $\left(\frac{\text{kA}}{\text{m}}\right)$ used to reverse $\mathbf{M}$ antiparallel. $H_y = 0$. After the 10 ns switching pulse, the positive H_x field must be raised to 7.65 $\left(\frac{\text{kA}}{\text{m}}\right)$ to get $\mathbf{M}$ to reverse again parallel with the easy axis, in the absence of a crystalline anisotropy field. The physical device switches back parallel without additional field. The vertical lines indicate approximate switching times, also reported in the accompanying table. (b) Reversal with a transverse field applied, H_y =1.4 $\left(\frac{\text{kA}}{\text{m}}\right)$. Switching times P to AP and AP to P are very similar. 130

7.26 Experimental and model simulation data of the switching frequency, $\frac{1}{\tau_s}$, in reversing the magnetization of a Co/Cu/Co nanopillar AP to P, using an STT current, I_s. 133

LIST OF TABLES

Table		Page
2.1	Exchange superlattices and their measured bilinear exchange coupling constant .	22
3.1	Antiferromagnetic layer materials	37
3.2	Soft ferromagnetic layer materials	39
3.3	Spacer and tunnel barrier materials	39
7.1	Fields and parameter values used for the 2D spin valve transient and hysteresis simulations.	93
7.2	Toggle MRAM bit cell; model parameters and variables	103
7.3	Field and parameter values used for the 3D spin valve transient simulation for sustained precession.	105
7.4	Field and parameter values used for the 3D spin valve transient simulation for testing uniaxial anisotropy.	106
7.5	Field and parameter values used for the 3D spin valve transient simulation for testing uniaxial anisotropy along a non-principle axis.	108
7.6	Field and parameter values used for the 3D spin valve transient simulation for testing uniaxial anisotropy.	110
7.7	Fields and parameter values used for the 2D spin valve transient and hysteresis simulations.	111
7.8	Field and parameter values used for the 3D spin valve using STT to reverse magnetization from AP to P.	119
7.9	Field and parameter values used for the 3D spin valve using STT to reverse magnetization from P to AP.	121
7.10	I_s and parameter values for a 3D spin valve using STT to operate in steady-state precession.	125
7.11	Field and parameter values from [1] used for the 3D spin valve dynamic switching comparison simulation.	128
7.12	Field and parameter values used for the 3D spin valve using STT to reverse magnetization from AP to P in Co/Cu/Co nanopillars.	131

DEDICATION

This work is for all my girls and my wonderful husband, but I dedicate it to Sarah, who trained me in patience and helped me to see that joy can be effortless.

Chapter 1 – Introduction

This thesis is concerned with the modeling of phenomena central to the operation of nanoscale magnetic devices or Spintronics. Spintronics is a relatively new area of electronics/magnetics engineering in which the spin (or angular momentum) of the electron in ferromagnetic materials plays a fundamental role. The signal is a magnetoresistance which depends on the relative orientation of the magnetic directions (moments) in adjacent ferromagnetic layers. The developed models are for important spintronic devices currently in production and for physical behaviors being actively investigated in these devices. The models of the physical behaviors are explained in the context of the devices and are modeled in the Verilog-A/MS behavioral language, a high-level language which is widely used within standard integrated circuit computer-aided design (ICCAD) software for analog and mixed-signal design simulation. The models developed in this work are targeted at a "macrospin" level, where it is assumed that the magnetization is uniform throughout a single magnetic layer and changes direction coherently. This assumption allows a simplified set of mathematical expressions for the various torques acting upon the magnetization and result in compact models accurately describing the device behavior. The goal has been to reach a viable three dimensional (3-D) continuous-time model of magnetization for a thin-film ferromagnetic layer subject to spin currents and magnetic fields. This goal has been achieved beginning with a two dimensional (2-D) approximation of the magnetization dynamics of a thin-film layer, progressed to include several inherent, basic device behaviors, and is now a 3-D model which includes both magnetostatic behaviors and magnetization dynamics. Compact models are behavioral components for use in circuit design and simulation with other spintronic elements and/or with charge-based devices. The developed models have been used in transient simulations with initial DC operating points. They are evaluated here using Spectre [2], the Cadence version of the prevalent SPICE circuit analysis program embedded in most ICCAD

design tools. The model results are qualitative and show correct functionality, without a critical quantitative comparison to current experimental data.

This work is motivated by the dearth of published spintronic device compact models for the electronics industry's use. Modern spin-based devices have been under development since the discovery of giant magnetoresistance (GMR) in ferromagnetic/non-magnetic (FM/NM) multilayers in 1988 [3, 4, 5], independently by Albert Fert and Peter Grunberg. They have been successfully used as sensors but with the exception of Magnetic Random Access Memory (MRAM) most spintronic devices are single discrete sensor components. As sensors, spintronic elements are already being used in a variety of technologies: automotive, airplane, and medical systems, and of course read heads in high density magnetic recording [6]. Without readily-usable standard simulator models, the integration of these spin-based devices in ICs will proceed more slowly. The models will help to promote hybrid CMOS-spintronic circuit design with contemporary devices and with spin-based logic elements in the future.

All symbols used in this thesis are defined with their units in Appendix 8.1. Système International (SI) units are used throughout, and vectors are represented by bold font such as $\mathbf{H}$. Unit vectors are represented in bold font with carets such as $\hat{\mathbf{j}}$.

1.1 Literature review

Modeling of spintronic devices has been growing rapidly in the past decade. This growth has been prompted by interest in making spin-logic and programmable spin-logic circuits with magnetic/magnetoresistive elements. Magnetoresistive-based circuits such as basic logic "gates" (nand, nor, etc...), full adders, field programmable logic devices, MRAM and other CMOS-magnetic hybrid architectures [7, 8, 9, 10, 11, 12, 13] were suggested or reported as implemented in the literature beginning around the year 2000, though Slonczewski had a vision of such devices as early as 1956 in his internal IBM paper on hysteresis (now published [14]). It is obvious from published results that several research groups had developed three dimensional, continuous time

models for magnetization dynamics [15, 16, 17], but these models are proprietary and the papers do not reveal what languages or simulator tools were used. Early modeling work to support spintronic elements and circuits has mostly consisted of quasi-static SPICE models which use electrically equivalent circuits and behave, for example, like the magnetoresistive junction. Some models are state-driven, such that when certain physics-based conditions are met, a magnetization change takes place. Das and Black described HSPICE models for spin valve structures made of subcircuits using voltage-controlled resistors, current sources, and voltage sources which displayed hysteresis in a field-driven device [18, 19]. This method was followed by a more detailed HSPICE macromodel which described a magnetic tunnel junction (MTJ) in [20]. In 2007, the SPINTEC laboratory introduced the results of C-compiled models (models not published) for MTJ-based devices for use in hybrid magnetic-CMOS circuits [13]. Recently (2010) Harms *et al.* has realized an electrically equivalent circuit in a state-driven SPICE macromodel of a magnetic tunnel junction which uses a spin-polarized current to transfer spin information to another ferromagnetic layer [21]. At the core of this model, a capacitor charged by a write current provides a decision circuit with the condition for which a magnetization reversal should take place.

The above SPICE model by Harms is considered a macromodel because it is written using already-exisiting HSPICE model components and does not need to be compiled as part of the simulator's HSPICE code. However, without modification, a model like the Harms macromodel is usable only in an HSPICE simulator. Verilog-HDL (high level description language) with the analog extension is prevalent in more simulator environments than HSPICE, but both are industry standards.

For non-electrical systems like spintronic devices, Verilog-A overcomes the greatest drawback of the SPICE component macromodel: Verilog-A uses physical equations to describe device behavior. It is a natural language which effectively decouples the model equations from the infrastructure necessary for implementation in analog simulators [22]. A set of model equations may contain only as much detail as needed to give an accurate account of the behavior of interest, and detail can be added or removed by simply changing the equations.

There are several behavioral models (Verilog-A/MS or VHDL-AMS, both high-level description languages for analog or mixed signal for use with ICCAD tools) that are state-driven, such as an early MTJ model in 2004 by Kammerer *et al.* [23] which made a magnetization reversal decision based on a graphical approach which stated when a switching threshold was crossed (Stoner-Wohlfarth method [14]). Zhao *et al.* [24] in 2006 reported simulation results of an MTJ model with physical parameters determining the tunnel barrier height and overall conductance of spin-polarized electrons between the two ferromagnetic layers depending on the parallel or antiparallel state of the layers. Also in 2006 an MRAM sensing scheme using an MTJ was proposed with the MTJ resistance modeled in VHDL-AMS [25]. Switching the tunneling magnetoresistance via spin transfer torque (STT) was added to two more recent physics-based MTJ models (simulation results only): a VHDL-AMS model by Madec *et al.* which is a continuous-time 3-D model [26], and a state-driven Verilog-A model with thermal effects added [27]. A new VHDL-AMS model description has been published as of June, 2010 [28] also by Madec, which contains a more complete physical description of the MTJ conductance channel. The code for this work is also not published, but the authors have indicated that the model is not in spherical coordinates, rather a cylindrical coordinate system, and requires renormalization of the magnetization magnitude with each simulation integration step. It does not yet include spin transfer torque or thermal effects, although they are pursuing these additions.

The 3-D continuous-time model to be presented as my work does not yet include thermal effects, or the bias-dependence of magnetic tunneling. The model provides approximate, but correct order-of-magnitude timing, field and current magnitudes. It is parameterized to allow changes in material properties. At present, all effective field equations (torques) controlling the 3-D model are contained in a single code module. It is simple to fold new torque expressions into this module, such as the MTJ conductance equation above, but it is a future goal to separate out certain torques into separate modules for flexibilty in combining them to make new devices.

1.2 Spintronic devices

The devices discussed here use materials that are ferromagnetic, paramagnetic and antiferromagnetic. A ferromagnetic material is one which exhibits spontaneous magnetization, that is, a net magnetic moment in the absence of an external magnetic field. Paramagnetic materials have a random magnetic moment ordering throughout the material resulting in zero net magnetization, but can be weakly magnetized in the presence of an external magnetic field. Paramagnetic materials are referred to here as non-magnetic. Antiferromagnetic materials exhibit magnetic moments alternating direction in adjacent molecular planes. The sum of all the moments balance so as to have zero net magnetization.

The thin-film ferromagnetic layers, non-magnetic layers and tunnel barriers which comprise the spintronic devices in this work are very small - on the order of 10^{-5} μm^3, and the FM films can have all of their magnetic moments or spin vectors align coherently in a single spin direction making that layer a "single domain." Thin layers of ferromagnetic materials are alternately stacked with non-magnetic or metal oxide insulator materials to form nanopillar-sized magnetoresistive devices. The magnitude of the magnetoresistive change depends on the combination of FM materials and interface or junction materials used, and how they are physically arranged and processed.

In many applications of spintronics the prominant architecture is that of the spin valve. In general the spin valve is a multilayer stack of materials designed and processed to fix the magnetic moment in one FM layer and allow another FM layer to change its magnetization with respect to the fixed layer moment. If an applied field is enough to reverse the magnetization of the free FM layer by 180°, the change in magnetization will create a significant change in the resistance. This magnetoresistive change is the device output signal.

Two other devices are discussed here, that use the physical phenomena of magnetoresistive change and are the toggle MRAM cell and the spin transfer torque (STT) devices. A toggle magnetic random access memory (Toggle MRAM) cell uses two free FM layers separated by a NM spacer but the two coupled layers are always nearly antiparallel in magnetization to one

another. The two layers respond to a field by having their combined magnetization or net moment point in the direction of the applied field. The toggle MRAM uses an insulator or tunnel barrier material to create its magnetoresistance. A spin transfer torque device is a spin valve but, instead of using an external applied field to change the free layer magnetization electrons spin-polarized by their layer's magnetization, transfer angular momentum to the free layer transported by a current perpendicular (CPP) to the thin-film ferromagnetic layers.

1.2.1 Spin valve

A basic spin valve consists of two ferromagnetic layers (FM) separated by a thin non-magnetic spacer layer (NM) as illustrated in Figure 1.1(a). The magnetization of the top FM layer is free to rotate in response to an applied magnetic field (free layer), while the bottom FM layer is held fixed by an adjacent "pinning" layer. The applied field is due to the combination of conductor currents I_x and I_y which can be bi-directional. The pinned layer is fixed in its magnetization by being exchange-biased with an adjacent antiferromagnet (AFM) layer. The magnetoresistance (MR) of the device depends on the relative orientation of the magnetic layers: lowest when the layers are magnetized in the same direction or parallel (P) and highest when magnetized oppositely or antiparallel (AP) as shown in (b). The P and AP states correspond to the resistance across the junction, R_P and R_{AP} respectively. The application of a current through the multilayer from rp to rn, allows the junction resistance to be read indirectly via the MR-generated voltage across the junction. The MR or GMR is proportional to $\cos(\theta_M - \theta_{Pinned})$ where θ_M and θ_{Pinned} are the angles of the magnetization in the free and pinned layers respectively [29]. The GMR ratio is defined most commonly in the literature as

$$GMR = \frac{R_{AP} - R_P}{R_P} = \frac{R_{max} - R_{min}}{R_{min}}\,.$$

The spin valve device typically has FM layers 10 nm - 50 nm thick with internal dimensions both between ~50 nm to ~150 nm in an ellipsoidal shape. The interface or spacer layer is 1 nm -

10 nm thick with a matching ellipsoidal area. The resistance through the multilayer is between 0.5 - 5 Ω. Devices that are constructed with a conductive (metallic), non-magnetic interface, usually copper (Cu) or ruthenium (Ru) spacer layers, generally yield a minimum 3%-8% change in GMR, up to a maxium of about 50%, depending on the combination of spacer and FM materials used. From 1990 until about 2000, a NM spacer layer was the defacto interface between the two FM layers for the creation of the GMR effect, but it has been shown that tunnel barriers, very thin (0.5 - 3 nm) layers of an insulating, dielectric material (I), can result in an even higher MR or tunneling magnetoresistance (TMR) [30, 31, 32]. This kind of interface is termed a magnetic tunnel junction (MTJ) and is also common in spin valve structures.

1.2.2 Toggle MRAM

Toggle MRAM is a chosen model target because of its innovative and successful magnetic switching method. It consists of a tunneling magnetoresistive memory element between a word and bit line. Magnetic fields to write the bit are applied to the element by passing a unidirectional current through the write lines as shown in Figure 1.2. The simplified structure in Figure 1.2 (a) illustrates that the magnetic element has three FM layers: a pinned magnetic layer in which the magnetization is fixed and two free layers in which the magnetization direction can be changed. The two free layers are coupled via the intermediate non-magnetic (for example, Cu or Ru) spacer, so that the magnetizations of the layers are opposite in orientation (antiparallel). The two free layers and their interfacing spacer layer are together called a synthetic antiferromagnet (SAF). Figure 1.2 (a) also shows that the easy axis of the multilayer bit is rotated 45° to both the writelines. Figure 1.2 (b) depicts how the bit cell is incorporated into an MRAM array and how the fields from the writeline currents affect the bits. Conventional MRAM does not use the SAF structure but has a single free layer, and the bits are not rotated. Unless the bits are spaced adequately, they are subject to write disturbance or half-select errors: the accidental writing of a bit on the same word or bit line as the full-selected bit at their intersection [33].

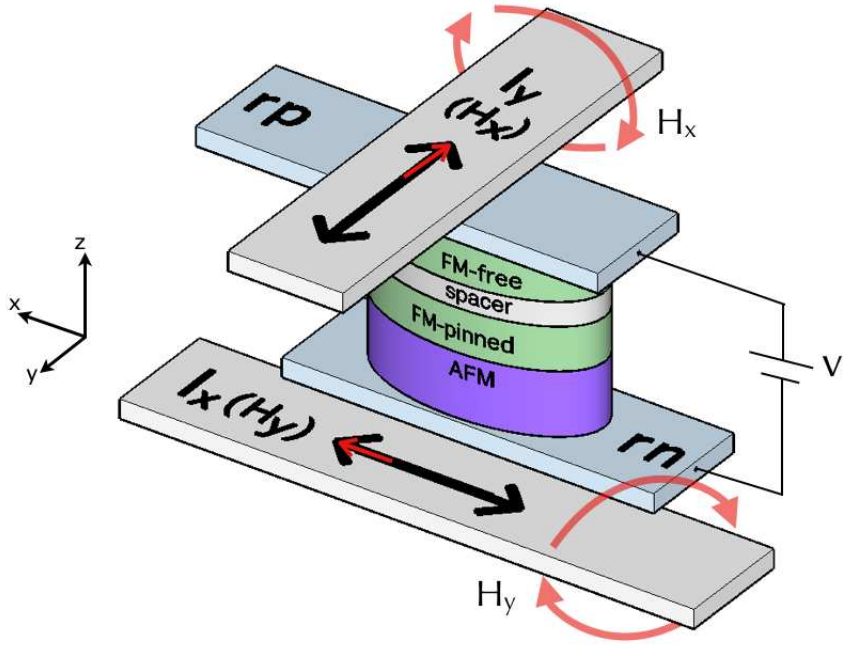

(a)

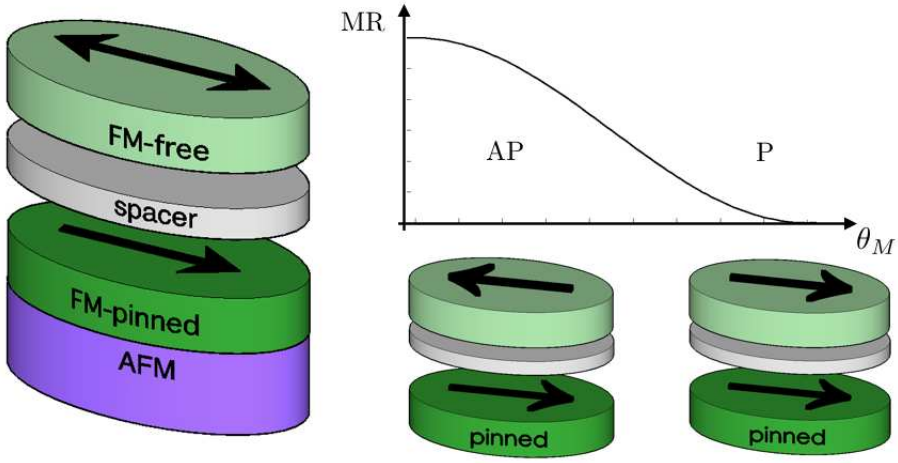

(b)

Figure 1.1: a) Spin valve structure with electrical connections to conductors I_x and I_y creating fields in y and x respectively. Sensor readout is across rp and rn. b) Illustration of how free layer magnetization affects the output GMR signal: AP or antiparallel magnetization = high MR, P or parallel magnetization = low MR.

In Toggle MRAM, this problem was solved by Savtchenko in 2002 [34]. He proposed the structure already described which allows the write operation to be a rotation of the moments of the balanced synthetic antiferromagnet (SAF), where "balanced" means the free FM layers have the same area and thickness. The SAF's two coupled magnetic elements are switched between two stable states using a specific sequence of magnetic field pulses from currents applied on orthogonal word and bit lines. This pulse sequence allows the layers' net moment to change by ~45° with each pulse edge. The toggle bit's susceptibility to half-select or write disturb errors is significantly reduced [35, 36, 37] compared to a spin valve.

The magnetic anisotropy of the bit is designed so that in the absence of write fields, the free layers are stable in either of two states: top layer at 45° and bottom layer at 225° or vice versa. A single bit of binary information is thus stored in the magnetization direction of the coupled free layers with respect to the pinned FM layer. The magnetoresistive signal is generated with a MTJ between the free and pinned layers.

The Toggle MRAM architecture allows the bit cells to be used in a higher density configuration than conventional MRAM, which means the area of a bit cell can be reduced to a minimal size with enough margin that it won't switch from thermal fluctuations. A higher density bit array still has an increased probability of falsely switching a target bit cell's nearest-neighbor via the writeline fields [33]. For this reason and the necessity for smaller switching currents, toggle MRAM and other GMR- or TMR-based devices are utilizing an even newer phenomenom termed Spin Transfer Torque (STT) .

1.2.3 Spin transfer torque (STT) devices

In the two previous devices, magnetic fields from currents (Oersted fields) in traces adjacent to the thin film FM layers are used to reorient the magnetization in the free FM layers. Spin transfer torque has the same result but arises from a current injected perpendicular to the plane of the thin film junction, transferring spin-polarized electrons (polarized in the $\hat{\mathbf{x}} = \hat{\mathbf{e_p}}$ direction) from a

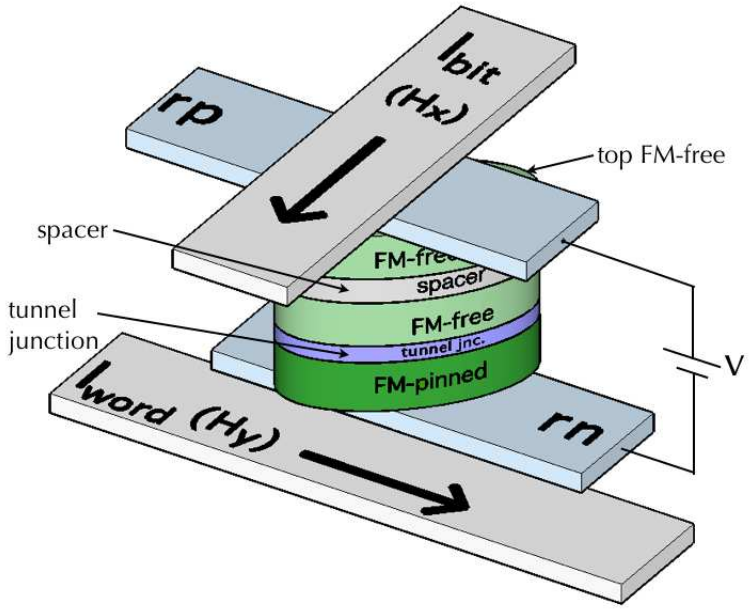

(a)

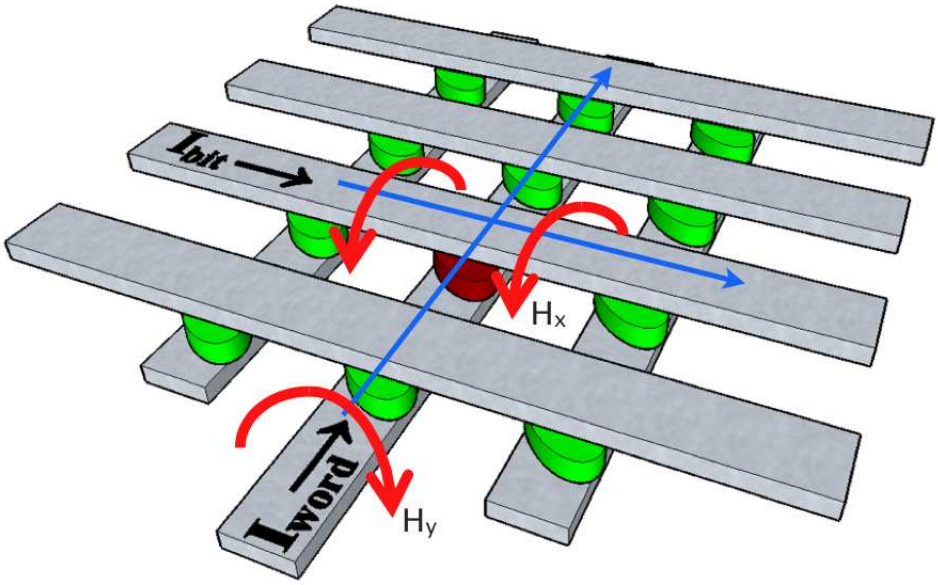

(b)

Figure 1.2: (a) Toggle MRAM bit cell with writeline conductors, and (b) a cross-point architecture for a bit cell array (the activated bit is shown in red).

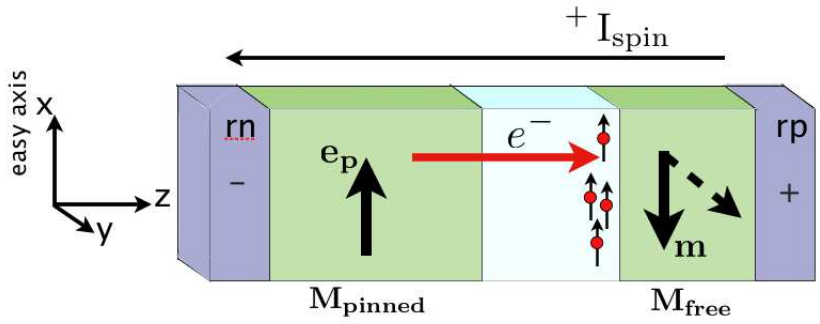

Figure 1.3: Simplified spin transfer torque system

FM source electrode to a receiving FM electrode through a non-magnetic spacer region as shown in Figure 1.3. The figure is representative of a spin valve in which the magnetization of the free layer, $\mathbf{m}$, is able to switch directions along the device easy axis ($\hat{\mathbf{x}}$) due to the electron flow (red arrow in the figure). If the voltage bias is positive with respect to the free layer (positive voltage on the free-layer contact), a conventional electrical current ($\mathrm{I_{spin}}$) will flow from the free layer to the pinned layer, and spin-polarized electrons from the pinned layer traverse the junction to the free layer (electron current) as shown. The electrical and electron currents will be in the reverse direction if the voltage bias is reversed, creating an electron flow that consists mostly of the majority spin (spin-polarization) in the free layer.

STT investigations have shown reliable switching of free layers in nanopillar spin valve structures [38, 39, 40, 41, 42], as well as operating in other modes such as microwave oscillators [43, 44, 45, 46]. The spin valve systems initially researched utilized non-magnetic spacer materials for the interlayer between the ferromagnetic electrodes, but attention has now turned to tunnel barrier materials which yield a significantly higher magnetoresistance (TMR) compared to GMR. One of the main advantages to using the STT switching method is that the magnitude of the electrical current needed to provide enough spin-polarized electrons for switching, is an order of magnitude less than current needed to create a large enough Oersted field for conventional switching $\left(10^6 \frac{\mathrm{A}}{cm^2}\right.$ vs. $\left.10^7 - 10^8 \frac{\mathrm{A}}{cm^2}\right)$. STT electrical currents are, at present, competitive with SRAM current/power usage [47] and the switching current density is expected to be further

reduced with materials that act as better electron spin-polarizers.

1.2.4 Summary

The devices introduced above, the spin valve, toggle MRAM, and the STT element are the basic elements of spintronics. They are all submicron, multilayer stacks of antiferromagnets (AFM), conductive non-magnetic metals, ferromagnetic metals (FM), and dielectric materials (I), but the interactions between the layers varies with their arrangement, and whether they are in the presence of current-in-plane (CIP) magnetic fields (Oersted fields) or spin-polarized current-perpendicular-to-plane (CPP) current. The magnetic phenomena relevant to the spintronic models are presented in the next chapter with a synopsis of the physics governing device behavior and interactions, and their mathematic descriptions as used in the models.

Chapter 2 – Magnetic properties and phenomena

2.1 Magnetic moment and magnetization

The magnetic moment, μ_m, is the fundamental object in magnetization. A magnetic solid consists of a large number of atoms each with a magnetic moment, $\mu_{m_{spin}}$, primarily due to the electron's spin. The atomic magnetic moments in nanoscale devices interact together as one "macrospin." The collective magnetic moment of an FM element is described by the vector $\mathbf{m}$ in $\left[\mathrm{Am}^2\right]$. The magnetic moment of a single electron is an expression of the angular momentum of that electron. We consider here only the intrinsic spin angular momentum, $\mathbf{L_s}$, of the electrons summarized in Figure 2.1, as this is the dominant angular momentum in ferromagnetic materials. The spin angular momentum reflects the two possible spin states $\pm\frac{1}{2}$ quantized by the reduced Planck's constant, $\hbar$. The ratio of the spin magnetic moment to the spin angular momentum is called the spin gyromagnetic ratio

$$\frac{\mu_{m_{spin}}}{\mathbf{L_s}} = \gamma_s \approx 1.76 \times 10^{11} \left(\frac{rad}{s \cdot \mathrm{T}}\right) \approx 28 \left(\frac{\mathrm{GHz}}{\mathrm{T}}\right) . \tag{2.1}$$

$\mu_{m_{spin}}$ is equal to $\pm\frac{\hbar e}{2m_e}$ which is frequently used and labeled as the Bohr magneton, μ_B [48]. The number of Bohr magnetons in a ferromagnetic atom or alloy can be computed which is useful as an approximation of the maximum magnetization magnitude. Since the (volume) magnetization of a sample is directly proportional to its magnetic moment, $\mathbf{M} = \frac{\mathbf{m}}{\mathbf{V}}$, it reveals that the magnetization of a sample is directly proportional to its angular momentum.

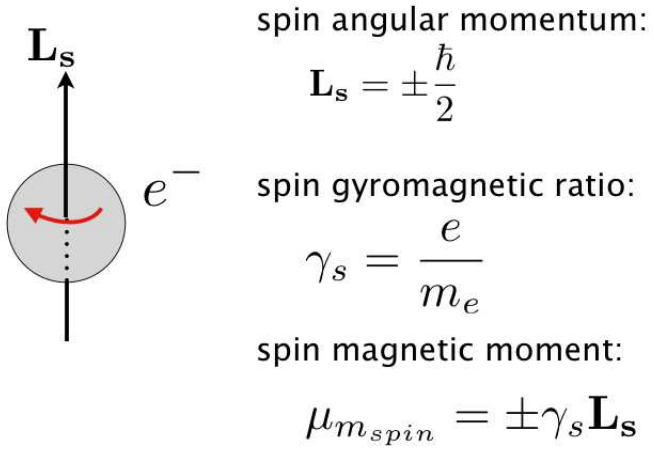

Figure 2.1: A spinning electron with angular momentum, $\mathbf{L_s}$, results in a spin magnetic moment $\mu_{m_{spin}}$.

2.2 Anisotropy

In a magnetic solid, anisotropy defines the direction which the magnetization will prefer because that direction results in a lower free energy. There are several sources of anisotropy which contribute to the net torque acting upon the magnetic moment. In thin magnetic films, the most significant anisotropy effects are those due to the crystalline structure of the material and the sample shape.

2.2.1 Magnetocrystalline anisotropy

The crystalline anisotropy of a magnetic solid is determined by the crystal's physical structure. The atoms in the crystal have a charge polarity, positive or negative, resulting in an electric field in the crystal. The crystal's electric field causes the atomic orbitals to align themselves on certain axes also aligning the magnetic moments in those same directions. The spin magnetic moments of the atoms have their direction confined to a crystal lattice direction by the crystal electric field, causing the magnetization to prefer that direction. This direction is called the anisotropy

axis or direction.

Magnetocrystalline anisotropy is described as uniaxial (along a single axis) or cubic (along a combination of the $\hat{\mathbf{x}}$, $\hat{\mathbf{y}}$, and $\hat{\mathbf{z}}$ directions). It is expressed as the free energy in a power series expansion for the following two cases [49], where θ is the angle of magnetization with respect to the anisotropy axis,

1. Uniaxial anisotropy: $E_k = V\left[K_{u1}sin^2\theta + K_{u2}sin^4\theta + \ldots + K_{un}sin^{2n}\theta\right]$ $(n = 1, 2, 3...)$. Normally $K_{u1} \gg K_{un}$ and it is sufficient to use only the quadratic term with K_{u1}.

2. Cubic anisotropy: $E_k = V\left[K_1(\alpha_1^2\,\alpha_2^2 + \alpha_2^2\,\alpha_3^2 + \alpha_3^2\,\alpha_1^2) + K_2(\alpha_1^2\,\alpha_2^2\,\alpha_3^2)\right]$, where the α_n s are direction cosines (unitless) equal to $\alpha_n = \frac{M_x}{M_S}$, $\frac{M_y}{M_S}$ and $\frac{M_z}{M_S}$.

The magnitude of the first- and 2nd order crystalline anisotropy constants (K_1 or K_{u1}, and K_2 or K_{u2}) for magnetic materials/alloys are in the range $10^2\,{}^{\mathrm{J}}/_{\mathrm{m}^3} \leq K \leq 10^5\,{}^{\mathrm{J}}/_{\mathrm{m}^3}$.

2.2.2 Shape anisotropy

Whenever magnetization creates magnetic poles along the surface of a solid, a field opposing that magnetization, called the demagnetization field, $\mathbf{H_d}$, is formed. Shape anisotropy originates with the demagnetization field and the energy of the anisotropy is

$$E_d = \frac{1}{2}\mu_0 V \mathbf{M}\mathbf{H_d} \tag{2.2}$$

$$= \frac{1}{2}\mu_0 V \mathbf{M}\,(-N\mathbf{M}) \tag{2.3}$$

where the factor of $\frac{1}{2}$ is due to the term being a type of self-energy, that is, the energy terms between magnetic particles are not counted twice. The shape anisotropy is defined as $\mathbf{H_d} = -N\mathbf{M}$. This definition shows that $\mathbf{H_d}$ is opposite $\mathbf{M}$ by a factor of N. N is a tensor of demagnetization factors for a specific shape; for an elliptical solid, N is a diagonal matrix with terms along the principle axes, N_x, N_y and N_z in which the sum of the demagnetization factors must add to 1.0. Some demagnetization factor examples are pictured in Figure 2.2. The demagnetization factors

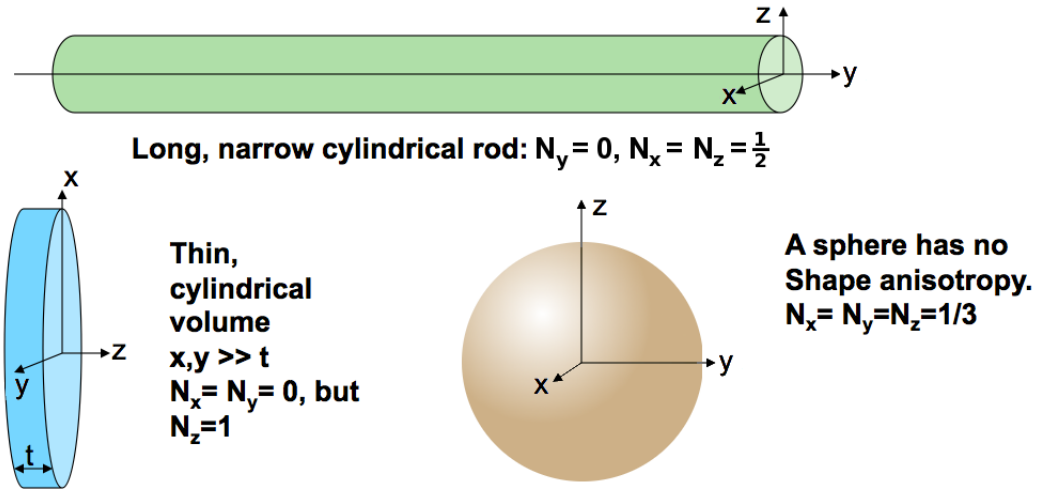

Figure 2.2: Some examples of shape anisotropy.

represent the strength of the field caused by the separation of magnetic charges along the axes. When magnetic charges are far apart as on the end surfaces (y-z planes) of the long cylindrical rod, separated by the length of the rod in the $\hat{\mathbf{x}}$-direction, the demagnetization factor, $N_x = 0$, and the demagnetization field is very weak or non-existent. The thin, cylindrical volume in the figure is representative of a flat ellipsoid such as one might have for a thin film magnetic layer; N_x and N_y , the in-plane demagnetization factors, would be very small - two to three orders of magnitude less than the $N_z \approx 1.0$ factor. In this case N_z for the direction perpendicular to the thin-film plane indicates that the magnetic charges on the surfaces of the x-y planes are very close together, generating a very strong demagnetization field.

The example of the thin cylindrical volume is appropriate for all models in this work. For a thin film magnetic layer, the energy of the shape anisotropy will be minimal when the layer is magnetized in the x-y plane, and at a maximum when magnetized perpendicular-to-the-plane in the $\hat{\mathbf{z}}$-direction. For situations where external fields are applied in the plane of the thin-film, the demagnetization factor of the longer or easy axis, will always be N_x in this document. Conversely, N_y will always refer to the demagnetization factor on the shorter or hard axis. Thus, $-N\mathbf{M} = -\left(N_x \mathrm{M_x}\hat{\mathbf{i}} + N_y \mathrm{M_y}\hat{\mathbf{j}}\right)$.

Shape anisotropy is significantly greater than the crystalline anisotropy having an energy magnitude on the order of 10^6 J/m^3, so a magnetic layer shape with a long axis would define the easy axis of magnetization if it were different from the easy axis of the crystalline lattice. This work always considers the easy axis due to the layer shape to be aligned with the crystallographic easy axis.

2.3 Exchange

Exchange interactions are responsible for both short-range (electron-electron on the same atom, or nearest neighbor atoms) and long-range magnetic order, that is, magnetic moments passed to atoms further away than the first or second nearest neighbor. Exchange can affect the spins of electrons across many atomic sites and even across nonmagnetic layers several nanometers thick. Exchange occurs in order to create the lowest energy configuration among electrons in molecular and atomic orbitals, trading off the energy cost of coulomb repulsion with the energy cost of parallel spins. The difference in energy between the parallel spin and the antiparallel (paired) spin configurations is the exchange energy.

The character of the exchange is denoted by its exchange integral or exchange constant, J_{ij}, which determines how the wavefunctions of two interacting particles combine. An illustration of this interaction in ferromagnetic metals is shown in Figure 2.3, the *Bethe-Slater curve* [50]. This curve shows that when interatomic distances (r_{ij}) are small, the atoms' electrons combine in an atomic orbital with lower energy if they have opposite or antiparallel spins - this is antiferromagnetic exchange. When the atoms are spaced further apart, their electrons combine in a larger orbital where there is a lower energy cost for the electrons to have parallel spin or ferromagnetic exchange.

This description covers only direct exchange between electrons on neighboring magnetic atoms, however the exchange constant for more indirect exchange interactions over larger distances still retains the same proportionality: the sign of the exchange constant indicates ferro-

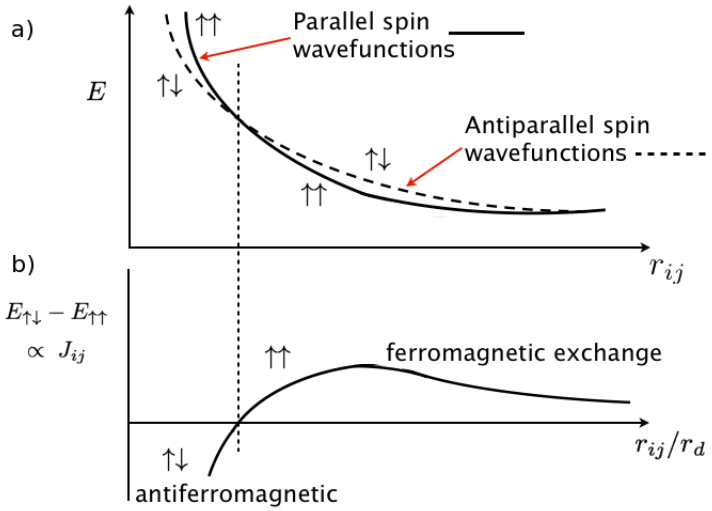

Figure 2.3: *Bethe-Slater curve* showing the energy dependence of exchange interaction. a) Energy of combined atoms and their electrons with antiparallel or paired spins (↑↓) , or parallel spins (↑↑) vs. interatomic separation (r_{ij}). b) The energy difference proportional to the exchange constant plotted against r_{ij} normalized to the radius of a d-orbital, r_d.

magnetic (parallel spin) coupling for $J_{ex} > 0$, and antiferromagnetic (antiparallel, paired spin) coupling for $J_{ex} < 0$, where J_{ex} will be used as a general exchange parameter for different exchange interactions. With this foundation two types of exchange that are specific to the devices modeled in this work are now covered. The first is due to a direct form of exchange called exchange anisotropy or exchange bias and the second exchange interaction is indirect and communicates spin information over a range of a few nanometers called interlayer exchange coupling (IEC).

2.3.1 Exchange bias

Exchange bias is the exchange coupling of interfacial spins between a FM and a AFM layer. This exchange is used to pin the direction of magnetization in the FM layer. The pinning process takes advantage of the temperature dependence of ferromagnetic and antiferromagnetic order specific to the materials. The Néel temperature, T_N, of the AFM materials is the temperature above

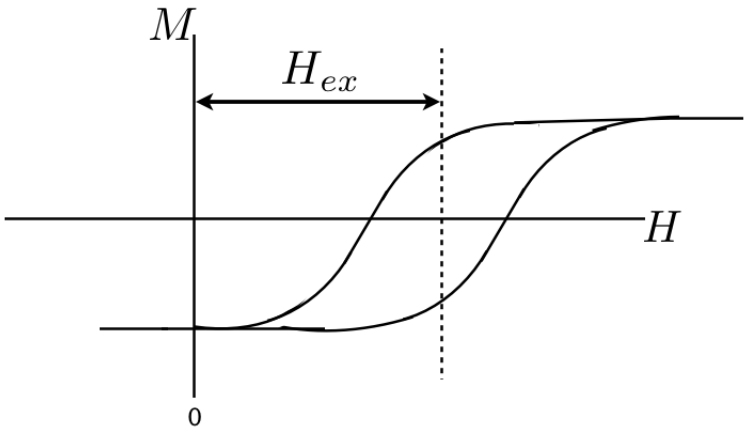

Figure 2.4: Example hysteresis loop, M vs. H, for a pinned FM layer exchange coupled to an AFM layer.

which the material no longer has antiferromagnetic order and becomes paramagnetic. Similarly, the Curie temperature, T_C, is the temperature above which the ferromagnetic materials become paramagnetic with random spin ordering. It is important that the materials have $T_N < T_C$ in order to be able to use the AFM material to pin the FM layer. Pinning is done after the deposition of the AFM and FM layers. The layers are heated above T_N but below T_C in the presence of an applied field, thus de-ordering the AFM layer and holding the FM layer magnetized in the direction of the applied field. The layers are then cooled below T_N with the field still present, and the AFM layer orders itself in a manner that minimizes its interaction energy with the FM layer at the interface [51]. The FM layer's magnetization is biased/pinned in the direction in which it was cooled and this becomes the preferred direction of magnetization.

The effect of the exchange biasing is to produce a unidirectional exchange field, $\mathbf{H_{ex}}$, which acts on the pinned FM layer like an external field. Thus, $\mathbf{H_{ex}}$ combines with an external applied field, $\mathbf{H}$, to shift the hysteresis loop of the pinned FM layer by the value of $\mathbf{H_{ex}}$ as shown in Figure 2.4.

2.3.2 Interlayer exchange coupling

Interlayer exchange coupling (IEC) is an indirect exchange interaction in which the electrons of a non-magnetic spacer material communicate the spin states of two FM layers. It has the interesting and important characteristic of alternating the sign of the coupling from positive to negative with the thickness of the non-magnetic spacer between the FM layers as shown in Figure 2.5 from Parkin's original Fe/Cr data [52]. Parkin's data illustrates the alternating coupling states with the change in the resistance across the FM/NM/FM junction; $\frac{\Delta R}{R}$ is low for parallel coupling of the layers, and high for antiparallel coupling. This characteristic allows the free FM layer, in the absence of an applied field, to be fixed in an AP or P magnetization state with respect to the pinned layer for a given interlayer thickness. The exchange is the transfer or reflection of spin-up (majority) electrons and/or spin-down (minority) electrons between the layers dependent on their spin and the magnetization of the layers. The exchange coupling causes the magnetization of the layers to alternate P to AP at a well-defined period of spacer thickness as the magnetic alignment of the ferromagnetic layers always takes the configuration that has thelowest energy cost. The periodic AP and P alignment of the FM layers cause the

alternating sign of the exchange constant (ferromagnetic coupling for $J_{ex} > 0$, and antiferromagnetic coupling for $J_{ex} < 0$). Since the electron reflection/scattering is spin dependent, there is an energy difference between the P and AP alignment of the FM layer magnetizations. This energy difference is the interlayer exchange coupling. The energy of the coupling has been characterized [53, 54] as

$$E_{exch} = -J_1 \cos\theta_{\mathrm{M}} - J_2 \cos\theta_{\mathrm{M}}^2 \,. \tag{2.4}$$

In equation 2.4, E_{exch} is an energy density (per unit area, A), and θ_M is the angle between the magnetizations of the FM layers. There are two exchange parameters indicated, J_1 or the bilinear exchange constant, so called because the energy per area is linear in the directions of both magnetizations ($-J_1 \cos\theta_{\mathrm{M}} = -J_1 \mathbf{m_1} \cdot \mathbf{m_2}$), and similarly, J_2 or biquadratic, because it is quadratic in both of the magnetization directions. All measured values of J_2 are negative, favoring

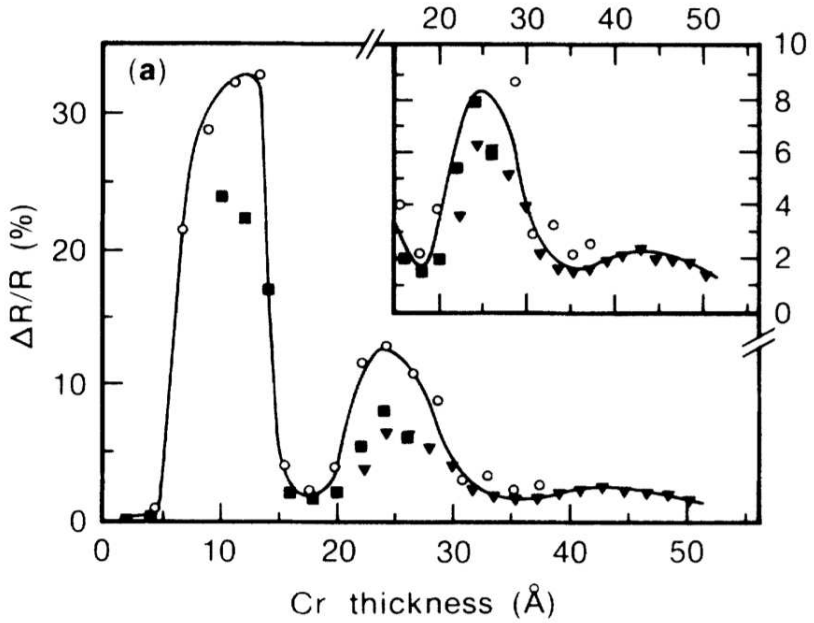

Figure 2.5: Interlayer exchange coupling acting in Fe/Cr layers showing parallel ($^{\Delta R}/_{R}$ low) and antiparallel ($^{\Delta R}/_{R}$ high) layer magnetizations with Cr spacer thickness. [Reprinted figure with permission from S. Parkin, N. More, and K. Roche, Phys. Rev. Lett. Vol. 64, 2304 (1990). Copyright (1990) by the American Physical Society.]

Exchange superlattice	Spacer thickness t_{sp} (nm)	Bilinear exchange coupling constant, J_1 ($\frac{J}{m^2}$)
Co/Ru/Co	0.6	6.0×10^{-3}
Co/Cu/Co (111)	0.85	1.1×10^{-3}
Co/Cu/Co (100)	1.2	4.0×10^{-4}
Co/Ru/NiFe	2.5	1.8×10^{-5}
NiFe/Cu/NiFe	2.1	1.2×10^{-6}

Table 2.1: Exchange superlattices and their measured bilinear exchange coupling constant

perpendicular orientation of the two magnetizations. In general, J_1 is more significant by an order of magnitude. The biquadratic term can not always be ignored, but it is due to smaller effects such as interface roughness. When J_1 is dominant and positive (negative), the magnetization coupling is ferromagnetic or parallel (antiferromagnetic or antiparallel). The strengths of J_1 and J_2 are dependent on the FM materials and the spacer thickness. Table 2.1 lists examples of layer structures commonly found in the literature and their measured value of the bilinear exchange term.

In this work the biquadratic, J_2 term is ignored as the interfaces are considered ideal. Generally, in spin valves and other devices with IEC-coupled layers, the coupling is designed by the spacer thickness to be antiferromagnetic or AP ($J_1 < 0$) . This allows for an initial state where the opposing dipole fields from both FM layers sum to zero.

2.4 Spin polarization

Spin polarization relates the difference between the number of spin-up and spin-down electrons participating in a certain electronic process. Spin polarization is defined at the Fermi level with a model by Julliere [55] as the average of the density of states occupation of spin-up and spin-down electrons,

$$P = \frac{N_{E_f}(\uparrow) - N_{E_f}(\downarrow)}{N_{E_f}(\uparrow) + N_{E_f}(\downarrow)}\,, \tag{2.5}$$

which is normalized to one. In this case, spin-up (↑) electrons means electrons with spin parallel to the magnetization, and spin-down (↓) electrons are those antiparallel to the magnetization. Thus a positive spin polarization means that there are more electrons at the Fermi level with spin parallel to the magnetization of the layer, and a negative spin polarization means the contrary.

In 3d transition metals like Co, Fe, and Ni, the spin-up and spin-down **d** subbands are shifted in energy, leading to more electrons in one of the spin directions, causing the **d** bands to be strongly polarized.

2.5 Magnetoresistance

The Magnetoresistance (MR) through a spin valve or other multilayer device is the output signal of a spintronic device. A large percentage change in MR is desirable for noise-insensitive output signal levels. For both giant magnetoresistance (GMR) and tunneling magnetoresistance (TMR), the change in MR occurs with the relative orientation of the magnetization in the adjacent FM layers. In recent years, GMR and TMR have achieved percentage changes in MR of 65% (GMR) [56] to 600% (TMR) [57] at room temperature. Although the same equations are used to describe their overall effect, the two MR mechanisms are somewhat different.

2.5.1 Giant magnetoresistance (GMR)

GMR has already been introduced in section 1.2.1 with regards to the spin valve, but the mechanism of this effect is now discussed. The expressions for GMR are repeated here for comparison with Figure 2.6 noting that the junction resistances of an FM/NM/FM multilayer, R_P and R_{AP}, vary with the orientation of the FM layers (P and AP respectively):

$$GMR = \frac{R_{AP} - R_P}{R_P} = \frac{R_{max} - R_{min}}{R_{min}}.$$

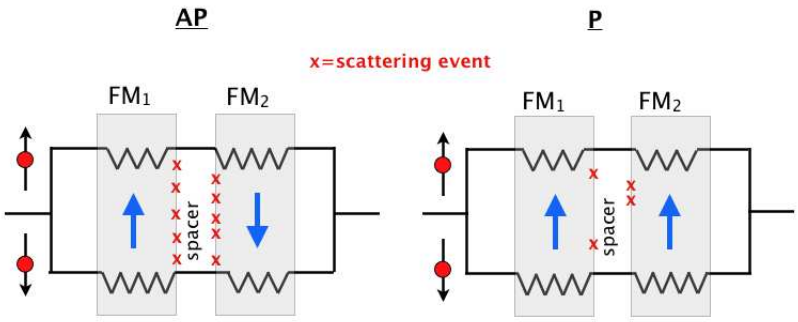

Figure 2.6: Resistive paths and their combination for P and AP FM layers. The blue arrows indicate the magnetization (and the majority carrier) of the FM layer. R_1 represents the resistance seen by a spin-up(down) electron at the boundary of a layer with majority spin-up(down) carriers, and R_2, the resistance seen by a spin-up(down) electron at the boundary of a layer with the opposite spin majority carrier.

GMR is fundamentally caused by the spin-dependent reflectivity or scattering of the spin carriers at the FM/NM interfaces [58] , which is the same scattering mechanism shown in Figure 2.5, causing the periodicity in the exchange coupling polarity (AP→P→AP) with spacer layer thickness. Figure 2.6 explains the AP and P layer cases diagramatically with paths for each spin carrier; R_1 represents the resistance seen by a spin-up (down) electron at the boundary of a layer with majority spin-up (down) carriers, and R_2 ($> R_1$), the resistance seen by a spin-up(down) electron at the boundary of a layer with the opposite spin majority carrier. In the AP case, both spin carriers are likely to be reflected/scattered as they diffuse to each interface resulting in an average of the two resistances, $\frac{R_1+R_2}{2}$. With P layers, the interfacial scattering occurs mostly for the carrier with spin opposite to the majority spin of the layers so that the majority spin carrier (spin-up in the figure) has a much lower resistance path through all the layers than the minority spin carrier (spin-down). The resistances of each path are combined as resistances in parallel , $2R_1 || 2R_2$. The AP case has a higher resistance over the P case. It was stated in section 1.2.1

that the GMR effect follows a $\cos(\theta_M - \theta_{Pinned})$ law. We use

$$R = R_{min} + \frac{1}{2}\left(R_{max} - R_{min}\right)\left(1 - \cos\left(\theta_{\mathrm{M1}} - \theta_{\mathrm{M2}}\right)\right) . \tag{2.6}$$

The premultiplier term constrains the MR response between R_{min} and R_{max}, and θ_{M1} is the in-plane magnetization angle of the free layer with respect to $\theta_{\mathrm{M2}} = \theta_{Pinned}$.

2.5.2 Tunneling magnetoresistance (TMR)

Tunneling magnetoresistance is the magnetoresistance across a magnetic tunnel junction. As stated at the end of section 1.2.1 these structures consist of two ferromagnetic electrodes (FM) sandwiching a thin insulating barrier (I). When a DC bias voltage is applied, electrons near the FM/I interface tunnel through the barrier and, since they are spin-polarized, the resistance depends on the relative orientation of the electrodes' magnetization, just as it does for GMR. The TMR ratio is defined in the same way as

$$TMR(\%) = \frac{R_{AP} - R_P}{R_P}$$

however, the change of the tunneling current in MTJs is more dramatic (~10x greater than GMR). TMR can be understood in terms of Julliere's model introduced in section 2.4, which is based on two assumptions. First, it is assumed that the spin of electrons is conserved in the tunneling process, so that the tunneling of spin-up and spin-down electrons are independent of one another. This assumption allows us to separate the conduction of electrons into two separate spin channels.

It is also assumed that the conductance for a particular spin orientation is proportional to the product of the effective density of states (DOS) of the two ferromagnetic electrodes. With

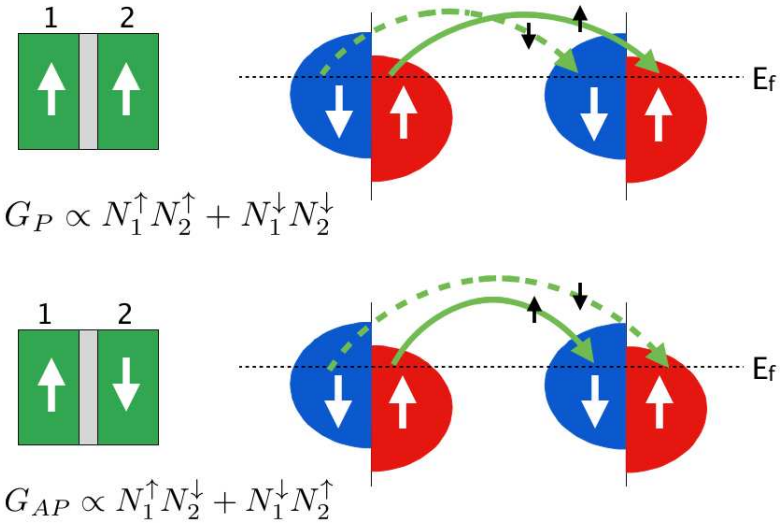

Figure 2.7: Tunneling of electrons between electronic states (shown as DOS diagrams) in FM films 1 and 2. Spin-up (solid green arrow) and spin-down (dashed green arrow) conduction channels are shown being independent. With P magnetization majority spins tunnel to majority spin states and minority spins to minority spin states. For AP magnetization of the films, majority spins in film 1 become minority carriers in film 2 and tunnel to minority spin states in film 2. Minority spins in film 1 tunnel to majority spin states in film 2.

these two assumptions, the TMR ratio, in terms of conductance is

$$TMR(\%) = \frac{G_{AP} - G_P}{G_P} = \frac{2P_1P_2}{1 - P_1P_2}$$

and rewriting equation 2.5 for the spin-up and spin-down channels

$$P_1 = \frac{N_1(\uparrow) - N_1(\downarrow)}{N_1(\uparrow) + N_1(\downarrow)} \qquad P_2 = \frac{N_2(\uparrow) - N_2(\downarrow)}{N_2(\uparrow) + N_2(\downarrow)}.$$

In the DOS drawing of Figure 2.7 the white arrows indicate the spin direction and the green arrows represent the spin channels. Electrons originating from one spin state in the first ferromagnetic film are accepted by unfilled states of the same spin in the second film. If the two ferromagnetic films are magnetized parallel, the minority spins tunnel to the minority states and the majority spins tunnel to the majority state. When the two films are magnetized antiparallel,

a majority spin in film 1 (polarization P_1) becomes a minority spin in film 2 (polarization P_2), so the majority spins of the first film tunnel to the minority states in the second film and vice versa. The larger change in magnetoresistance for TMR has been shown to be material-dependent such that one conduction channel gives a much greater probability of tunneling to electrons of one spin than those with the opposite spin [59, 60].

2.5.2.1 TMR bias voltage dependence

The magnetoresistance of an MTJ is a function of the bias voltage across the junction contacts. The TMR of MTJ devices decreases with increasing junction bias [61, 62]. This is a consequence of the decrease in tunneling probability across the insulator when the barrier height is increased with the junction bias. This characteristic is modeled by the empirical relationship [63, 26]

$$TMR(v) = \frac{TMR_0}{1 + \left(\frac{V_b}{V_h}\right)^2}\,. \tag{2.7}$$

V_b is the bias voltage and V_h is a fit parameter corresponding to the voltage bias at which the resistance of the MTJ is half the TMR at zero voltage bias $\left(\frac{TMR_0}{2}\right)$. The MR at zero-voltage bias is TMR_0 and is defined as

$$TMR_0(\%) \equiv \frac{(R_{max} - R_{min})}{R_{min}}\,, \tag{2.8}$$

where R_{min} and R_{max} are the low and high state values of the magnetoresistance respectively. This TMR voltage-dependence is modeled similarly in [25, 13].

2.6 Dynamics

Magnetization dynamics is concerned with the time-dependent motion or precession of a sample's magnetic moment due to a torque from an applied magnetic field. The torque from the applied

field is equivalent to the transfer of angular momentum to the magnetic moment causing it to precess about the applied field. However, the moments, over time, also align themselves in the direction of the field. This second process, called relaxation or damping, occurs because the moments lose energy to interactions with the material lattice (phonons), intinerant electrons, and magnons (spin waves). Without damping, the magnetic moment would simply precess about the applied field with $\frac{d\mathbf{m}}{dt}$ perpendicular to both the moment $\mathbf{m}$ and the field $\mathbf{H}$; the dissipative process of damping results in an effective torque perpendicular to $\frac{d\mathbf{m}}{dt}$ and $\mathbf{m}$ which causes the magnetization to relax into the field direction.

2.6.1 Precession and precession frequency

The precession of a magnetic moment occurs when the moment is subjected to a magnetic field which creates a torque on the moment: $\mathbf{T} = -\mathbf{m} \times \mu_0\mathbf{H}$. The torque acts to change the total angular momentum $\mathbf{L}$ by an amount $d\mathbf{L}$ in time dt, so that $d\mathbf{L} = \mathbf{T}dt$, hence the change in the angular momentum is directed in the direction of the torque. In Figure 2.8, The torque $\mathbf{T}$, is the cross product of the moment with the applied field, and so is perpendicular to both. The angle of magnetization or the angular difference between the applied field and the magnetization is θ. Because the torque is perpendicular to moment, the angular momentum $\mathbf{L}$ does not change in magnitude, but only in direction. As long as the field is present, $\mathbf{L}$ will continue to change as shown at the bottom of the figure, causing the magnetic moment to move or precess in the direction of the torque. Because $\mathbf{m}$ and $\mathbf{L}$ are directly related by the gyromagnetic ratio (section 2.1), the change in the direction of the magnetic moment is also directly related to the torque by γ as

$$\frac{d\mathbf{m}}{dt} = \gamma\mathbf{T} = \gamma(\mathbf{m} \times \mathbf{B}), \tag{2.9}$$

where $\mathbf{B} = \mu_0\mathbf{H}$. The frequency of the precession is also related to γ $\left(\frac{rad}{\mathrm{s}\cdot\mathrm{T}}\right)$. This is shown in Figure 2.9. The component of $\mathbf{L}$ perpendicular to the torque vector gives the change in the angular momentum in the direction of the torque. The rate at which both $\mathbf{L}$ and $\mathbf{m}$ precess ($\frac{d\varphi}{dt}$

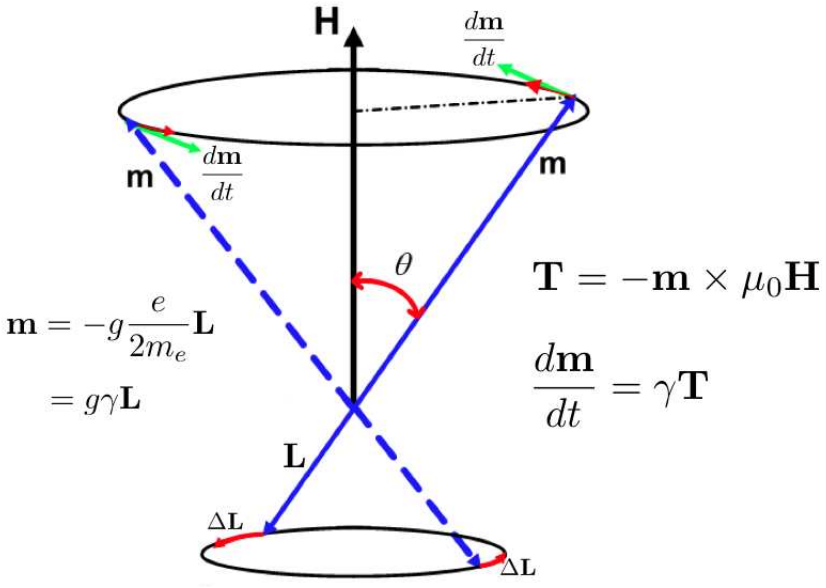

Figure 2.8: Magnetic precession.

in Figure 2.9) is called the Larmor frequency, ω_L. Since the torque arises from the moment's interaction with the applied field,

the precession frequency is also directly proportional to the applied field via γ as

$$\omega_L = \gamma \mathbf{B}\,,$$

as shown in Figure 2.9. The precession of the magnetic moment from equation 2.9 can be rewritten

$$\frac{d\mathbf{M}}{dt} = -\gamma_0 \left(\mathbf{M} \times \mathbf{H}\right)\,, \tag{2.10}$$

where the magnetization is $\mathbf{M} = \frac{\mathbf{m}}{V}$, $\gamma_0 = \mu_0 \gamma$ $\left(\frac{\mathrm{m}}{\mathrm{A \cdot s}}\right)$, and V is the volume of the material.

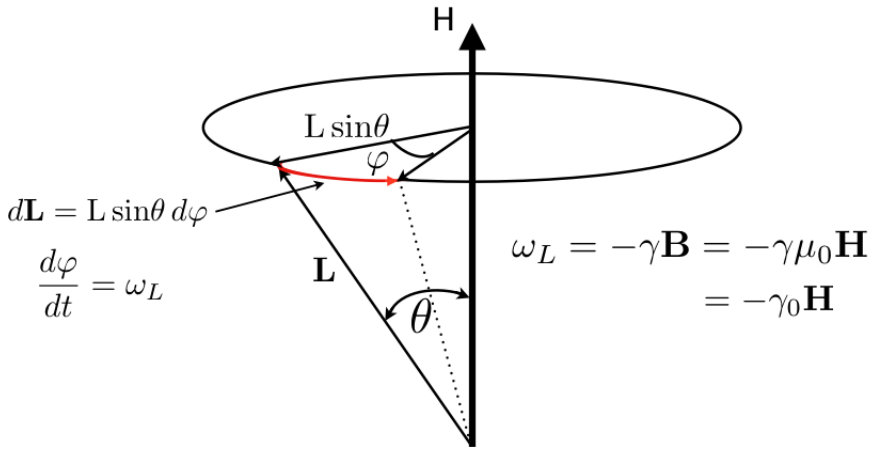

Figure 2.9: Precession frequency

2.6.2 Spin relaxation or damping

The relaxation of a free layer's magnetization to the equilibrium state $\mathbf{M} \times \mathbf{H} = 0$ (zero torque) when an applied field, $\mathbf{H}$, is present is called damping. Damping has been observed as a non-linear process which determines the rate of the spin relaxation, and has generally been considered phenomenological in nature. Recently, the intrinsic damping has been derived from first principles and is shown to originate in spin-orbital coupling [64]. The strength of the damping is called the Gilbert damping parameter, α, after Gilbert who accounted for the relaxation by subtracting a viscous-type term proportional to the time derivative of the magnetization [65], which looks like

$$\frac{d\mathbf{M}}{dt} = \frac{\alpha}{M_s}\left(\mathbf{M} \times \frac{d\mathbf{M}}{dt}\right) . \tag{2.11}$$

The damping parameter is material dependent. A larger value of α causes a stronger damping effect or faster spin relaxation. The damping term, as can be seen from equation 2.11, is necessarily perpendicular to both the magnetization and the precession direction as shown in Figure 2.10. The magnitude of the magnetization must remain constant at its saturation magnetization, but its direction, given by the angle θ, gradually decreases to 0° via the damping torque. Without

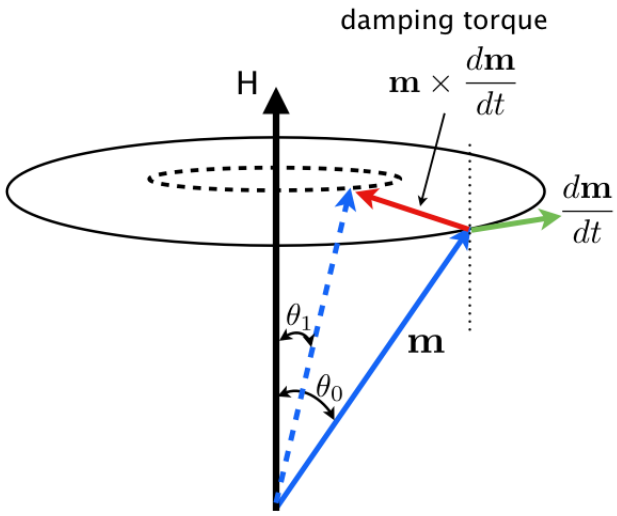

Figure 2.10: The action of damping described by the Gilbert damping torque.

damping, the magnetization would simply precess at a constant angle, θ, to the applied field.

2.6.3 Spin transfer torque (STT)

In 1989, Slonczewski used a ferromagnetic multilayer with a tunnel barrier and observed that even at zero junction bias, a spin current flowed across the tunnel junction whenever the magnetizations of two FM electrodes were not collinear [66]. Both Berger [67] and Slonczewski [68] independently predicted that a current flowing perpendicular to the plane in a metallic multilayer could potentially generate a spin transfer torque strong enough to switch the magnetization in one of the layers.

The spin current is a flow of non-equilibrium conduction electrons from which the free layer electrode absorbs some of the spin angular momentum (torque transfer). In the multilayer there is always one FM electrode which is pinned or has a higher coercivity and is the source of spin-polarized electrons as described by equation 2.5. The electron flow forming the spin current can originate from the FM layer on either side of the spacer region depending on the junction's

voltage bias. A simplified STT system is shown in Figure 2.11 with the FM layers beginning in an AP state. The electrical current flows from V^+ to V^- and the spin-polarized electron current (spin current) from the source layer on the left, traverses the NM spacer to the interface with the free/receiving layer. The source layer has a magnetic moment, $\mathbf{m_p}$ $\left(\mathrm{Am}^2\right)$, polarized in the direction $\hat{\mathbf{e}}_\mathbf{p}$, and those spin-polarized electrons build up at the interface to the free layer. The free layer exerts a torque on $\mathbf{m_p}$ ($\propto \mathbf{m}\times(\mathbf{m}\times\hat{\mathbf{e}}_\mathbf{p})$) and $\mathbf{m_p}$ responds with an equal and opposite torque on $\mathbf{m}$ (both torques shown in red arrows), changing the moment of the free layer, so that it becomes parallel with that of the source layer when a switching current threshold is reached. This balance of torque occurs to conserve the total angular momentum of the system.

When the magnetization of the free layer is parallel with the polarizing/pinned layer, the same torque transfer mechanism occurs but the minority electrons of the free layer (those with spin opposite to $\mathbf{m_p}$ and $\mathbf{m}$) are actually the electrons making up the spin-polarized current. These minority spin electrons become trapped in the interface layer and are reflected at the interfaces with the FM electrodes as depicted in Figure 2.12. With each reflection event, the minority spin electrons transfer a torque equal and opposite to the torque due to the moment in the FM layer. This will not affect the pinned layer, which has an abundant population of $\hat{\mathbf{e}}_\mathbf{p}$-polarized electrons, but the number of electrons transferring torque back to the free layer will eventually reach a threshold which will switch the free layer AP to $\mathbf{S_1}$. The process of switching the free layer from a P state to an AP state with the pinned layer requires a larger electrical current ($-I_s$ in the figure), and more time (larger $-I_s$ pulsewidth) to complete the free layer reversal, than in the AP to P process.

The magnitude of the torque transferred is proportional to the transverse component of angular momentum of the spin-current electrons (which is the change in angular momentum),

$$\Delta\mathbf{L} = \frac{\hbar}{2}\,\mathbf{m}\times(\mathbf{m}\times\hat{\mathbf{e}}_\mathbf{p})\ (\mathrm{J}\cdot\mathrm{s}) \tag{2.12}$$

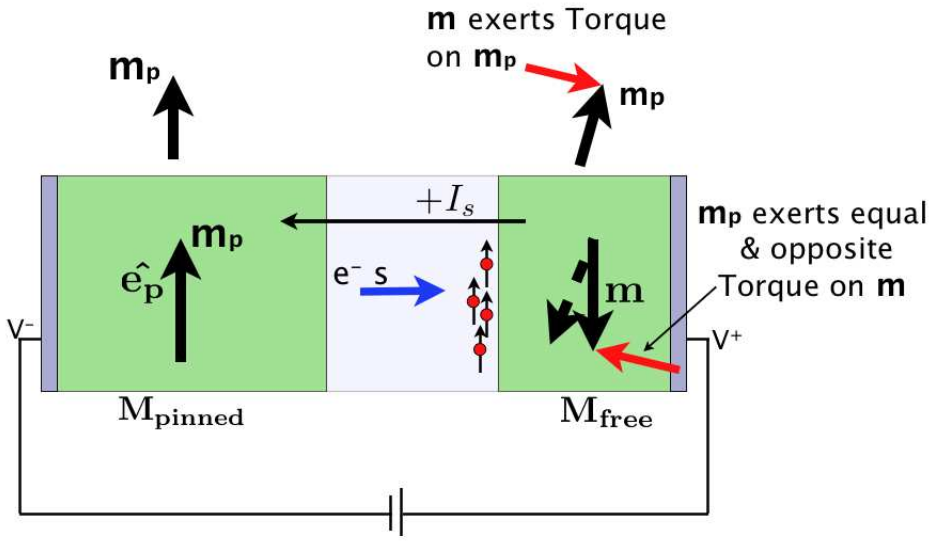

Figure 2.11: A spin valve using spin transfer torque to switch the free layer magnetization from AP to P with the polarizing/pinned layer. Electrons with magnetization $\mathbf{m_p}$ are transported across the spacer layer due to the junction current I_s, and transfer their angular momentum to the free layer electrons at the spacer/free layer interface. The free layer will reverse its magnetization to be P with the polarizing/pinned layer with a sufficient I_s magnitude and pulse width.

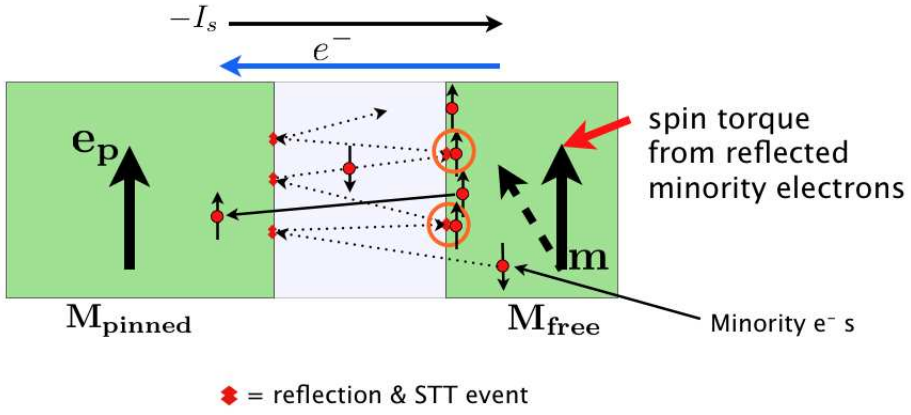

Figure 2.12: The process of reversing the free layer moment from a P state. The majority electrons in the free layer (spin-up, ↑) find states in the pinned layer and are transmitted across the spacer with the electron flow (solid arrow). The minority electrons of the free layer are confined in the spacer and upon reflection at the spacer/FM interfaces, transfer spin torque back to the both layers (dotted lines). When the magnitude and pulse width of I_s is great enough, the free layer's minority electrons will transfer enough angular momentum to switch the free layer AP to the polarizing layer.

multiplied by the rate of transfer of the spin-current electrons,

$$\frac{1}{\Delta t} = \frac{\mathrm{I_s} G(\theta)}{e} \left(\frac{1}{s}\right) . \tag{2.13}$$

The transfer rate includes a conduction-efficiency factor $G(\theta)$, which is dependent on the material polarization, P, of equation 2.5 and the parallel ($\theta = 0$) or antiparallel ($\theta = \pi$) state of magnetization between the free and pinned layer. For a polarization of P = 0.35, $G(0) \backsimeq 0.127$ and $G(\pi) \backsimeq 0.515$. The torque is then

$$\mathbf{T_{stt}} = \frac{\mathrm{I_s} G(\theta) \hbar}{2e} \, \mathbf{m} \times (\mathbf{m} \times \hat{\mathbf{e}}_\mathbf{p}) . \tag{2.14}$$

The effect that STT has on the magnetization of the free layer is shown Figure 2.13. In contrast to the damping torque, the STT compels the magnetization angle to become larger, moving the moment direction away from the applied field if a field is present. By balancing the damping and STT torques with a field applied in the initial direction of the free layer magnetization, the free layer magnetization can undergo the dynamical state of steady state precession, given the appropriate junction bias (spin current).

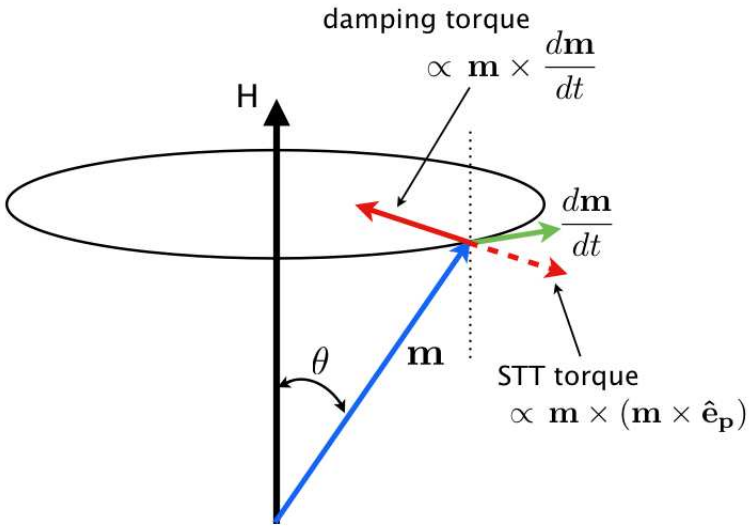

Figure 2.13: The effect of STT on magnetization trajectory. STT torque opposes damping torque and can increase the cone angle, θ, past 90° which will reverse the magnetization. Alternatively, the STT torque can balance with the damping torque causing the magnetic moment to undergo steady-state precession.

Chapter 3 – Materials and device considerations

This chapter discusses some general information about common materials used for the devices introduced in Chapter 1. The limited set of layer materials presented are those that are prominent in the research papers read concerning spintronic multilayer devices. Device materials are chosen to enhance various operating characteristics of a device, such as higher Néel and Curie temperatures for higher temperature operation, or a pairing of a FM and Insulator material that gives a larger TMR result.

3.1 General device/material geometries

The devices introduced in chapter 1 use material layers matched in long and short axial dimensions as shown in Figure 3.1. The thickness will depend upon the particular layer. For example, to facilitate exchange coupling, the spacer interlayer must have a thickness which is less than the mean free path of the FM layers' electrons. The ferromagnetic layers FM-free and FM-pinned typically have the same thickness, but thickness asymmetry can be used to change the character of the free layer's hysteresis curve [35] . The required thickness of the AFM pinning layer, t_{AFM}, must be greater than the finite distance needed for a gradual 180° reorientation of moments. This AFM-FM interface distance is called an exchange length or domain wall. It is necessary to keep the AFM moments fixed in the presence of an applied field as the FM moments twist in the applied field direction. The exchange length is dependent on the AFM anisotropy constant, K_{AFM} $\left[\frac{\mathrm{J}}{\mathrm{m}^3}\right]$, and the required AFM thickness is described by $t_{AFM} > \frac{J}{K_{AFM}}$, where J $\left[\frac{\mathrm{J}}{\mathrm{m}^2}\right]$ is the exchange strength between the AFM/FM layers .

An MTJ would be similarly constructed with a tunnel barrier material, 0.5 nm - 3 nm thick.

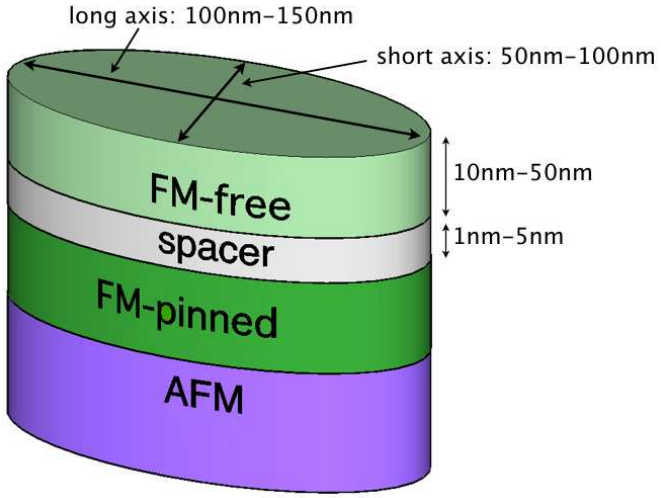

Figure 3.1: Spin valve with typical layer geometry

AFM layer	$T_N(^\circ C)$
IrMn	417
FeMn	217
NiMn	797
PtMn	207
NiO	252

Table 3.1: Antiferromagnetic layer materials

3.2 Antiferromagnetic materials

The AFM pinning of the fixed FM layer in a spin valve or other multilayer magnetic device gives the pinned layer magnetic stability which is important to the reliability and sensitivity of the device. The materials listed in Table 3.1 are commonly-used AFM materials for pinning in magnetoresistive multilayer devices. The Néel temperature, T_N, for the antiferromagnets, is also listed.

Most of these alloys have Néel temperatures that are less than half that of the Curie temperatures of the common FM materials making it simpler to achieve the exchange biasing process described in section 2.3.1. In the case of NiMn, which might be used in a high temperature application, an FM material with a substantially higher T_C, such as the Co alloys of Table 3.2

would be required for the pinning process and the overall ambient device operation.

3.3 Ferromagnetic materials

The ferromagnetic materials used in spintronic devices are soft magnetic materials meaning that they can be easily magnetized - this property is called permeability (μ). The soft FM materials like those in Table 3.2 come from the transition metal series and have a high average magnetic moment per atom, expressed in the table as n_B, the number of Bohr magnetons (μ_B). The atomic moments of the ferromagnetic elements and their alloys are plotted against their atomic number on the Slater-Pauling curve [69, 70]. This curve shows that body-centered-cubic (BCC) CoFe and NiFe have the highest average moment count for alloys at almost $2.5\mu_B$ with face-centered-cubic (FCC) CoFe and NiFe coming in a little lower at about 1.5-1.8μ_B. In these specific materials, the number of Bohr magnetons/atom translates to a high value of saturation magnetization, M_S. M_S is the magnitude of the magnetization of the FM layer and is an indication of the torque that a magnetic field will exert on it, and therefore the ability to manipulate that layer's magnetization.

In addition to the high saturation magnetization of NiFe alloys, NiFe thin films can be stoichiometrically composed and annealed to have virtually no crystallographic or magnetostriction anisotropy (the deformation of the film in the direction of an applied field). This creates a high permeability, μ, where

$$\mu \propto \frac{M_S^2}{K_{\text{eff}}} \tag{3.1}$$

when the effective anisotropy, K_{eff}, is low, which means that the material is very responsive to small applied fields. NiFe alloys have relatively low resistivities in the range of $30 \leq \rho \leq 50$ $\mu\Omega \cdot cm$ and can be used in the 10 MHz frequency range. The CoFe alloys have an even higher M_S but experience significant magnetostriction and resitivity of about 10 $\mu\Omega \cdot cm$ [48]. To eliminate magnetostriction and/or allow for higher frequency operation, an amorphous alloy may be used.

Amorphous ferromagnetic alloys are formed using a nonmetallic element with some metallic

FM layer	$T_C(^\circ C)$	n_B (μ_B)	M_S ($^A/_m$)
NiFe	803	~2.3	8×10^5 (FCC)
CoFe	1200	~2.4	2×10^6 (BCC)
Co	1388	1.7	1.44×10^6 (HCP)
CoFeB	>1300		1.6×10^6 (Amor.)
Fe	1043	2.2	1.7×10^6 (BCC)

Table 3.2: Soft ferromagnetic layer materials

Spacers	Tunnel barriers
Cu	Al_2O_3
Ru	MgO

Table 3.3: Spacer and tunnel barrier materials

properties, like Boron (B), and combining it with a ferromagnetic alloy, like CoFe. Their properties are low coercivity, low hysteresis loss and high permeability. These materials also have higher electrical resistivity. They have Curie temperatures comparable to most ferromagnetic crystalline alloys. For CoFeB it can be seen in Table 3.2 that the M_S is not much decreased from polycrystalline CoFe, but the reduction in the effective anisotropy will increase the alloy's permeability, and the T_c is in fact increased over CoFe. In addition, the resistivity of CoFeB is much higher, up to 130-150 $\mu\Omega \cdot cm$ in thin films compared to ~ 10 $\mu\Omega \cdot cm$ in CoFe. The higher resistivity allows for higher frequency operation by decreasing eddy currents in the film [71, 72].

3.4 Interlayer materials

The two non-magnetic (NM) spacer materials given in Table 3.3 , Copper and Ruthenium, are frequently encountered in the literature as interlayer materials in multilayer devices. Metallic spacer materials allow spin communication between the FM layers through exchange coupling, but because this coupling is weak, the FM layers are also allowed to be independently switched. The magnitude of the GMR effect is also an important factor in choosing a FM/NM pair. Additionally, the spacer metals should have relatively good lattice matching (0-10%) with the FM metals to prevent lattice discontinuites which disrupt electron transport. For GMR, the spacer layer

thickness must be less than the mean free path of electrons in the metal spacer to allow the carrier's spin to traverse the spacer thickness without spin-flip.

The two metal oxide dielectrics, Aluminium oxide (Al_2O_3) and Magnesium oxide (MgO), are by far the most commonly-used materials for magnetic tunnel junctions (MTJ), Al_2O_3 partly due to historical reasons. The popular choice of these materials as tunnel barriers stems from the high TMR ratios achieved when they are used with several of the FM layer materials in Table 3.2. The mechanism of polarized spin conduction between the insulator and FM electrodes discussed in section 2.5.2, MgO tunnel barriers have achieved up to 600% TMR [57], while MTJs using Al_2O_3 now have TMR values ranging from 60% - 70% [73].

3.5 Summary

The literature regarding the characteristics of multilayer materials for spin valves and other magnetic devices indicates that there are many properties and interactions yet to research and understand. This is a relatively new field (GMR was discovered in 1988), and at this time there are no completely clear recipes which define successful material choices and combinations, although many important guidelines have been established. Much of the ongoing research is to understand the underlying mechanisms of material combinations that work well. Material properties have not been a focus in modeling the magneto- static and dynamic components of spin valves and MRAM devices, but basic material properties and interactions have been reviewed. In this work all modeling has been done using parameters for $Ni_{80}Fe_{20}$ (Permalloy) for the FM layers and copper as the non-magnetic spacer layer (using an appropriate exchange constant, J_1). In the Toggle MRAM, the TMR block assumes an MgO tunnel barrier with a bias effect parameter based on measurements of Fe/MgO/Fe MTJs [31]. A strong exchange bias for the AFM-FM_{pinned} layers is assumed, such that the direction of the FM pinned layer is fixed.

Chapter 4 – Effective fields and torques

In this chapter certain material and physical anisotropies and their effective fields will be explained and expressions will be developed for the torque acting upon the free layer due to these fields. The field and torque expressions are divided into 2-D and 3-D sections. Both sections are intended for three dimensional devices, but the torques and fields acting on the magnetization vector are either derived as 2-D or 3-D expressions. Precession in magnetization occurs as the thin-film magnet's angular momentum, $\mathbf{L}$, changes, making torque, $\mathbf{T} = \frac{d\mathbf{L}}{dt}$, an appropriate term with which to work in the conservation of angular momentum. It is often easier to work with an energy expression for a particular interaction and deduce the torque from the derivative of the energy term with respect to the angle of magnetization. In a defined system Brown's theorem, $\mathbf{M} \times \mathbf{H_{eff}} = 0$, expresses that the torque exerted on a magnetization by an effective field must be zero at equilibrium [74]. The device models use this concept by equating the balance of individual torque terms at equilibrium and thus determine a stable equilibrium solution for the magnetization.

4.1 Effective fields

Every torque term acting on a magnetic moment or magnetization vector is the result of an effective field term. The field terms that have been modeled sum to a total effective field

$$\mathbf{H_{eff}} = \mathbf{H_a} + \mathbf{H_k} + \mathbf{H_d} + \mathbf{H_{ex}} + \mathbf{H_{stt}}, \tag{4.1}$$

where the fields are defined as follows (V is the volume of an FM layer and μ_0 is the permeability of free space):

$\mathbf{H_a}$ An external, applied field.

$\mathbf{H_k}$ The anisotropy field for a set of intrinsic, material anisotropy effects.

$\mathbf{H_d}$ The demagnetization field, an internal field which develops due to the shape of the ferromagnet.

$\mathbf{H_{ex}}$ The effective field from the transfer of spin information through a spacer layer via the interlayer exchange coupling.

$\mathbf{H_{stt}}$ The effective field from the transfer of spin torque via a current-perpendicular-to-the-(thin-film)-plane (CPP) .

4.1.1 Relationship of torque to effective field

A magnetic material can have its magnetization orientation described by an energy function in θ which might include a variety of conditions such as any of the effective fields above. As torque acts upon the magnetic moment of the thin-film layer, the energy function will vary as a function of θ. A torque term may be computed as

$$\mathbf{T} = \frac{\partial E}{\partial \mathbf{M}} \frac{\partial \mathbf{M}}{\partial \theta} = \frac{\partial E}{\partial \theta} \tag{4.2}$$

where θ is the angle of magnetization with respect to the easy axis of the FM layer. This is identical to taking the cross product of the magnetic moment with the effective field term,

$$\mathbf{T} = -\mu_0 \mathbf{m} \times \mathbf{H} \,. \tag{4.3}$$

The torque can also be indirectly accessed by using equations **??** and **??** to result in an expression for $\mathbf{H_{eff}}$ [75],

$$\mathbf{H_{eff}} = -\frac{1}{\mu_0 V M_S} \frac{\partial E}{\partial \theta} \tag{4.4}$$

(and the torque as $\mathbf{T} = -\mu_0 V M_S \mathbf{H_{eff}}$) . These relationships for determining the expressions for torque or field are used throughout this chapter. When either the system energy is minimized,

$\frac{\partial E_{sys}}{\partial \theta} = 0$, or the system torques are balanced, the system equations yield a stable equilibrium value for the magnetization in terms of θ.

4.2 Energy and torque for two-dimensional models

A 2-D dynamic model is appropriate for systems where timing the process of magnetic reversal or switching does not need to be precise - only the end state of the magnetization need be correct relative to its previous state. The path of the magnetization is approximated to remain in the plane of the FM thin film with an increased damping effect which can result in faster switching results over those of a 3-D model. The 2-D model is simpler than the 3-D version, and can act as a fast-runtime compact model for observing magnetization behavior of a device or system of devices. Transitioning to 3-D field terms is also made more tractable by beginning with the 2-D components.

The overall 2-D model for a spin valve considered only uniaxial crystalline anisotropy, an applied field, and the dynamic damped precessional torque. The interlayer exchange coupling along with a dipole coupling field between FM layers were subsequently added for the Toggle MRAM model.

4.2.1 Applied field

The applied field in the 2-D case is confined to be in the plane of the thin-film with components in the $\hat{\mathbf{x}}$ and $\hat{\mathbf{y}}$ directions. The energy from the applied field is often called the "Zeeman" energy after the Dutch physicist Pieter Zeeman, who observed that there was an interaction between the magnetic moment of an atom or molecule and an applied magnetic field. The energy is simply $E_a = \mathbf{m} \cdot \mu_0 \mathbf{H_a}$ where the magnetic moment is the magnetization over the layer volume, $\mathbf{m} = \mathbf{M}V$, and $\mathbf{H_a}$ is the vector sum of the applied field components in the $\hat{\mathbf{x}}$ and $\hat{\mathbf{y}}$ directions.

E_a and its torque, $\frac{\partial E_a}{\partial \theta}$ are written as:

$$E_a = -\mu_0 \mathrm{V} M_S \left(\mathrm{H}_x cos\theta_M + \mathrm{H}_y sin\theta_M\right) \tag{4.5}$$

$$\mathbf{T_a} = \mu_0 \mathrm{V} M_S \left(\mathrm{H}_y cos\theta_M - \mathrm{H_x} sin\theta_M\right) . \tag{4.6}$$

4.2.2 Shape anisotropy

The shape anisotropy field was introduced in section 2.2.2 as $\mathbf{H_d} = -N\mathbf{M}$. Using this field to expand equation 2.3 gives

$$\begin{aligned} E_d &= \frac{1}{2}\mu_0 V \mathbf{M}\left(N_x + N_y\right)\mathbf{M} \\ &= \frac{1}{2}\mu_0 V M_S^2\left(N_x \cos^2\theta + N_y \sin^2\theta\right) \\ &= \frac{1}{2}\mu_0 V M_S^2\left[N_x + \left(N_y - N_x\right)\sin^2\theta\right] \end{aligned}$$

if $N_x \cos^2\theta$ is replaced with $N_x\left(1 - \sin^2\theta\right)$. Since θ is measured with respect to the long/easy axis (x-axis, $\theta = 0°$), the energy expression for the shape anisotropy shows that E_d will be a maximum in the $\hat{\mathbf{y}}$ direction ($\theta = 90°$), on the short axis, and a minimum in the $\hat{\mathbf{x}}$ direction on the long axis ($\theta = 0°$). The torque is

$$\mathbf{T_d} = \frac{1}{2}\mu_0 V M_S^2 (N_y - N_x)\sin 2\theta = K_{sh} V sin2\theta_M \,, \tag{4.7}$$

with the shape anisotropy constant defined as $K_{sh} = \frac{1}{2}\mu_0 M_S^2\left(N_y - N_x\right)$. The energy and torque for the shape anisotropy are very similar to these same expressions for crystalline anisotropy, and may be combined.

K_{sh} has not been included in the 2-D models but has been transformed with spherical coordinates (section 4.6.3) and used in 3-D spin valve and STT simulations .

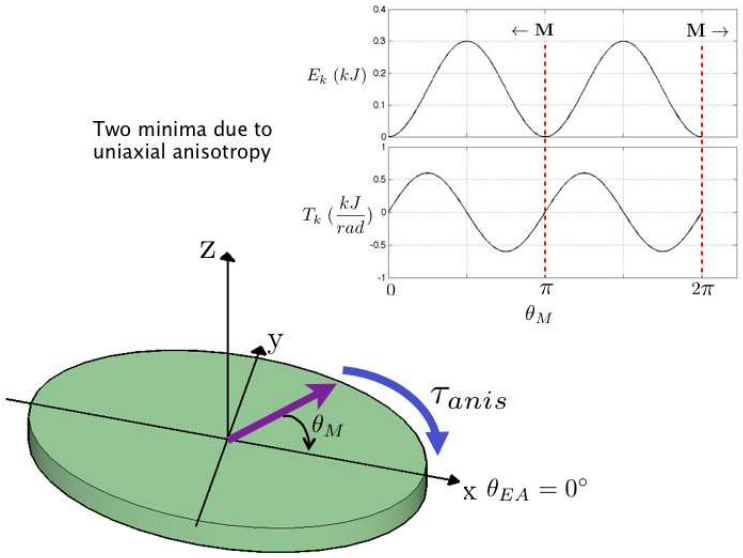

Figure 4.1: Uniaxial crystalline anisotropy torque present in a thin-film ferromagnetic layer. The uniaxial anisotropy causes two energy minima (upper graph) on the long or easy axis at 0° and 180°, while the torque (lower graph) is zero at the energy minima.

4.2.3 Uniaxial crystalline anisotropy

An energy function for the uniaxial crystalline anisotropy was given in section 2.2.1 as

$$E_k = V(K_{u1}sin^2\theta + K_{u2}sin^4\theta + \ldots)\,. \tag{4.8}$$

In the models, we use only one anisotropy constant, $K_{u1} = K_u = 300\,^J/_{m^3}$ for simplicity. The torque is

$$\mathbf{T_k} = \frac{dE_k}{d\theta} = 2VK_usin\theta_M cos\theta_M = K_u \mathrm{V} sin2\theta_M\,. \tag{4.9}$$

The mathematical form of the shape anisotropy torque, $\mathbf{T_d}$, is identical to $\mathbf{T_k}$ with the constant K_{sh} replacing K_u. Depending on the component values used for the tensor N, $25 \leq \frac{K_{sh}}{K_u} \leq 50$, revealing that $\mathbf{T_k}$ is small compared to $\mathbf{T_d}$. Shape anisotropy defines the easy axis as the long axis of the FM layer, along which it costs less energy to magnetize the sample as there exists a smaller opposing field in the long direction. It is not unusual to combine the uniaxial and shape

anisotropy constants as $K = K_u + K_{sh}$ and use K in place of K_u in equation 4.9 to add the effect of shape to the model. The torque's effect on the magnetization of the FM layer and how the system energy varies with θ is shown in Figure 4.1. θ_M is the angle of magnetization measured relative to the easy axis, which in the figure is on the x-axis for $\theta_{EA} \equiv 0°$. The crystalline anisotropy torque works to pull $\mathbf{M}$ back to the easy axis whenever θ_M is not collinear with θ_{EA}. The energy diagram shows that the crystalline anisotropy results in two stable energy minima along the x-axis at 0/360° and 180°, and the torque $\mathbf{T_k}$ (lower graph), is zero at the energy minima. The unstable energy maxima (also where $\mathbf{T_k} = 0$) are along the shorter, hard axis (y-axis) at 90° from θ_{EA}.

4.2.4 Effect of combined applied field and crystalline anisotropy

If the crystalline anisotropy energy from equation 4.8 is summed with the energy in equation 4.5, one can get a sense for how the particle will respond in an applied field. At the top of Figure 4.2 the zero applied field state is shown. There are two stable energy minima at 0° and 180°. The middle drawing shows that when a field with arbitrary direction is applied, $\mathbf{M}$ rotates away from it's initial position in the direction of the applied field due to the torque from the field, as depicted in the cartoon, and the energy minima shift to a single magnetization angle in the bottom drawing, when the field/torque is of a critical strength; the magnetization minimum ($\theta_1^{'}$ on the bottom graph) remains as long as the field is constant.

4.2.5 Interlayer exchange coupling (IEC)

The torque for the interlayer exchange coupling is developed using only the bilinear (J_1) term in equation 2.4 and multiplying by the area of the layers , A, for a result in joules. The IEC energy is

$$E_{exch} = -\mathrm{A}\, J_{ex}\, cos\theta_{\mathrm{M}}\,, \tag{4.10}$$

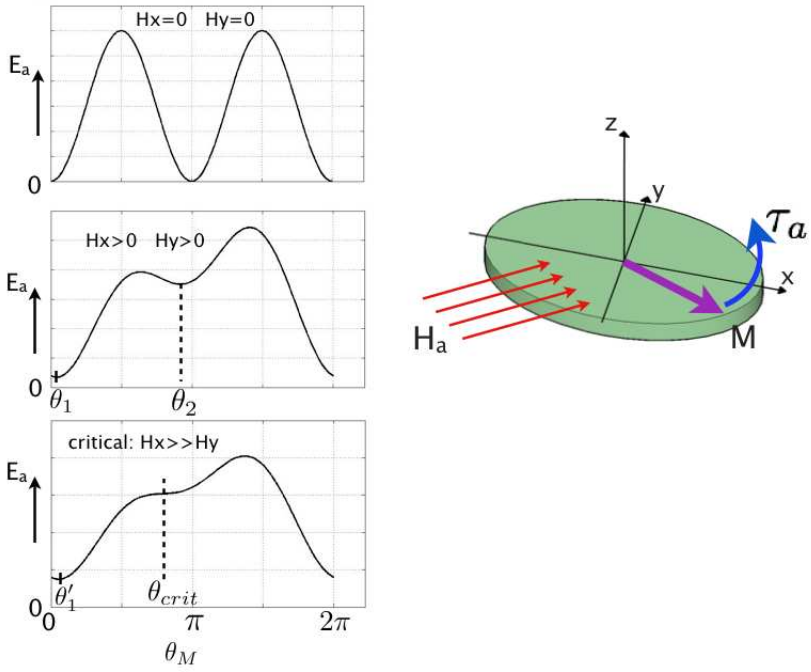

Figure 4.2: Effect of an applied field combined with uniaxial anisotropy. The plots of the single-domain particle energy vs. θ_{M} under the indicated applied field conditions show that in zero field, the uniaxial anisotropy controls the magnetization of the film. With non-zero fields stable magnetization angles are found at local minima (θ_1 and θ_2), but with a large critical field applied, only one global minimum or stable magnetization ($\theta_1^{'}$) exists.

and the torque,

$$\mathbf{T}_{\text{exch}} = \frac{dE_{exch}}{d\theta} = \text{A}\, J_{ex} \sin\theta_{\text{M}} \tag{4.11}$$

where J_{ex} is the same bilinear exchange constant in Table 2.1. Since the energy of exchange depends on the relative orientation of the layer magnetizations and the interlayer thickness, the interlayer exchange torque works to bring the FM layers into P alignment for some thicknesses, and into AP alignment for others, depending on which of these states the energy is minimized for. In this way, the spin information between the FM layers is communicated.

4.2.6 Dipole coupling

When two FM layers are in close proximity, the magnetic fields from one layer affect the other through magnetostatic dipole forces. This interaction favors the anti-parallel alignment of the layers. The magnetic moment of an FM layer determines the direction of the magnetic field emanating from that layer while internally, an opposing magnetic field is set up called the demagnetizing field. For very thin layers in close proximity, the magnetic fields are assumed to be approximately the same as the demagnetizing fields determined by the layer's demagnetizing factors, N_x and N_y. Given two FM layers (layer 1 and 2), the effective magnetostatic coupling field from layer 1 to layer 2, $\mathbf{H_{12}}$, is proportional to the demagnetizing field in layer 1 multiplied by a magnetostatic coupling attenuation factor, r, assuming the lateral dimension of the layers are much larger than their thicknesses [76]. The complementary situation is also true for layer 2 and its proportional field, $\mathbf{H_{21}}$. Deriving an expression for torque due to this magnetostatic coupling begins by describing the demagnetization fields of the two coupled layers. Regarding Figure 4.3, the required parameters are listed on each layer with $M_{S1,2}$ and $\mathbf{H_{d1,2}}$ as the saturation magnetization and demagnetizing fields for layers 1 and 2 respectively. Because the FM layer magnetization prefers a particular direction due to the layer's shape, the magnetostatic coupling field is proportional to the shape anisotropy (defined in section 2.2.2 as $-N\mathbf{M}$). The

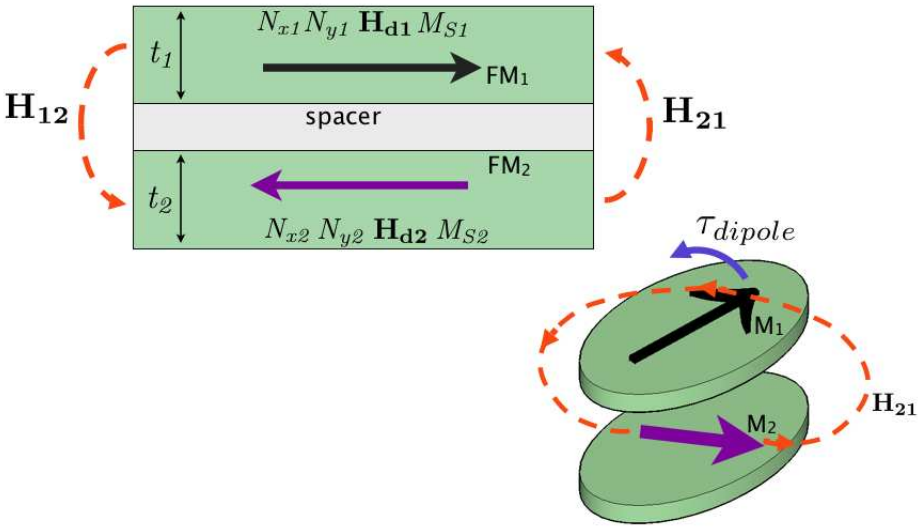

Figure 4.3: Ferromagnetic layers coupled by dipole fields $\mathbf{H_{12}}$ and $\mathbf{H_{21}}$ with parameters noted on each layer. The ellipsoidal layers illustrate the $\mathbf{H_{21}}$ field from layer 2 producing a torque on $\mathbf{M_1}$.

demagnetizing fields for layers 1 and 2 are calculated as

$$\mathbf{H_{d1}} = -\frac{\mathbf{1}}{\mathbf{2}}\,(N_{y1} + N_{x1})\mathbf{M_1}, \quad and \quad \mathbf{H_{d2}} = -\frac{\mathbf{1}}{\mathbf{2}}\,(N_{y2} + N_{x2})\mathbf{M_2}\,. \tag{4.12}$$

These are once again, internal, self-generated fields, requiring a factor of 1/2. The attenuation factor is in the range $0 \leq r \leq 1$, however Wang [77] estimates that $r = 0.8$ for zero separation between the FM layers for his rectangular shaped layers, implying a shape/aspect ratio dependence for r. Using equation 4.12 and expanding $\mathbf{M}$ into its components in $\hat{\mathbf{x}}$ and $\hat{\mathbf{y}}$ as $M_S cos\theta\hat{\mathbf{x}} + M_S sin\theta\hat{\mathbf{y}}$, the coupling fields are

$$\mathbf{H_{12}} = r \cdot \mathbf{H_{d1}} = \frac{rM_{S1}}{\mathbf{2}}\,(-N_{y1}\,sin\theta_{\mathrm{M1}} - N_{x1}\,cos\theta_{\mathrm{M1}}) \tag{4.13}$$

$$\mathbf{H_{21}} = r \cdot \mathbf{H_{d2}} = \frac{rM_{S2}}{\mathbf{2}}\,(-N_{y2}\,sin\theta_{\mathrm{M2}} - N_{x2}\,cos\theta_{\mathrm{M2}})\,. \tag{4.14}$$

Note that the demagnetizing factors are not vectors but can be applied only to the magnetization component along the same principle axis as the factor, which maintains the directional components of the vector. The torque on layer 2 due to the dipole field of layer 1 is

$$\boldsymbol{T_{12}} = -\mu_0 V_1 \left(\mathbf{M_2} \times \mathbf{H_{12}}\right) = -\mu_0 V_1 \frac{r M_{S1} M_{S2}}{2} \cdot \begin{bmatrix} cos\theta_{\mathrm{M2}} & sin\theta_{\mathrm{M2}} \\ -N_{y1} sin\theta_{\mathrm{M1}} & -N_{x1} cos\theta_{\mathrm{M1}} \end{bmatrix}$$

$$\boldsymbol{T_{12}} = J_{12} \cdot \left(N_{y1} sin\theta_{\mathrm{M1}} cos\theta_{\mathrm{M2}} - N_{x1} cos\theta_{\mathrm{M1}} sin\theta_{\mathrm{M2}}\right) . \tag{4.15}$$

$\mathrm{V}_1 = A_1 t_1$ and is the volume of layer 1. Similarly, the torque on layer 1 due to the dipole coupling field of layer 2 with $\mathrm{V}_2 = A_2 t_2$ is

$$\boldsymbol{T_{21}} = -\mu_0 V_2 \left(\mathbf{M_1} \times \mathbf{H_{21}}\right) = J_{21} \cdot \left(N_{y2} sin\theta_{\mathrm{M2}} cos\theta_{\mathrm{M1}} - N_{x2} cos\theta_{\mathrm{M2}} sin\theta_{\mathrm{M1}}\right) , \tag{4.16}$$

$$J_{12} = \mu_0 V_1 \frac{r M_{S1} M_{S2}}{2} \quad \text{and} \quad J_{21} = \mu_0 V_2 \frac{r M_{S1} M_{S2}}{2} . \tag{4.17}$$

where J_{12} and J_{21} are the dipole coupling constants and parameterize the torque for FM layers of different materials and thicknesses. Normally the areas of both layers would be equal and the volumes would differ only due to the thicknesses, t_1 and t_2.

4.3 Two-dimensional magnetization dynamics

The dynamic magnetic response of a small magnetic element such as the free layer is described by the Landau-Lifshitz-Gilbert (LLG) equation [78], equation 4.18 where $\mathbf{M}$, the magnetization and $\mathbf{H}$, the effective magnetic field are, in general, vectors in three dimensions, γ_0 is the gyromagnetic constant $\gamma_0 = \mu_0 \gamma \left(\frac{\mathrm{m}}{\mathrm{A \cdot s}}\right)$, and α is the Gilbert damping parameter for the material.

$$\frac{d\mathbf{M}}{dt} = -\gamma_0 \left(\mathbf{M} \times \mathbf{H}\right) + \frac{\alpha}{|\mathbf{M}|} \mathbf{M} \times \frac{d\mathbf{M}}{dt} \tag{4.18}$$

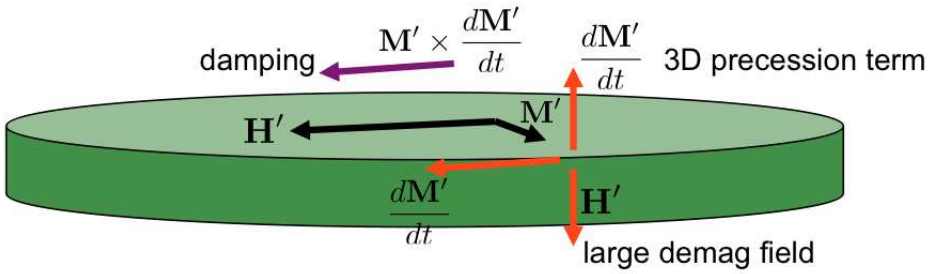

Figure 4.4: 2-D effective damping in precessional dynamics. The precessional term is pushed out of the thin film plane, but the large out-of-plane demagnetizing field pulls it back in-plane in the direction of the damping.

The first term on the right-hand-side (RHS) is recognized as the magnetic precession of the moment due to the applied field $\mathbf{H}$ (from equation 2.10) , while the second term represents the damping experienced by the magnetization's precession which will eventually align the magnetization with the applied field. For thin films, shape anisotropy forces the magnetization vector to lie principally in the plane and an effective in-plane magnetization dynamic can be found [79, 80]

$$\frac{d\mathbf{M}'}{dt} = -\frac{\gamma_0}{M_S}\left(\alpha + \frac{1}{\alpha}\right)\mathbf{M}' \times (\mathbf{M}' \times \mathbf{H}') \tag{4.19}$$

for $\mathbf{M}' = (\mathrm{M_x}, \mathrm{M_y})$ and $\mathbf{H}' = (\mathrm{H_x}, \mathrm{H_y})$ restricted to the film plane, and the magnitude of $\mathbf{M}$ remains constant ($|\mathbf{M}| \equiv M_S$). Figure 4.4 is an illustration of Cervera and Kohns' work which reveals that the three-dimensional (3-D) precessional term $\mathbf{M} \times \mathbf{H}$ gets converted, in the thin-film limit, to a two-dimensional (2-D) damping term proportional to $1/\alpha$, increasing the 2-D effective damping and essentially causing the precession term to act as a damping term.

The magnetic elements are modeled as a single magnetic domain. Since the magnitude of $\mathbf{M}$ must remain constant, it is simpler to normalize $\mathbf{M}'$ by its magnitude as $\frac{\mathbf{M}'}{M_S} = \mathbf{m}'$ and to describe the magnetization vector only by its angle, θ_M, with respect to the x axis. First the precession dynamic term on the RHS of 4.19 is expanded using $\mathbf{m}' = cos\theta_M\hat{\mathbf{x}} + sin\theta_M\hat{\mathbf{y}}$:

$$\mathbf{m}' \times (\mathbf{m}' \times \mathbf{H}') = (\mathrm{H_y}\, cos\theta_M\, sin\theta_M - \mathrm{H_x} sin^2\theta_M)\hat{\mathbf{x}} - (\mathrm{H_y}\, cos^2\theta_M - \mathrm{H_x}\, cos\theta_M\, sin\theta_M)\hat{\mathbf{y}}\,. \tag{4.20}$$

The left-hand-side (LHS) of 4.19 is transformed by using

$$\frac{d\mathbf{m}'}{dt} = \frac{d\mathbf{m}'}{d\theta_M} \cdot \frac{d\theta_M}{dt} \tag{4.21}$$

where

$$\frac{d\mathbf{m}'}{d\theta_M} = -sin\theta_M \hat{\mathbf{x}} + cos\theta_M \hat{\mathbf{y}}\,,$$

and both the LHS and RHS are multiplied by their transposes or inverses. The dynamics expression is then written as

$$\tfrac{d\theta_M}{dt} = -\gamma_0 \left(\alpha + \tfrac{1}{\alpha}\right) \times$$
$$\left[(\mathrm{H_y}\, cos\theta_M\, sin\theta_M - \mathrm{H_x} sin^2\theta_M)\hat{\mathbf{x}} - (\mathrm{H_y}\, cos^2\theta_M - \mathrm{H_x} cos\theta_M\, sin\theta_M)\hat{\mathbf{y}}\right] \cdot (-sin\theta_M \hat{\mathbf{x}} + cos\theta_M \hat{\mathbf{y}})^{\mathrm{T}}$$

which becomes

$$\begin{aligned} \frac{1}{\gamma_0 \left(\alpha + \frac{1}{\alpha}\right)} \frac{d\theta_M}{dt} &= \mathrm{H_y} cos\theta_M\, sin^2\theta_M - \mathrm{H_x} sin^3\theta_M - \mathrm{H_x} cos^2\theta_M\, sin\theta_M + H_y cos^3\theta_M \\ &= \mathrm{H_y} cos\theta_M \left(sin^2\theta_M + cos^2\theta_M\right) - \mathrm{H_x} sin\theta_M \left(sin^2\theta_M + cos^2\theta_M\right)\,, \end{aligned}$$

and finally takes the form of an effective field,

$$\frac{1}{\gamma_0 \left(\alpha + \frac{1}{\alpha}\right)} \frac{d\theta_M}{dt} = (\mathrm{H_y} cos\theta_M - \mathrm{H_x} sin\theta_M)\,. \tag{4.22}$$

Equation 4.22 can be cast equivalently as a sum of torques acting on the magnetic moment by rearranging and multiplying both sides by $\mu_0 V M_S$:

$$0 = \mu_0 V M_S\, (\mathrm{H_y} cos\theta_M - \mathrm{H_x} sin\theta_M) - \frac{\mu_0 V M_S}{\gamma_0 \left(\alpha + \frac{1}{\alpha}\right)} \frac{d\theta_M}{dt} \quad [\mathrm{J}] \tag{4.23}$$

and

$$\mathbf{T_{dyn}} = \frac{\mu_0 V M_S}{\gamma_0 \left(\alpha + \frac{1}{\alpha}\right)} \frac{d\theta_M}{dt}\,. \tag{4.24}$$

The first term in parentheses in equation 4.23 is recognized from equation 4.6 as the torque due to external applied fields and the final dynamic term is the (2-D) combined precessional and damping torque. The form of equation 4.23 is used in the spin valve and toggle MRAM systems discussed in sections 5.1 and 5.2 . With the dynamic 2-D torque term defined, it is now simple to add other previously-derived torque terms to the models in a torque balance form.

4.4 Effective fields of three-dimensional systems

The model components of the 3-D spin valve system are analogous to all the 2-D model components in that an energy or torque expression is developed for an effective field, but in the method that follows, it is the effective field (directly proportional to torque) that is used to find the change in the magnetic moment. However, the different effective fields are summed together in one module [81, 82, 75]. This method seems to be more tractable from the standpoint of the simulation software, but is less desirable in terms of modular device construction. In Chapter 5, it is convenient and intuitive to connect appropriate system nodes together with blocks representing the torque between those nodes. In what follows, this ability is lost, combining all the system torques into a total effective field term, which is used in the 3-D single domain LLG block in Figure 4.5. Even though the model method is effective, it may be more useful in the future to use the field and torque expressions derived below in a modified manner to allow for block modularization as in the 2-D model.

4.5 Mathematical development of a three-dimensional system equation

In this section the LLG equation is transformed from cartesian to spherical coordinates and cast in a form like that of equation 4.22 in order that the change of the magnetic moment in time is expressed fully by its change in angle with respect to an anisotropy or easy axis. First, the

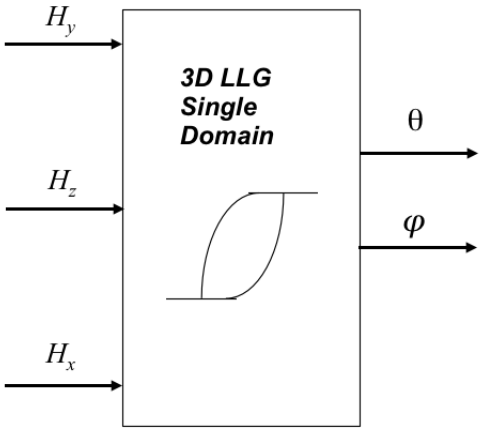

Figure 4.5: Single model block containing all interaction equations for the 3-D device model.

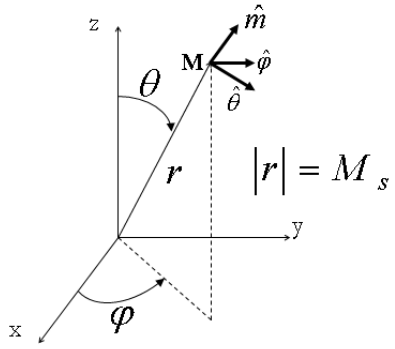

Figure 4.6: Spherical coordinate system and angles: θ is the polar angle with respect to the **z**-axis, and φ is the azimuthal angle in the x-y plane.

rotational coordinate system with respect to the fixed, cartesian coordinates is defined by the angles θ and φ in Figure 4.6. This is a more intuitive coordinate system in which to model the precession of the magnetic moment because the length of the radial vector, $\mathbf{r}$, is the magnitude of $\mathbf{M}$ which is constant at its saturation magnetization M_S, requiring only the two angle variables to describe the motion. The magnetization can be normalized by M_S and its path followed on a unit sphere as it changes in the polar and azimuthal directions represented by θ and φ respectively. First some foundational work must be done to describe the unit vectors of the rotational system. To begin, the time rate of change of the magnetization $\frac{d\mathbf{M}}{dt}$ is described with the position vector

for $\mathbf{M}$:

$$\mathbf{M} = \begin{bmatrix} M_S sin\theta cos\varphi\, \hat{\mathbf{x}} \\ M_S sin\theta sin\varphi\, \hat{\mathbf{y}} \\ M_S cos\theta\, \hat{\mathbf{z}} \end{bmatrix} \tag{4.25}$$

and $\mathbf{M}$ changes with time as

$$\frac{d\mathbf{M}}{dt} = \frac{\partial \mathbf{M}}{\partial \mathbf{r}}\frac{d\mathbf{r}}{dt} + \frac{\partial \mathbf{M}}{\partial \theta}\frac{d\theta}{dt} + \frac{\partial \mathbf{M}}{\partial \varphi}\frac{d\varphi}{dt}\,. \tag{4.26}$$

In this case, $\mathbf{r}$ is the length or magnitude of the magnetization vector, M_S, according to the fundamental constraint of ferromagnets that $|\mathbf{M}(\mathbf{r},t)| = M_S$, so that the first term on the RHS of eqn. 4.26 is $\frac{\partial \mathbf{M}}{\partial M_S}\frac{dM_S}{dt}$. The partial derivative terms are contained in the unit vectors as

$$\hat{\mathbf{e}}_m = \frac{\partial \mathbf{M}}{\partial M_S}\frac{1}{\left|\frac{\partial \mathbf{M}}{\partial M_S}\right|} = \frac{\partial \mathbf{M}}{\partial M_S}, \quad \hat{\mathbf{e}}_\theta = \frac{\partial \mathbf{M}}{\partial \theta}\frac{1}{\left|\frac{\partial \mathbf{M}}{\partial \theta}\right|} = \frac{1}{M_s}\frac{\partial \mathbf{M}}{\partial \theta}, \quad and \quad \hat{\mathbf{e}}_\varphi = \frac{\partial \mathbf{M}}{\partial \varphi}\frac{1}{\left|\frac{\partial \mathbf{M}}{\partial \varphi}\right|} = \frac{1}{M_S sin\theta}\frac{\partial \mathbf{M}}{\partial \varphi}\,. \tag{4.27}$$

This allows the scale factors for each unit vector to be clearly understood and the variation of the magnetization with respect to M_S, θ and φ to be written in terms of the unit vectors as:

$$\hat{\mathbf{e}}_m = \frac{\partial \mathbf{M}}{\partial M_S}, \quad M_S\hat{\mathbf{e}}_\theta = \frac{\partial \mathbf{M}}{\partial \theta}, \quad \text{and} \quad M_S sin\theta\, \hat{\mathbf{e}}_\varphi = \frac{\partial \mathbf{M}}{\partial \varphi}.$$

Applying this coordinate system in equation 4.26 one can write

$$\frac{d\mathbf{M}}{dt} = \dot{M}_S\hat{\mathbf{e}}_m + M_S\dot{\theta}\,\hat{\mathbf{e}}_\theta + M_S sin\theta\,\dot{\varphi}\,\hat{\mathbf{e}}_\varphi \tag{4.28}$$

with the dot representing the time-derivative of the variable. The Landau-Lifshitz-Gilbert (LLG) equation in the Gilbert form is

$$\frac{d\mathbf{M}}{dt} = -\gamma_0\left(\mathbf{M}\times\mathbf{H_{eff}}\right) + \frac{\alpha}{M_S}\left(\mathbf{M}\times\frac{d\mathbf{M}}{dt}\right). \tag{4.29}$$

A system of equations is formulated for $\frac{d\mathbf{M}}{dt}$ using equation 4.28 as the LHS and eqn. 4.29 as the RHS. The two RHS terms in equation 4.29 are expanded first as

$$\mathbf{M} \times \mathbf{H_{eff}} = M_S \hat{\mathbf{e}}_m \times [(\mathbf{H_{eff}} \cdot \hat{\mathbf{e}}_m) + (\mathbf{H_{eff}} \cdot \hat{\mathbf{e}}_\theta) + (\mathbf{H_{eff}} \cdot \hat{\mathbf{e}}_\varphi)]$$

$$= \begin{bmatrix} \hat{\mathbf{e}}_m & \hat{\mathbf{e}}_\theta & \hat{\mathbf{e}}_\varphi \\ M_S & 0 & 0 \\ (\mathbf{H_{eff}} \cdot \hat{\mathbf{e}}_m) & (\mathbf{H_{eff}} \cdot \hat{\mathbf{e}}_\theta) & (\mathbf{H_{eff}} \cdot \hat{\mathbf{e}}_\varphi) \end{bmatrix}$$

$$= M_S(\mathbf{H_{eff}} \cdot \hat{\mathbf{e}}_\theta)\hat{\mathbf{e}}_\varphi - M_S(\mathbf{H_{eff}} \cdot \hat{\mathbf{e}}_\varphi)\hat{\mathbf{e}}_\theta \tag{4.30}$$

and

$$\mathbf{M} \times \frac{d\mathbf{M}}{dt} = \begin{bmatrix} \hat{\mathbf{e}}_m & \hat{\mathbf{e}}_\theta & \hat{\mathbf{e}}_\varphi \\ M_S & 0 & 0 \\ \dot{M_S} & M_S\dot{\theta} & M_S sin\theta\, \dot{\varphi} \end{bmatrix}$$

$$= M_S^2\, \dot{\theta}\, \hat{\mathbf{e}}_\varphi - M_S^2\, sin\theta\, \dot{\varphi}\, \hat{\mathbf{e}}_\theta\,. \tag{4.31}$$

Putting equation4.28 and the expanded LLG terms from equations 4.30 and 4.31 together in matrix form yields

$$\begin{bmatrix} \dot{M_S}\hat{\mathbf{e}}_m \\ M_S\dot{\theta}\, \hat{\mathbf{e}}_\theta \\ M_S sin\theta\, \dot{\varphi}\, \hat{\mathbf{e}}_\varphi \end{bmatrix} = \begin{bmatrix} 0 \\ \left(\gamma_0 M_S(\mathbf{H_{eff}} \cdot \hat{\mathbf{e}}_\varphi) - \frac{\alpha}{M_S}(M_S^2\, sin\theta\, \dot{\varphi})\right) \hat{\mathbf{e}}_\theta \\ \left(-\gamma_0 M_S(\mathbf{H_{eff}} \cdot \hat{\mathbf{e}}_\theta) + \frac{\alpha}{M_S}(M_S^2\, \dot{\theta})\right) \hat{\mathbf{e}}_\varphi \end{bmatrix} \tag{4.32}$$

but the terms with $\mathbf{H_{eff}}$ must also be expanded. This is done in terms of the change in total energy with the change in magnetization. The total energy is defined as

$$E = -\mu_0 V \mathbf{M} \mathbf{H_{eff}}$$

and $\mathbf{H_{eff}}$ can be expressed as

$$\mathbf{H_{eff}} = -\frac{1}{\mu_0 V}\frac{\partial E}{\partial \mathbf{M}}\,.$$

Thus, $\gamma_0 M_S(\mathbf{H_{eff}}\cdot\hat{\mathbf{e}}_\varphi) = \gamma_0 M_S \cdot \left(-\frac{1}{\mu_0 V}\frac{\partial E}{\partial \mathbf{M}}\right)\left(\frac{\partial \mathbf{M}}{\partial \varphi}\frac{1}{M_S sin\theta}\right)$ recalling that $\hat{\mathbf{e}}_\varphi = \frac{1}{M_S sin\theta}\frac{\partial \mathbf{M}}{\partial \varphi}$. Similarly for -$\gamma_0 M_S(\mathbf{H_{eff}}\cdot\hat{\mathbf{e}}_\theta)$ it is seen that $-\gamma_0 M_S(\mathbf{H_{eff}}\cdot\hat{\mathbf{e}}_\theta) = -\gamma_0 M_S \cdot \left(-\frac{1}{\mu_0 V}\frac{\partial E}{\partial \mathbf{M}}\right)\left(\frac{\partial \mathbf{M}}{\partial \theta}\frac{1}{M_S}\right)$. These two $\mathbf{H_{eff}}$ terms now look like

$$\gamma_0 M_S(\mathbf{H_{eff}}\cdot\hat{\mathbf{e}}_\varphi) = -\frac{\gamma_0}{\mu_0 V sin\theta}\frac{\partial E}{\partial \varphi} \qquad \text{and} \qquad -\gamma_0 M_S(\mathbf{H_{eff}}\cdot\hat{\mathbf{e}}_\theta) = \frac{\gamma_0}{\mu_0 V}\frac{\partial E}{\partial \theta}$$

and equation 4.32 can be rewritten

$$\begin{bmatrix} \dot{M}_S\hat{\mathbf{e}}_m \\ M_S\dot{\theta}\,\hat{\mathbf{e}}_\theta \\ M_S sin\theta\,\dot{\varphi}\,\hat{\mathbf{e}}_\varphi \end{bmatrix} = \begin{bmatrix} 0 \\ \left(-\frac{\gamma_0}{\mu_0 V sin\theta}\frac{\partial E}{\partial \varphi} - \alpha M_S sin\theta\,\dot{\varphi}\right)\hat{\mathbf{e}}_\theta \\ \left(\frac{\gamma_0}{\mu_0 V}\frac{\partial E}{\partial \theta} + \alpha M_S\dot{\theta}\right)\hat{\mathbf{e}}_\varphi \end{bmatrix}. \tag{4.33}$$

Finally we arrive at two equations in $\dot{\theta}$ and $\dot{\varphi}$:

$$M_S\dot{\theta} = -\frac{\gamma_0}{\mu_0 V sin\theta}\frac{\partial E}{\partial \varphi} - \alpha M_S sin\theta\,\dot{\varphi} \tag{4.34}$$

$$M_S sin\theta\,\dot{\varphi} = \frac{\gamma_0}{\mu_0 V}\frac{\partial E}{\partial \theta} + \alpha M_S\dot{\theta} \tag{4.35}$$

and isolating $\dot{\theta}$ and $\dot{\varphi}$ on the LHS of equations 4.34 and 4.35 respectively,

$$\dot{\theta} = -\frac{\gamma_0}{\mu_0 V M_S\, sin\theta}\frac{\partial E}{\partial \varphi} - \alpha\, sin\theta\,\dot{\varphi} \tag{4.36}$$

$$\dot{\varphi} = \frac{\gamma_0}{\mu_0 V M_S\, sin\theta}\frac{\partial E}{\partial \theta} + \frac{\alpha}{sin\theta}\dot{\theta}\,. \tag{4.37}$$

Substituting the RHS of equation 4.37 for $\dot{\varphi}$ in equation 4.36, we get the result

$$\dot{\theta} = -\frac{\gamma_0}{\mu_0 V M_S sin\theta}\frac{\partial E}{\partial \varphi} - \alpha sin\theta\left(\frac{\gamma_0}{\mu_0 V M_S sin\theta}\frac{\partial E}{\partial \theta} + \frac{\alpha}{sin\theta}\dot{\theta}\right)$$

$$\dot{\theta} = -\frac{\gamma_0}{\mu_0 V M_S sin\theta}\frac{\partial E}{\partial \varphi} - \frac{\alpha\gamma_0}{\mu_0 V M_S}\frac{\partial E}{\partial \theta} - \alpha^2\dot{\theta}$$

$$\dot{\theta}(1+\alpha^2) = -\frac{\gamma_0}{\mu_0 V M_S}\frac{1}{sin\theta}\frac{\partial E}{\partial \varphi} - \frac{\alpha\gamma_0}{\mu_0 V M_S}\frac{\partial E}{\partial \theta}$$

$$\dot{\theta}(1+\alpha^2) = \frac{\gamma_0}{\mu_0 V M_S}\left[-\frac{1}{sin\theta}\frac{\partial E}{\partial \varphi} - \alpha\frac{\partial E}{\partial \theta}\right]. \tag{4.38}$$

Likewise, substituting the RHS of equation 4.36for $\dot{\theta}$ in equation 4.37, we find that

$$\dot{\varphi} = \frac{\gamma_0}{\mu_0 V M_S sin\theta}\frac{\partial E}{\partial \theta} + \frac{\alpha}{sin\theta}\left(-\frac{\gamma_0}{\mu_0 V M_S sin\theta}\frac{\partial E}{\partial \varphi} - \alpha\, sin\theta\,\dot{\varphi}\right)$$

$$= \frac{\gamma_0}{\mu_0 V M_S sin\theta}\frac{\partial E}{\partial \theta} - \frac{\alpha\gamma_0}{\mu_0 V M_S sin^2\theta}\frac{\partial E}{\partial \varphi} - \alpha^2\dot{\varphi}$$

$$\dot{\varphi}(1+\alpha^2) = \frac{\gamma_0}{\mu_0 V M_S}\frac{1}{sin\theta}\left[-\frac{\alpha}{sin\theta}\frac{\partial E}{\partial \varphi} + \frac{\partial E}{\partial \theta}\right]. \tag{4.39}$$

It is noted that the terms in brackets in equations 4.38 and 4.39 are the torques experienced by the system in the θ and φ directions due to E, the total free energy that is present. If the convention is taken that the effective fields in θ and φ are

$$\mathrm{H}_\theta = -\frac{1}{\mu_0 V M_S}\frac{\partial E}{\partial \theta} \quad \text{and} \quad \mathrm{H}_\varphi = -\frac{1}{\mu_0 V M_S\, sin\theta}\frac{\partial E}{\partial \varphi},$$

then we can write the result from equations 4.38 and 4.39 in terms of H_θ and H_φ as follows:

$$\frac{d\theta}{dt} = \frac{\gamma_0}{(1+\alpha^2)}\left[H_\varphi + \alpha H_\theta\right] \tag{4.40}$$

$$\frac{d\varphi}{dt} = \frac{\gamma_0}{(1+\alpha^2)}\frac{1}{sin\theta}\left[\alpha H_\varphi - H_\theta\right] \tag{4.41}$$

Equations 4.40 and 4.41 match expressions found in the literature [82] for the angular velocity of the magnetization due to an effective magnetic field .

The torques of equations 4.38 and 4.39 are scaled by $-\frac{1}{\mu_0 V M_S}$ to convert them into effective fields in A/m, denoted as H_θ and H_φ, and the gyromagnetic ratio, $\gamma = \frac{2.21\times10^5}{1+\alpha^2}\left(\frac{\mathrm{m}}{\mathrm{As}}\right)$ multiplied by the effective field terms yields the rate of change of the moment in θ and φ. One can see that these expressions of angular velocity fold together all the magnetostatic and anisotropy terms with the dynamic field response in the effective field variables H_θ and H_φ. Therefore, to use equations 4.40 and 4.41 in Verilog-A, the torques derived earlier must be transformed into the defined spherical coordinate system in Figure 4.6, which is done next.

4.6 Energy and effective fields for three-dimensional models

Relating the 2-D terms in spherical coordinates is done with three kinds of manipulations:

1. If the 2-D term is expressed with magnetization ($\mathbf{M}$) components in the $\hat{\mathbf{x}}$, and/or $\hat{\mathbf{y}}$, and/or $\hat{\boldsymbol{z}}$ directions, the components of the position vector in equation 4.25 replace the cartesian components, *eg.*, $\mathbf{M_x} = M_S sin\theta\, cos\varphi\,\hat{\mathbf{i}}$, remembering that now θ and φ are the polar and azimuthal angles of the spherical coordinate system.

2. If a vector term other than $\mathbf{M}$ must be portioned into the θ and φ directions, a dot product can be taken between the vector term and $\hat{\mathbf{e}}_\theta$ and/or $\hat{\mathbf{e}}_\varphi$. The spherical unit vectors $\hat{\mathbf{e}}_\theta$ and $\hat{\mathbf{e}}_\varphi$ were defined in equation 4.27 and are $\hat{\mathbf{e}}_\theta = cos\theta cos\varphi\hat{\mathbf{i}} + cos\theta sin\varphi\hat{\mathbf{j}} - sin\theta\hat{\mathbf{k}}$, and $\hat{\mathbf{e}}_\varphi = -sin\varphi\hat{\mathbf{i}} + cos\varphi\hat{\mathbf{j}}$.

3. To represent an angle between two vectors (as for the dipole or exchange coupling terms), a dot product of the two vectors must be performed in spherical coordinates.

In addition to transforming the expressions for torque in cartesian to torque in spherical coordinates, each term is divided by $\mu_0 V M_S$ or $\mu_0 V M_S sin\theta$ as appropriate, in order to give it the correct units as an effective field in the θ and φ directions. These field terms are then used in equations 4.40 and 4.41.

Two vector definitions are given in the Verilog-A code, one for the easy axis which has a default setting

$$\hat{\mathbf{ea}} = \left(1\hat{\mathbf{i}},\, 0\hat{\mathbf{j}},\, 0\hat{\mathbf{k}}\right) , \tag{4.42}$$

but the vector components can be set to any direction, as long as the magnitude of $\hat{\mathbf{ea}} = 1$. The other definition is for $\mathbf{M}$ and has already been given in equation 4.25, but in the Verilog-A code it is used as the unit vector $\frac{\mathbf{M}}{M_S} = (sin\theta\, cos\varphi\, \hat{\mathbf{i}},\, sin\theta\, sin\varphi\, \hat{\mathbf{j}},\, cos\theta\, \hat{\mathbf{k}}) = \hat{\mathbf{m}}$.

4.6.1 Uniaxial crystalline anisotropy

This anisotropy depends upon the angle between the magnetic moment and the easy axis, where originally θ_M was the angle in

$$E_k = K_u V sin^2\theta_{\mathrm{M}} \,, \text{ and } T_{anis} = K_u V sin2\theta_M \,. \tag{4.43}$$

Now the angle will be designated as ψ as it depends on both θ and φ, and is

$$\psi = cos^{-1}(\hat{\mathbf{ea}} \cdot \hat{\mathbf{m}}) = cos^{-1}\mathbf{u} \,, \tag{4.44}$$

where $\hat{\mathbf{ea}} \cdot \hat{\mathbf{m}} = \mathbf{u} = \mathrm{ea_i m_i} + \mathrm{ea_j m_j} + \mathrm{ea_k m_k} = \mathrm{ea_i} sin\theta\, cos\varphi + \mathrm{ea_j} sin\theta\, sin\varphi + \mathrm{ea_k} cos\theta$. The derivatives of the energy function in equation 4.43 are needed for the effective field:

$$\frac{\partial E_k}{\partial \theta} = \frac{\partial}{\partial \psi}\left(K_u V sin^2\psi\right)\frac{\partial \psi}{\partial \theta}$$

$$\frac{\partial E_k}{\partial \varphi} = \frac{\partial}{\partial \psi}\left(K_u V sin^2\psi\right)\frac{\partial \psi}{\partial \varphi},$$

where first it is easy to see that the common term, $\frac{\partial}{\partial \psi}\left(K_u V sin^2\psi\right) = K_u V sin2\psi$ as before. To find $\frac{\partial \psi}{\partial \theta}$ and $\frac{\partial \psi}{\partial \varphi}$ the chain rule is used

$$\frac{\partial \psi}{\partial \theta} = \frac{\partial \psi}{\partial \mathbf{u}}\frac{\partial \mathbf{u}}{\partial \theta}$$

recognizing that

$$\frac{\partial \psi}{\partial \theta} = \frac{\partial}{\partial \mathbf{u}}(cos^{-1}\mathbf{u})\frac{\partial \mathbf{u}}{\partial \theta} = \frac{-1}{\sqrt{1-\mathrm{u}^2}}\left(\mathrm{ea_i} cos\theta\, cos\varphi + \mathrm{ea_j} cos\theta\, sin\varphi - \mathrm{ea_k} sin\theta\right),$$

and in the same manner a similar expression for $\frac{\partial \psi}{\partial \varphi}$ is found. This leads to the torques in both θ and φ as

$$\frac{\partial E_k}{\partial \theta} = K_u V sin2\psi \cdot \frac{-1}{\sqrt{1-\mathrm{u}^2}}\left(\mathrm{ea_i} cos\theta\, cos\varphi + \mathrm{ea_j} cos\theta\, sin\varphi - \mathrm{ea_k} sin\theta\right), \tag{4.45}$$

$$\frac{\partial E_k}{\partial \varphi} = K_u V sin2\psi \cdot \frac{-1}{\sqrt{1-\mathrm{u}^2}}\left(-\mathrm{ea_i} sin\theta\, sin\varphi + \mathrm{ea_j} sin\theta\, cos\varphi\right). \tag{4.46}$$

Using the definition of the effective field:

$$\mathrm{H}_\theta = -\frac{1}{\mu_0 V M_S}\frac{\partial E}{\partial \theta} \quad and \quad \mathrm{H}_\varphi = -\frac{1}{\mu_0 V M_S}\frac{1}{sin\theta}\frac{\partial E}{\partial \varphi},$$

the effective fields for the uniaxial crystalline anisotropy are

$$\mathrm{H}_{k\theta} = \frac{K_u sin2\psi}{\mu_0 M_S} \cdot \frac{1}{\sqrt{1-\mathrm{u}^2}}\left(\mathrm{ea_i} cos\theta\, cos\varphi + \mathrm{ea_j} cos\theta\, sin\varphi - \mathrm{ea_k} sin\theta\right), \tag{4.47}$$

and

$$\mathrm{H}_{k\varphi} = \frac{K_u sin2\psi}{\mu_0 M_S sin\theta} \cdot \frac{1}{\sqrt{1-\mathrm{u}^2}} \left(-\mathrm{ea_i} sin\theta\, sin\varphi + \mathrm{ea_j} sin\theta\, cos\varphi\right) . \tag{4.48}$$

4.6.2 Applied field or Zeeman energy

The energy due to the applied field $\mathbf{H_a}$ in the $\hat{\mathbf{x}}, \hat{\mathbf{y}}$, and $\hat{\mathbf{z}}$ directions is

$$E_a = -\mu_0 V \left(\mathrm{M_x H_x} + \mathrm{M_y H_y} + \mathrm{M_z H_z}\right) ,$$

where $\mathrm{M_x} = M_S sin\theta cos\varphi$, etc..., for the magnetization components in spherical coordinates, so that

$$E_a = -\mu_0 V M_S \left(\mathrm{H_x} sin\theta\, cos\varphi + \mathrm{H_y} sin\theta\, sin\varphi + \mathrm{H_z} cos\theta\right) ,$$

and the torques are

$$\frac{\partial E_a}{\partial \theta} = -\mu_0 V M_S \left(\mathrm{H_x} cos\theta\, cos\varphi + \mathrm{H_y} cos\theta\, sin\varphi - \mathrm{H_z} sin\theta\right)$$

and

$$\frac{\partial E_a}{\partial \varphi} = \mu_0 V M_S sin\theta \left(\mathrm{H_x} sin\varphi - \mathrm{H_y} cos\varphi\right) .$$

These are scaled as before to effective fields as

$$\mathrm{H_{a\theta}} = \left(\mathrm{H_x} cos\theta\, cos\varphi + \mathrm{H_y} cos\theta\, sin\varphi - \mathrm{H_z} sin\theta\right) \tag{4.49}$$

and

$$\mathrm{H_{a\varphi}} = \left(\mathrm{H_y} cos\varphi - \mathrm{H_x} sin\varphi\right) . \tag{4.50}$$

4.6.3 Shape anisotropy

The shape anisotropy results in an energy responsible for the demagnetization field within the free layer and is the product of the magnetization **M** with the demagnetization tensor **N**. A free layer of NiFe with elliptical shape is assumed for which the tensor has only diagonal elements in the $\hat{\mathbf{x}}, \hat{\mathbf{y}}$, and $\hat{\mathbf{z}}$ directions. In simulation the demagnetization factors $\mathrm{N}_x = 0.0182$, $\mathrm{N}_y = 0.0515$, and $\mathrm{N}_z = 0.931$ from [83] are used. The demagnetizing field internal to the free layer is

$$\mathbf{H_d} = -\mathrm{N}\mathbf{M} = -\left(N_x \mathrm{M_x}\hat{\mathbf{i}} + N_y \mathrm{M_y}\hat{\mathbf{j}} + N_z \mathrm{M_z}\hat{\mathbf{k}}\right)$$

with an energy due to this field

$$E_d = -\mu_0 V \mathbf{M}\mathbf{H_d} = \left(N_x \mathrm{M_x^2} + N_y \mathrm{M_y^2} + N_z \mathrm{M_z^2}\right) .$$

Replacing the components of **M** with the appropriate spherical expressions, E_d becomes

$$E_d = \mu_0 V M_S^2 \left[\left(N_x - N_z\right) sin^2\theta + \left(N_y - N_x\right) sin^2\theta sin^2\varphi + N_z\right] .$$

Taking the derivative of the energy with respect to θ and φ and scaling the torques to effective fields, the resultant shape anisotropy fields are

$$\mathrm{H_{d\theta}} = -M_S sin(2\theta) \left[\left(N_x - N_z\right) + \left(N_y - N_x\right) sin^2\varphi\right] \tag{4.51}$$

and

$$\mathrm{H_{d\varphi}} = -M_S sin(2\varphi) \left(N_y - N_x\right) sin\theta \, . \tag{4.52}$$

4.7 Spin transfer torque (STT)

The magnetization dynamics of a ferromagnetic free layer can also be manipulated by an effect called spin transfer torque (STT). In this effect a spin-polarized current flowing perpendicular to the magnetic multilayers may transfer spin angular momentum between layers resulting in a torque on the magnetic moments of the layers. The origin of the spin transfer torque is the s-d interaction between the spin momentum of the conduction electron and the local dipole moment of the magnetic layer. The spin torque effect can give rise to local magnetization excitations such as spin wave generation [67, 39, 84], magnetic reversal or switching [38, 42], and stable precession [43, 44, 46]. The two latter effects are considered in this work. The spin transfer torque provides an electrical method to switch the layer magnetization in a magnetic-based memory or magnetologic element instead of the traditional Oersted field switching method.

The STT term is realized as the change in angular momentum of the FM layer perpendicular to that layer's original magnetization direction, due to the angular momentum imparted by the electrons that build up at the interface of the spacer layer and the FM layer when a CPP current is applied through the multilayer. The transverse component is the only component considered due to the constraint that the magnitude of $\mathbf{M}$ can not change. Figure 1.3 from Chapter 1 is redrawn in Figure 4.7 to show how a spin-polarized electron coming through the conductive spacer is acted upon by a torque in the direction $-\mathbf{M} \times (\mathbf{M} \times \hat{\mathbf{e}}_\mathbf{p})$ from the free FM layer, where $\hat{\mathbf{e}}_\mathbf{p}$ is the unit magnetization vector of the polarizing FM layer and its electrons. In order to conserve the system's angular momentum the intinerent electron reacts with a torque exactly opposite with direction $\mathbf{M} \times (\mathbf{M} \times \hat{\mathbf{e}}_\mathbf{p})$, which an electron near the interface *in* the free FM layer absorbs. When enough spin-polarized electrons interact in this manner with the FM layer's electrons, the polarized electron flow will succeed in switching the FM layer moment and align its magnetization with that of the polarizing/pinned layer. The spin torque is

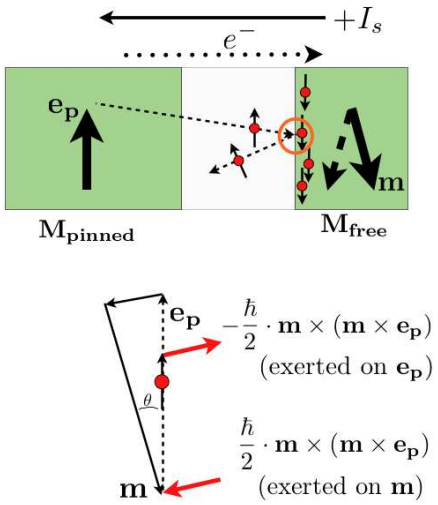

Figure 4.7: Transfer of angular momentum from spin-polarized electrons to a FM layer magnetized antiparallel to the pinned layer.

$$\begin{aligned}
\mathbf{T}_{stt} &= \frac{I_s \hbar G(\psi)}{e \cdot 2 \cdot M_S^2}\,\mathbf{M}\times(\mathbf{M}\times\hat{\mathbf{e}}_\mathbf{p}) \quad [\mathrm{J}] \quad \text{where} \\
d\mathbf{L} &= \frac{\hbar}{2 \cdot M_S^2}\,\mathbf{M}\times(\mathbf{M}\times\hat{\mathbf{e}}_\mathbf{p}) \quad [\mathrm{J{\cdot}s}] \quad \text{and} \\
\frac{I_s}{e} &= \textit{rate of electron impingement} \quad [s^{-1}]\,.
\end{aligned}$$

The spin torque expression describes the change in angular momentum $d\mathbf{L}$ of the FM layer at the rate of $\frac{I_s}{e}$ from the flow of electrons in the spin-polarized current, I_s [85, 68]. The term $G(\psi)$ reflects the device conductance and the efficiency with which the electron flow is able to travel through the spacer layer to either FM layer, and what proportion of those electrons are spin-polarized in the direction of the pinned layer. The angle ψ is the angle between the magnetization vector and the easy axis, $\hat{\mathbf{e}}_\mathbf{p}\cdot\hat{\mathbf{m}}$, in the spherical coordinate system. The spin torque term can be shown to contribute to the total magnetization change of the free layer, $\frac{d\mathbf{M}}{dt}$, as follows,

$$\frac{d\mathbf{M}}{dt} = -\gamma_0\,(\mathbf{M}\times\mathbf{H_{eff}}) + \frac{\alpha}{M_S}\left(\mathbf{M}\times\frac{d\mathbf{M}}{dt}\right) - \gamma_0\frac{I_s\hbar G(\psi)}{\mu_0 V\, M_S^2\, 2\, e}\,\mathbf{M}\times(\mathbf{M}\times\hat{\mathbf{e}}_\mathbf{p})\;\left[\frac{A}{m\cdot s}\right] \qquad (4.53)$$

where it is noted that $\frac{\mu_0 V}{\gamma_0}\frac{d\mathbf{M}}{dt} = \mathbf{T}$. The STT term can be combined as part of the effective field

term,

$$\frac{d\mathbf{M}}{dt} = \frac{\alpha}{M_S}\left(\mathbf{M}\times\frac{d\mathbf{M}}{dt}\right) - \gamma_0\mathbf{M}\times\left[\mathbf{H_{eff}} + \frac{I_s\hbar G(\psi)}{\mu_0 V\, M_S^2\, 2\, e}\left(\mathbf{M}\times\hat{\mathbf{e}}_\mathbf{p}\right)\right] \tag{4.54}$$

where the last term on the RHS of the Landau-Lifshitz-Gilbert equation is the effective STT field, $\mathbf{H_s} = \frac{1}{\mu_0\cdot V\cdot M_S}\cdot\frac{I_s\hbar G(\psi)}{M_S\cdot e\cdot 2}\left(\mathbf{M}\times\hat{\mathbf{e}}_\mathbf{p}\right)$ $[\frac{A}{m}]$. In order to use this new field term in the LLG equation in spherical coordinates, $\mathbf{H_s}$ must be separated into parts in the θ and φ directions. To deal with the $\mathbf{H_s}$ components the cross product $(\mathbf{M}\times\hat{\mathbf{e}}_\mathbf{p})$ is first computed with directional components in the $\hat{\mathbf{i}}$, $\hat{\mathbf{j}}$, and $\hat{\mathbf{k}}$ directions,

$$\begin{aligned}(\mathbf{M}\times\hat{\mathbf{e}}_\mathbf{p}) = \mathbf{F_f}(\theta,\varphi) \quad &= \quad (\mathrm{ea_y}\, cos\theta - \mathrm{ea_z} sin\theta\, sin\varphi)\,\hat{\mathbf{i}} - (\mathrm{ea_x} cos\theta - \mathrm{ea_z} sin\theta\, cos\varphi)\,\hat{\mathbf{j}} \quad (4.55)\\ &\quad + (\mathrm{ea_x} sin\theta\, sin\varphi - \mathrm{ea_y} sin\theta\, cos\varphi)\,\hat{\mathbf{k}}\,. \quad (4.56)\end{aligned}$$

$\mathbf{F_f}(\theta,\varphi)$ represents the cross product of equation 4.56 here and in the Verilog-A code. The dot product of equation 4.56 with the corresponding components of $\hat{\mathbf{e}}_\theta$ and $\hat{\mathbf{e}}_\varphi$ will be represented as $\mathbf{F_f}(\theta,\varphi)\cdot\hat{\mathbf{e}}_{\theta,\varphi}$. The magnetization direction of the polarizing/pinned layer is taken to be the in-plane easy axis already denoted as $\hat{\mathbf{ea}} = \left(\mathrm{ea_x}\hat{\mathbf{i}},\, \mathrm{ea_y}\hat{\mathbf{j}},\, \mathrm{ea_z}\hat{\mathbf{k}}\right)$, and $\mathbf{M}$ is already defined in 4.25. It was said in section 4.5 that $\mathrm{H}_{\theta,\varphi} = -\frac{1}{\mu_0 V}\frac{\partial E}{\partial \mathbf{M}}\cdot\hat{\mathbf{e}}_\theta\,,\hat{\mathbf{e}}_\varphi$, thus $(\mathbf{H_s}\cdot\hat{\mathbf{e}}_\varphi) = \mathbf{H_s}\cdot\frac{\partial\mathbf{M}}{\partial\varphi}\frac{1}{M_S sin\theta}$ noting that $\hat{\mathbf{e}}_\varphi = \frac{\partial\mathbf{M}}{\partial\varphi}\frac{1}{M_S sin\theta}$. Similarly, $(\mathbf{H_s}\cdot\hat{\mathbf{e}}_\theta) = \mathbf{H_s}\cdot\frac{\partial\mathbf{M}}{\partial\theta}\frac{1}{M_S}$ with $\hat{\mathbf{e}}_\theta = \frac{\partial\mathbf{M}}{\partial\theta}\frac{1}{M_S}$, with $\hat{\mathbf{e}}_\theta = cos\theta\, cos\varphi\hat{\mathbf{i}} + cos\theta\, sin\varphi\hat{\mathbf{j}} - sin\theta\hat{\mathbf{k}}$, and $\hat{\mathbf{e}}_\varphi = -sin\varphi\hat{\mathbf{i}} + cos\varphi\hat{\mathbf{j}}$. However, the actual magnetization vector used in the Verilog code is normalized with respect to M_S as seen in equation 4.56 so a $\frac{1}{M_S}$ term must be eliminated. The resulting expressions for $\mathbf{H}_{s\theta}$ and $\mathbf{H}_{s\varphi}$ using $\mathbf{H_s}$ and equation 4.56 are

$$\mathbf{H}_{s\theta} = \frac{1}{\mu_0\, V\, M_S}\cdot\frac{I_s\hbar G(\psi)}{2\, e}\mathbf{F_f}(\theta,\varphi)\cdot\hat{\mathbf{e}}_\theta \tag{4.57}$$

$$\mathbf{H}_{s\varphi} = \frac{1}{\mu_0\, V\, M_S}\cdot\frac{I_s\hbar G(\psi)}{2\, e}\mathbf{F_f}(\theta,\varphi)\cdot\hat{\mathbf{e}}_\varphi\,. \tag{4.58}$$

Finally, the transport and polarization efficiency factor, $G(\psi)$ must also be calculated in the model. First postulated by Slonczewski according to material and geometric parameters [86, 68],

this factor is described in the form of equation 4.59 by [87] as

$$G(\psi) = \left[-4 + (1+P)^3 \cdot \frac{3 + (\hat{\mathbf{e}}_\mathbf{p} \cdot \hat{\mathbf{m}})}{4P^{\frac{3}{2}}}\right]^{-1} \tag{4.59}$$

where P is the spin-polarization factor of the incident current and has typical values of $P \simeq 0.3 - 0.4$ in ferromagnetic metals. In the STT model $G(\psi)$ is computed using the dot product of $\hat{\mathbf{ea}}$ with $\hat{\mathbf{m}}$, and $P = 0.35$.

4.8 The 3-D model

We have gone through a lot of math to derive a three dimensional dynamics expression made from the combination of equations 4.40 and 4.41, and several key effective field terms; uniaxial crystalline anisotropy in equations 4.47 and 4.48, Zeeman field in equations 4.49 and 4.50, shape anisotropy in equations 4.51 and 4.52, and STT fields in equations 4.57 and 4.58. The 3-D model takes all the effective field terms and combines them as H_θ and H_φ in equations 4.40 and 4.41, repeated here for convience,

$$\frac{d\theta}{dt} = \frac{\gamma_0}{(1+\alpha^2)}\left[\mathrm{H}_\varphi + \alpha \mathrm{H}_\theta\right]$$

$$\frac{d\varphi}{dt} = \frac{\gamma_0}{(1+\alpha^2)}\frac{1}{sin\theta}\left[\alpha \mathrm{H}_\varphi - \mathrm{H}_\theta\right]$$

as

$$\begin{aligned}
\mathrm{H}_\theta \quad = \quad & \frac{K_u sin2\psi}{\mu_0 M_S} \cdot \frac{1}{\sqrt{1-\mathrm{u}^2}}\left(\mathrm{ea_i} cos\theta\, cos\varphi + \mathrm{ea_j} cos\theta\, sin\varphi - \mathrm{ea_k} sin\theta\right) \\
& + \left(\mathrm{H_x} cos\theta\, cos\varphi + \mathrm{H_y} cos\theta\, sin\varphi - \mathrm{H_z} sin\theta\right) \\
& - M_S sin(2\theta)\left[(N_x - N_z) + (N_y - N_x)\, sin^2\varphi\right] \\
& \frac{1}{\mu_0 \cdot V \cdot M_S} \cdot \frac{I_s \hbar G(\psi)}{e \cdot 2} \mathbf{F_f}(\theta, \varphi) \cdot \hat{\mathbf{e}}_\theta
\end{aligned}$$

and

$$\begin{aligned} \mathrm{H}_{\varphi} &= \frac{K_u sin2\psi}{\mu_0 M_S sin\theta} \cdot \frac{1}{\sqrt{1-\mathrm{u}^2}} \left(-\mathrm{ea_i} sin\theta\, sin\varphi + \mathrm{ea_j} sin\theta\, cos\varphi\right) \\ &\quad + \left(\mathrm{H_y} cos\varphi - \mathrm{H_x} sin\varphi\right) \\ &\quad - M_S sin(2\varphi)\left(N_y - N_x\right) sin\theta \\ &\quad \frac{1}{\mu_0 \cdot V \cdot M_S} \cdot \frac{I_s \hbar G(\psi)}{e \cdot 2} \mathbf{F_f}(\theta,\varphi) \cdot \hat{\mathbf{e}}_{\varphi}\,. \end{aligned}$$

The final term in each expression is the STT term which is further expanded in terms of $\mathbf{F_f}(\theta,\varphi)\cdot\hat{\mathbf{e}}_{\theta}$ and $\mathbf{F_f}(\theta,\varphi)\cdot\hat{\mathbf{e}}_{\varphi}$ in the Verilog-A code. It is apparent here that with all the terms combined into one equation for determining the magnetization angles $\mathbf{M}(\theta)$ and $\mathbf{M}(\varphi)$, it is no longer possible to keep torque terms in individual circuit modules and combine them for a specific device.

Chapter 5 – Spin valve, toggle MRAM, and STT systems

Brief descriptions of a spin valve, toggle MRAM and a spin torque transfer system were given earlier in the introduction, and the torques and fields needed to build the Verilog-A models have been developed for each of those systems. In this chapter more detail is provided about each system; signals and operation, and the composition of each Verilog-A model. The spin valve and toggle MRAM systems use 2-D magnetization statics and dynamics while the STT system uses the 3-D magnetization model.

Some portions of the Verilog-A code will be given in this chapter. In order to model magnetic behaviors, a new *discipline* (a collection of related physical signal types, *eg.*, current and voltage, or angle and angular force) has been defined for magnetic fields with an appropriate *nature* (a set of attributes) such as units of $\left[\frac{\mathrm{A}}{\mathrm{m}}\right]$ and the access term H( ) as in H(hx), for accessing the magnetic field signals. The magnetization angles and torque belong to a *rotational discipline* with *natures* of angle and angular force respectively. Thus to use or access the angle θ_{M1}, the code uses the access term Theta( ) or Theta(M1). The *nature* of angular force is used to describe torque. Torque can be accessed with the term Tau( ) as in Tau(M1). In this way, the various physical terms comprising a signal simply "contribute" to the signal using the Verilog-A symbol, <+ . In Verilog-A these signal contributions may occur only inside an analog process as they are (piecewise) continuous-time signals.

5.1 Spin valve

The physics of the spin valve is the basis for most other magnetic sensors and devices at present. In the modeled spin valve system, only the most basic elements were added; uniaxial crystalline anisotropy, applied fields in $\hat{\mathbf{x}}$ and $\hat{\mathbf{y}}$, and the 2-D dynamic field term. The spin valve of Figure

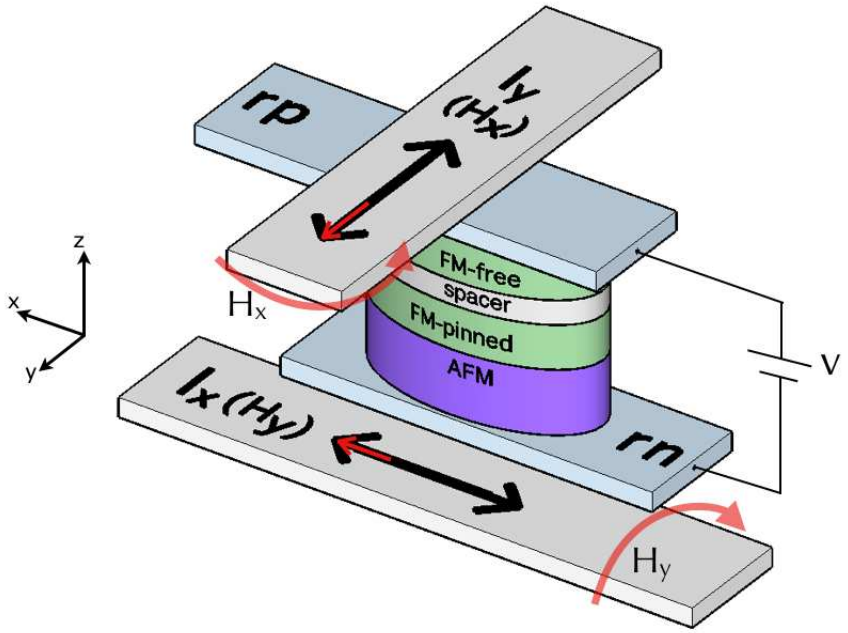

Figure 5.1: Spin valve system with test connections and current inputs.

1.1 is redrawn here so that the fields and electrical connections can be viewed.

5.1.1 Quasi-static behavior

For bistable operation, a uniaxial anisotropy is required to hold the magnetization of the free layer in one of two opposite directions along an easy axis. With the uniaxial anisotropy and zero applied field, the free layer magnetization, θ_{M1}, could be at either 0° or 180°, but the spacer thickness is such that the IEC sets the free layer AP to the pinned layer in zero field. Thus, the free layer has a magnetization of 180°. To verify the switching characteristics of this device a single switching field ($\mathrm{H_x}$ or $\mathrm{H_y}$) is calculated as $\mathrm{H_{x,y}} = \frac{2K_u}{\mu_0 M_S}$ according to Stoner and Wohlfarth [88, 14] with respect to a single-domain magnetic particle with uniaxial anisotropy. The resulting value is used as a minimum switching threshold (the coercive field, $\mathrm{H_c}$). When a single field must reverse the free layer magnetization ($+M_S$ to $-M_S$, and vice-versa) a value greater than this

minimum threshold is applied, and if both H_x and H_y are used for switching, each field is set to greater than half the minimum threshold. The first term in equation 5.1 is the applied field torque. This term combined with the uniaxial anisotropy term has equilibrium or switching field points (zero torque) at $\theta_M = 0°$ and 180°, when a field in only the $\pm\hat{\mathbf{x}}$ easy axis is used ($H_y = 0$). This easy axis, quasi-static switching characteristic is the classic square hysteresis curve from Stoner-Wohlfarth theory as shown in Figure 5.2 where the easy axis, M vs. H (M normalized to the saturation magnetization, M_S, and H to the coercive field, H_c) curve is highlighted in green. Other key quasi-static switching curves are also shown. The red dashed line shows the case where only H_y is applied (short or hard axis field), so that as θ_M rotates from 180° ($\frac{M}{M_S} = -1$) to 0° ($\frac{M}{M_S} = 1$), the magnetization changes linearly with the field, resulting in a diagonal curve without hysteresis. With both $H_x = H_y$ applied, the gold-highlighted curve shows the switching characteristic combining aspects of both the distinct coercive switching points of the easy axis field and the coherent rotational characteristic of the hard axis diagonal, with the equilibrium point always found for $\theta_M = 45°$.

5.1.2 The spin valve model

The effects of the Zeeman and anisotropy torques are now brought together with the dynamic component to complete the spin valve model. The dynamic term was combined with the Zeeman term in equation 4.23. The anisotropy has already been modeled as a torque in equation 4.9 and its function is to bring the magnetization back to the easy axis (positive or negative $\hat{\mathbf{x}}$-direction), where K_u is the strength of the uniaxial anisotropy. The balance of these three torques is

$$0 = \mu_0 V M_S \left(H_y cos\theta_M - H_x sin\theta_M\right) - K_u V sin2\theta_M - \frac{\mu_0 V M_S}{\gamma_0 \left(\alpha + \frac{1}{\alpha}\right)} \frac{d\theta_M}{dt} . \tag{5.1}$$

The first two terms describe the static behavior of a single domain particle as explained above and the final term is the dynamic or transient response. This physical model captures the two-dimensional hysteretic switching characteristics and dynamic magnetization response of the

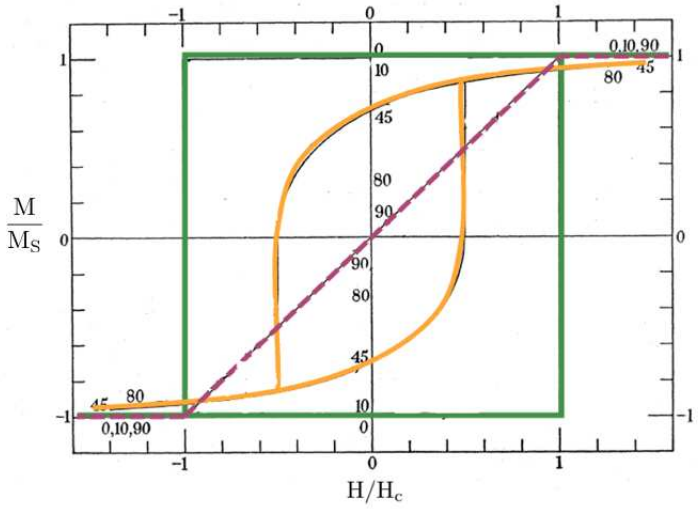

Figure 5.2: A Stoner-Wohlfarth hysteresis curve showing switching characteristics of a single domain magnetic particle; normalized magnetization against the applied field normalized to the coercive field, M/M_S vs. H/H_c. The green, square highlighted curve is for only $H = H_x$ applied ($H_y = 0$), the red dashed highlighted curve is for only $H = H_y$ applied ($H_x = 0$), and the gold highlighted curve is the case where $H = H_x + H_y$ and $H_x = H_y$.

single-domain, thin-film magnetic free layer with uniaxial anisotropy.

A block diagram for the model is presented in Figure 5.3. In this diagram the torques are balanced inside the *Free layer* block, which outputs the magnetization angle, θ_{M1}. The Verilog-A code for this is simply the sum of the three torques in equation 5.1 at node Tau(M), which will result in a value for $M = \theta_M$ when the sum equals zero.

Verilog-A analog process for 2-D torque balance:

```
analog begin
    // torque due to external field:
    Tau(M) <+ -'P_U0*Ms*(H(hx)*sin(Theta(M))-H(hy)*cos(Theta(M)));
    // anisotropy:
    Tau(M) <+ -Ku*sin(2*Theta(M)) ;
    // damping torque:
    Tau(M) <+ -ddt(Theta(M))* Ms/((alpha+1/alpha)*'P_gamma);

end
```

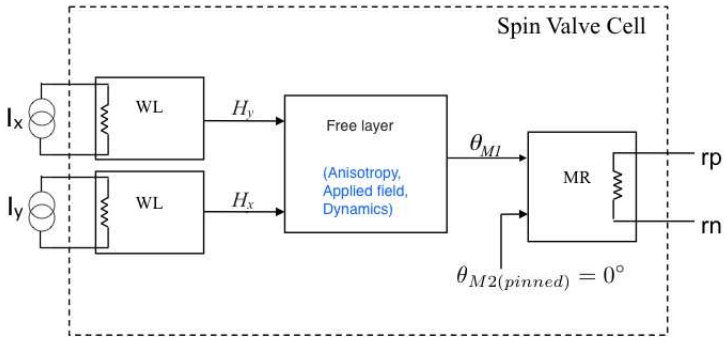

Figure 5.3: Block diagram of the spin valve and its modules.

The applied fields H_x and H_y are provided to the *Free layer* by currents on the electrical inputs of the bit and word lines, through a model block, *Write Line* (*WL*). This is a simple module which computes the magnetic field based on the current sheet approximation

$$H = \frac{J_s}{2} \tag{5.2}$$

where J_s is the sheet current density in the line. This assumes that the magnetic element is close to a wide, thin conductor. The *Write Line* has parameters W and R which are the width and resistance of the write line respectively. More sophisticated models could include the effects of thicker lines or magnetically cladded lines and spacing loss due to the separation between the write line and the magnetic element. In most cases, however, the write field will still be simply proportional to the current. Two write line modules are used in the spin valve cell, one for the word line (I_x) producing H_y, and the other for the bit line (I_y) producing H_x.

The *Magnetoresistance* (*MR*) module is shown as the output block in Figure 5.3. It models the magnetoresistance effect which determines the output resistance as a function of the magnetization angles of the two magnetic layers labeled θ_{M1} (the free layer magnetization) and θ_{M2} (the pinned layer magnetization). In the case of the spin valve, θ_{M2} is held fixed by connecting port M2 to a constant angle source. When the magnetization angle of the free layer is AP to that of the pinned layer, the magnetoresistance will be at its maximum, and at a minimum when

the layers are P, allowing a change in output voltage for a given current. The magnitude of the current is typically in milliamps and the voltage change is in millivolts. The change in the MR is modeled simply as $\Delta R \propto cos(\theta_{M1} - \theta_{M2})$. The parameters for the *MR* module are the maximum and minimum resistance values of the device. The module cores (analog processes) for the Write Line and Magnetoresistance are,

Verilog-A analog process for Write Line module:

```
analog begin

    V(inp,inn) <+ R * I(inp,inn);
    H(hout) <+ I(inp,inn) / (2*W);

end
```

analog process for Magnetoresistance module:

```
parameter real R_max = 1000 ; // high resistance [ohm]
parameter real R_min = 500 ; // low resistance [ohm]
analog begin

    V(rp,rn) <+ I(rp,rn)*(R_min+ 0.5*(R_max-R_min)* (1-cos(Theta(M1)-Theta(M2))))
    ;

end
```

5.2 Toggle MRAM

The Toggle MRAM model describes the magnetic behavior of two single-domain, magnetic free-layers coupled through exchange and magnetostatic interactions. The free layer (single domain) module from the spin valve is duplicated for both free layer blocks with the same uniaxial crystalline anisotropy, applied fields, and 2-D spin-dynamic effects obtained in equation 5.1. A physical model of the Toggle MRAM cell in Figure 5.4(a) illustrates the layers and the signal interface for its input and output signals. Figure 5.4(b) gives a block diagram showing the module

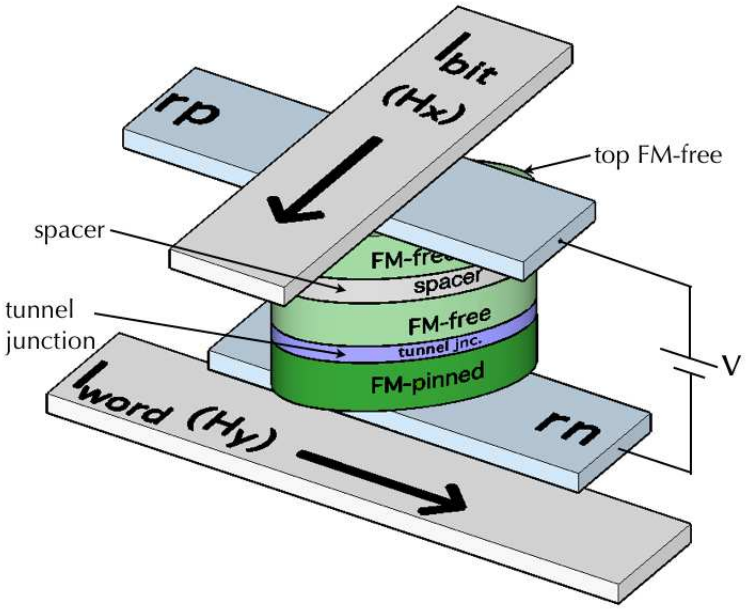

(a) Single Toggle MRAM bit sandwiched between bit and word line conductors. The structure has two FM free layers separated by a NM spacer, with a tunnel barrier between the bottom free layer and the pinned layer.

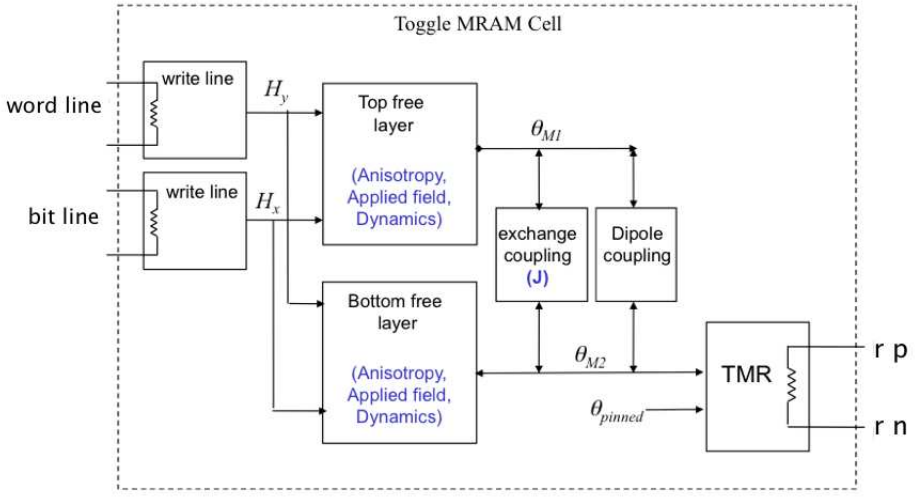

(b)

Figure 5.4: A Toggle MRAM bit. a) physical structure and b) model block diagram showing two free FM layers interacting via exchange and dipole coupling blocks. The output magnetoresistance is implemented with a magnetic tunnel junction between the bottom free layer and the pinned layer.

connections, where the external interface to the model is like that for the spin valve, with a bit line and a word line to input electrical current, which is then converted to magnetic fields in the $\hat{\mathbf{x}}$ and $\hat{\mathbf{y}}$ directions via two writeline modules. The output is again in the form of a magnetoresistance based on the orientation of the free and pinned layers, however, the bottom free layer is separated from the pinned layer by a thin, insulating tunnel barrier. Electron tunneling through this barrier or magnetic tunnel junction (MTJ) depends on the angle between the magnetization of the bottom free layer and the pinned layer, resulting in a tunneling magnetoresistance (TMR). The read circuitry of an MRAM determines the binary state of the bit by measuring this tunnel junction resistance through the adjoining contacts. When the bottom free layer and pinned layer are magnetized in the same direction, the resistance is lower (binary ‘‘0”) and when the bottom free layer and pinned layers are magnetized in opposite directions the resistance is higher (binary ‘‘1”).

5.2.1 Dynamic operation and response

Two useful properties of the Toggle MRAM cell are that there are two free layers, and that the entire layer stack is angled at 45° to the x and y axes. These two attributes work together to lower the energy needed to cause the free layers to “spin-flop” (i.e. the layers discontinuously jump from an AP state $(0,\pi)$ to a scissored state $(\theta,-\theta)$ state, with their net moment in the direction of the applied field). Examples of spin-flop states are phases (1), (2) and (3) in Figure 5.5. When the bit is the intended target cell in an MRAM bit array, it experiences a full-select field (both H_x and H_y) as part of a pulse sequence (phase (2) in the figure). When a half-select field is experienced (only H_x or H_y) the field is not along the 45° easy axis of the bit and the activation energy increases, which significantly reduces erroneous half-select switching errors. The spin-flop phase and its near-zero activation energy allows the two free layers to rotate through a set of field pulses to finally toggle their moments (switch magnetization direction) and is the key to this architecture [35].

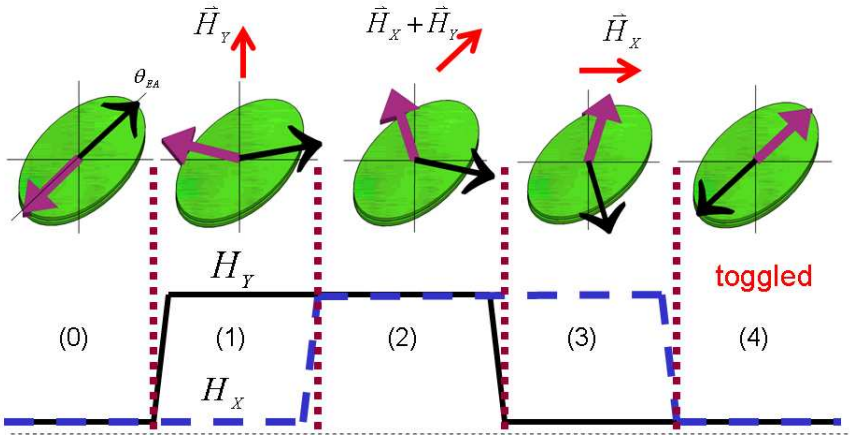

Figure 5.5: Toggling of the free layer magnetizations using a "box field" sequence.

Figure 5.5 is used to explain a toggle sequence graphically. The magnetic state of the free layers in the bit to be written (target bit), is reversed by applying a sequence of magnetic field pulses through the word and bit lines as in [36]. Although a variety of different field sequences can result in the toggling of the bit, the most common is the "box field" sequence illustrated in the figure. First a current is put through the word line; then the bit line is also activated. The word line is then turned off before the bit line. When plotted in the $H_x - H_y$ plane, the resulting field sequence follows the outline of a square box [76, 89]. Application of a magnetic field from a word line or bit line by itself (half-select) does not affect the state of the target bit. However, the H_x and H_y fields can affect MTJ bits which are neighbors to the target bit in the MRAM cell array depending on the spacing of the cells [33]. The response of the two free layer magnetizations is illustrated in the bit drawings which follow the time sequence in Figure 5.5. At the beginning of the sequence (0), there is no applied magnetic field and the two layers are oriented along the 45° anisotropy direction and opposite to each other with the bottom free layer's moment at 225° (solid wide arrow) and the top free layer's moment (thin arrow) at 45°. With application of the H_y field (1), the magnetization directions "spin flop" to orient themselves perpendicular to the applied field. When H_x is then added (2) the magnetic moments remain in the spin flop state but rotate around so that their net moment is along the direction of the total

applied field. In step (3) only H_x remains and the magnetic moments continue to rotate together in the same direction. Finally, all fields are removed (4) and the magnetic moments relax back to the anisotropy axis but with their directions reversed from the original state, with the top free layer's moment now at 225°, and the bottom free layer's moment at 45°. The box field sequence reliably toggles the state of the MRAM bit regardless of the initial state. Prior to writing, the state of the bit must be read to determine whether it needs to be toggled or not.

5.2.2 Model differences from the spin valve: TMR, dipole and exchange coupling

Three important effects are added to the model of the Toggle MRAM bit cell over the original spin valve/MRAM cell; the bias voltage dependence of the output TMR covered in section 2.5.2, and the coupling field, composed of the dipole and spacer exchange coupling. For the former, the full expression for the MTJ resistance which depends on the relative orientation of the magnetic moments of the bottom free layer θ_{M2} , with respect to the orientation of the pinned layer $\theta_{Mpinned}$, is

$$R_{MTJ} = \frac{R_{min}}{2} \cdot (1 + TMR(\mathrm{v}))\,(1 - cos(\theta_{M2} - \theta_{pinned}))\ . \tag{5.3}$$

R_{min} is the low value of the magnetoresistance and the tunneling magnetoresistance (TMR) has the bias-voltage dependence in equation 2.7 . In simulation, a V_h value for MgO tunnel barriers was used obtained from [31]. The Verilog-A code for for the TMR is

Verilog-A analog process for TMR module:

```
parameter real Vh = 0.4; //Bias effect parameter [volts]
parameter real M_ea; //Pinned angle = easy axis angle
real BE; //bias effect value based on Vh
analog begin

    BE = 1 + pow((V(rp,rn)/Vh), 2);
    I(rp,rn) <+ V(rp,rn) / (0.5 * R_min * (1 + (TMR/BE) * (1 - cos(Theta(M1)
    - M_ea))));
```

end

In this code, $\left(\frac{\mathsf{TMR}}{\mathsf{BE}}\right)$ is equal to the expression for $TMR(\mathrm{v})$ in equation 2.7. This code module also sets the pinned, easy axis angle internally to 45° degrees using the parameter M_ea. Because the bias voltage, V(rp, rn), is the controlled value, the current through the tunnel junction, I(rp, rn), is the variable for which the simulation is solved.

The other differences between the toggle MRAM bit cell model and the spin valve model is the additional use of the exchange coupling and dipole coupling torques. These two blocks are shown in Figure 5.4(b) coupling together the two free layers by the effective fields acting between the layers. As noted earlier in Chapter 1, the free layers are coupled antiferromagnetically (due to IEC) by the spacer thickness. To account for the 45° easy axis in free layers, the dipole coupling torque equations 4.15 and 4.16 must subtract the designated easy axis angle (θ_{EA}) from the magnetization angle:

$$\mathbf{T_{dip12}} = J_{12} \cdot N_{y1} sin\left(\theta_{M1} - \theta_{EA}\right) cos\left(\theta_{M2} - \theta_{EA}\right) - N_{x1} cos\left(\theta_{M1} - \theta_{EA}\right) sin\left(\theta_{M2} - \theta_{EA}\right) ,$$

$$\mathbf{T_{dip21}} = J_{21} \cdot N_{y2} sin\left(\theta_{M2} - \theta_{EA}\right) cos\left(\theta_{M1} - \theta_{EA}\right) - N_{x2} cos\left(\theta_{M2} - \theta_{EA}\right) sin\left(\theta_{M1} - \theta_{EA}\right) .$$

In the case of the exchange coupling torque, the exchange interaction depends only on the difference between the layers' magnetization angles (*ie.,* not with respect to the easy axis), so the torques applied in the exchange coupling block become (from equation 4.11)

$$\begin{aligned} \mathbf{T}_{\mathrm{exch12}} &= -\mathrm{A}_1 \mathrm{J} sin\left(\theta_{M1} - \theta_{M2}\right) \\ \mathbf{T}_{\mathrm{exch21}} &= -\mathrm{A}_2 \mathrm{J} sin\left(\theta_{M2} - \theta_{M1}\right) , \end{aligned}$$

and it is reasonably assumed that the free layers' areas are the same ($\mathrm{A}_1 = \mathrm{A}_2$).

The Verilog-A code for the dipole and exchange torques are entered just as the above equations.

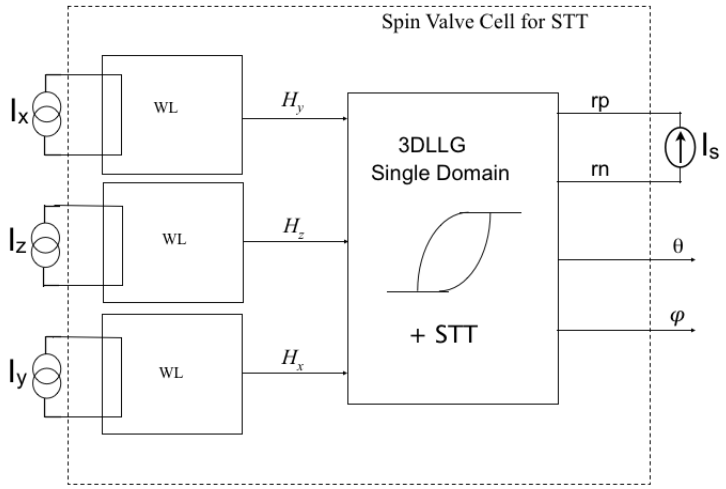

Figure 5.6: Block diagram of an spin valve system using STT. $I_{spin}$is the injected CPP current.

5.3 Spin transfer torque spin valve

The STT device introduced with Figure 1.3 is basically a GMR spin valve (NM spacer) with CPP current injected through the layers. This primary mode of STT has been developed in section 4.7. Here we cover the set-up and operation of the STT spin valve in its free layer switching mode and also its mode of steady state precession. The STT device model was developed only in 3-D.

5.3.1 STT-driven magnetic reversal of spin valve free layer

For the switching of the FM free layer in a spin valve via STT we use the block diagram shown in Figure 5.6. It is a block diagram of a GMR spin valve with a single domain free layer. The 3-D model is labeled "3DLLG Single Domain+STT" and the specific field terms from section 4.8 can vary. The figure shows a CPP current (labeled I_s) injected through the multilayer via the rp and rn terminals to generate the electron or spin current which will transfer spin angular momentum at the NM/FM interfaces. The current sources, I_x and I_z are unnecessary for this

operational mode. In practice, a field along the easy axis direction generated with I_y is sometimes used to guarantee a fixed magnetization in the polarizing/fixed layer. As an initialization step, I_y is pulsed negative (positive) to ensure that in simulation, the free layer begins AP (P) to the polarizing layer.

After the the free layer magnetization direction is initialized, I_s is ramped or pulsed as a positive current (negative current) in order to switch the magnetization of the free layer P (AP) to the polarizing layer. The spin torque from the current, I_s , moves **m** away from its initial equilibrium. With enough current, the precession angle due to the spin torque can grow overcoming the damping torque, and switch the magnetization when the polar angle, θ, increases past 90°. A minimum current magnitude for switching is determined with the current ramp.

5.3.2 Steady-state precession using STT

The ability to manipulate the thin-film free layer magnetization in a device using the transfer of spin angular momentum has spurred much investigation into what other kinds of magnetic motion might be generated with this torque. Another discovered form of magnetic excitation using STT is steady-state precession. Without any mechanical motion, a spin-valve multilayer is able to convert energy from the perpendicular DC spin current into high-frequency magnetic rotations that could be used as microwave sources or nanoscale oscillators.

Several sources have documented phase diagrams of spin transfer dynamics as a function of spin current and magnetic field [17, 44, 90, 16]. These authors and several more have investigated the different phases of spin transfer dynamics, and the phase diagrams are consistent with one another. These diagrams indicate the conditions under which steady-state precession is able to occur.

To reach the conditions of steady-state precession, a field in the initial direction of the free layer magnetization must be present. The spin torque from the current, I_s, moves **m** away from its equilibrium (P or AP to the polarizing/fixed layer), but if the damping torque increases with

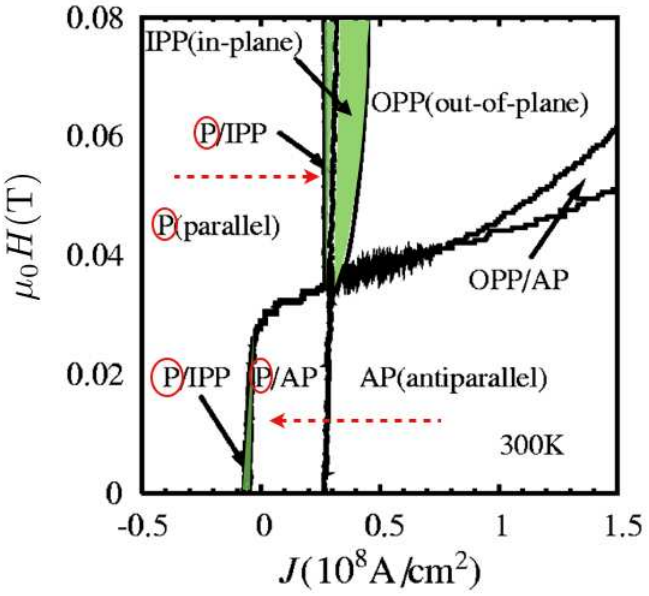

Figure 5.7: Phase diagram of spin transfer dynamics - for a fixed field H, a bistable region labeled A/B exhibits the A state when I is scanned from left to right, and the B state when I is scanned from right to left. Reference [17] has $10^{8\ \mathrm{A}/\mathrm{cm}^2} \leftrightarrow 10\,\mathrm{mA}$. Green and red highlights have been added for clarity. [Reprinted figure with permission from J. Xiao, A. Zangwill, M. D. Stiles, Phys. Rev. B. Vol. 72, 014446 (2005). Copyright (2005) by the American Physical Society.]

the precession angle faster than the spin torque, the precession angle may become limited (by the damping). In this case, **m** can achieve a state of dynamical equilibrium and precess continuously at some fixed average angle in response to the DC spin current. The energy gained from the spin torque during each cycle is balanced by the energy lost to damping.

In Figure 5.7 some of Xiao's data at T=300K is exhibited. If the region is labeled A/B then it exhibits the A state when $I = I_s$ is scanned from left to right, and the B state when $I = I_s$ is scanned from right to left. It is seen for this particular nanopillar geometry that at fields of $0 \leq |H_{ea}| \leq 32\,{}^{kA}/_{m}$ ($0 \leq \mu_0 \mathbf{H} \leq 0.04\,T$), applied along the easy axis in the direction of the initial AP magnetization, a current is reached (going lower right to lower left, AP $\rightarrow$ IPP) where an in-plane precession (IPP) occurs. This IPP region is a small triangular sliver highlighted in green. In order to switch from a P state to an equilibrium IPP state (upper green region, going upper left to upper center, P $\rightarrow$ IPP $\rightarrow$ OPP), a larger magnitude field must be applied, and a larger magnitude spin current as well. In the case of beginning in an AP state, it is somewhat easier to find the spin current region for IPP, but if I_s is too great, **m** will simply switch to the P state. In all cases, the applied field, H_{ea} must be larger than the coercive field $H_c = H_k + H_d$ to achieve steady-state precession.

Chapter 6 – Simulating in Spectre/Spice

Spectre is specifically named in this work because it is Cadence's own derived SPICE-like analog simulator, which has benefits of accuracy in several areas and the inclusion of Verilog-A. The SPICE and Spectre simulators do work similarly, but several algorithms, such as local truncation error and convergence checking are different.

The simulation of the device models in Figures 5.3, 5.4 and 4.5 are performed using the Cadence Virtuoso IC design platform with its Spectre Circuit simulator in its Analog Design Environment. The analog high-level description language (AHDL) in which the models are written, Verilog-A, is part of the Spectre Verilog-A Simulation option, and is an open standard. The Spectre circuit simulator uses direct methods such as implicit integration and Newton-Raphson, to simulate analog circuit modules at the differential equation level. The behavior of each module is described mathematically in terms of its terminals and external parameters applied to the module.

The magnetic device models here have been based on fundamental physics and are intended to be accurate, but not so detailed that they would be a bottleneck in a system simulation with other circuits. The goal has been to achieve correct critical behaviors, such as magnetic moment switching, control of that switching with material and device parameters, and correct system time constants.

Verilog-A and Spectre simulation mechanics

6.0.3 Verilog-A and magnetics

Working with the multi-disciplinary models in Verilog-A is similar to working with an electrical circuit in that Kirchoff's potential and flow laws (KPL and KFL) are still used. The potentials around a loop of branches sum to zero and all the branch flow quantities must sum to zero at a node. A Verilog-A system is just a lumped network of nodes and branches where the potentials across the branches and the flow quantities through the branches are allowed to be any physical quantity, not only voltage and current. When potential and flow quantities are used together, their product within the system is conserved, and these quantities make up a conservative **discipline**. The potential and flow quantities are physical quantities and each is called a **nature**. A conservative system must have two natures, one that is a potential quantity and one that is a flow quantity. If a **discipline** uses only one **nature**, it is not a conservative **discipline** [91].

In the magnetic device models, two of the disciplines used are 1) electrical - with Voltage and Current as potential and flow quantities, and 2) rotational - with Angle and Angular_Force (Torque) as its potential and flow quantities. Both of these are conservative disciplines; the first conserves power and the latter, energy. It was necessary to define a third, new **discipline** for magnetic fields. There is only one **nature** assigned to this **discipline** which requires that it have a potential **nature**. The statements are

nature Magnetic_Induction
abstol = 1e-6 ;

access = H ;
units = "A/m" ;

endnature

discipline sig_flow_H

potential Magnetic_Induction ;

enddiscipline

For the quantities of torque and magnetization angle the natures and disciplines are

nature Angle

abstol = 1e-6 ;
access = Theta ;
units = "rads" ;

endnature

and

nature Anglular_Force

abstol = 1e-6 ;
access = Tau ;
units = "N*m" ;

endnature

discipline rotational

potential Angle ;
flow Angular_Force ;

enddiscipline

It is obvious that the **nature** defines the attributes of the physical quantity and the **discipline** defines a signal as a potential (and/or flow if there are two natures). In fact, the input/output ports of the block are defined by the discipline assigned to the port signal. The core 2-D single domain block is a good example of how the natures work as the lumped element model depicted in Figure 6.1. There are three torques in this core block; applied field $\mathbf{T_a}$, uniaxial crystalline anisotropy $\mathbf{T_k}$, and the 2-D dynamic or damping torque $\mathbf{T_{dyn}}$. These torques with the output torque flow must sum to zero at every simulation time step (the Spectre circuit simulator directly checks Kirchhoff's Current/Flow Law at each time step), resulting in a value for the magnetization angle, θ_M, which is a potential across its branch.

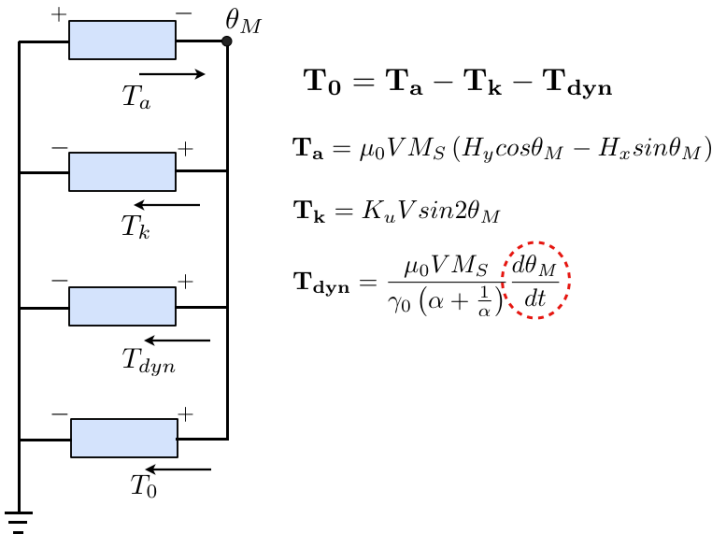

Figure 6.1: Torques or Angular_Force as flow natures, summing at the torque balance node (θ_M) in the 2-D single domain block. θ_M is the block output and resultant moment angle which is a potential of the same discipline as the torques (rotational).

6.0.4 Spectre/SPICE simulation

The correct simulation mode for the magnetic device models is transient analysis, as the output of interest is the change in the angle of magnetization with time. Transient analysis generates a system of non-linear differential equations which are discretized in time to convert the problem into a sequence of systems of non-linear algebraic equations making the time derivative into a finite difference approximation [class notes, ECE 521 - Analog Circuit Simulation]. A transient simulation does not require a DC operating point to be calculated, but it does require an initial state that allows the simulation to converge. The DC operating point is important only if it is desired to run an AC small-signal analysis because the small-signal analysis begins by linearizing the circuit about an operating-point. An AC analysis would be used with these models if investigating, for example, susceptibility, which requires the addition of a small-signal current(s) (which convert to an AC magnetic field) on the input to the model. In this case, the simulation does not record the system output in time, but keeps the system nodes at their

operating point values and computes a Taylor series expansion [92] of the change in system response to the small, sinusoidal change in the stimulus ($\frac{\Delta \mathbf{M}}{\Delta \mathbf{H}}$), using complex (phasor) notation for the stimulus and output variables. In most cases (2-D and 3-D LLG models) a DC operating point could be found, but it was common in the 3-D LLG model with the additional STT term, for the simulator to fail to find an operating point solution. It is likely that with the proper initial state and simulator settings that the operating point could be found if needed.

6.0.4.1 Transient Analysis

It is helpful to view what happens during a transient analysis. Going back to Figure 6.1, KPL/KFL gives the torque equation

$$
\begin{aligned}
\mathbf{T_0} &= -\mathbf{T_a} - \mathbf{T_k} - \mathbf{T_{dyn}} \\
\mathbf{T_0} &= \mu_0 V M_S \left(\mathrm{H_y} cos\theta_M - \mathrm{H_x} sin\theta_M\right) - K_u V sin2\theta_M - \frac{\mu_0 V M_S}{\gamma_0 \left(\alpha + \frac{1}{\alpha}\right)} \frac{d\theta_M}{dt} \\
\mathbf{T_0} &= \mu_0 V M_S \left[\mathrm{H_y}\left(1 - \frac{\theta_\mathrm{M}^2}{2!} + \frac{\theta_\mathrm{M}^4}{4!} - \ldots\right) - \mathrm{H_x}\left(\theta_\mathrm{M} - \frac{\theta_\mathrm{M}^3}{3!} + \frac{\theta_\mathrm{M}^5}{5!} - \ldots\right)\right] - \cdots
\end{aligned}
$$

and the simulator, for example, will expand the $\mathbf{T_a}$ equation's $sin\theta_M$ and $cos\theta_M$ terms in their respective series. It is clear that all but the dynamics expression can be formulated as a series expansion or the product of series expansions, and the simulator must deal with a derivative in the dynamic torque (circled in the figure). There are several possibilities for the derivatives' discrete approximation, but the two methods regularly employed in the model simulations were:

1. Backward Euler $\qquad \frac{d}{dt}(\theta_M(t_{k+1})) \approx \frac{1}{h}\left[\theta_M(t_{k+1}) - \theta_M(t_k)\right]$

2. Trapezoidal rule $\qquad \frac{d}{dt}(\theta_M(t_{k+1})) \approx \frac{2}{h}\left[\theta_M(t_{k+1}) - \theta_M(t_k)\right] - \frac{d}{dt}(\theta_M(t_k))$

where $h = t_{k+1} - t_k$, and in the Trapezoidal rule, $\frac{d}{dt}(\theta_M(t_k))$ is the previously-solved derivative. The rules for choosing the time step are two-fold;

1. the size of the simulation time step (h) must be much smaller than the time constant of

the dynamic response, and

2. very small time steps will allow the computed solution to be more accurate (closer to the real solution), *if* the system is convergent (i.e., moving towards the actual solution).

The above example requires an initial value for θ_M and iterates a set of non-linear algebraic equations using a finite difference approximation for the time derivative, illustrating the concept of numerical integration - solving finite difference equations one point at a time starting from an initial condition.

6.0.4.2 The system solving algorithm: Newton-Raphson

The set of equations at every step of a transient analysis are non-linear algebraic systems and can not be solved directly. The simulator uses the Newton-Raphson method, which takes an initial guess of the solution of the system of non-linear equations, and refines it, making it more and more accurate on each iteration. In the above section, the expression for $\mathbf{T_0}$ has had all its components approximated and discretised in time, but the overall system simulation is looking for the solution, θ_M, where $f(\theta_M) = \mathbf{T_0} = 0$. As an example of a simple scalar system using $f(v^k)$ with solution, $\hat{\mathbf{v}}$, the system solution is found using the Newton-Raphson iteration equation,

$$\frac{\partial f(v^k)}{\partial v}\left(v^{k+1} - v^k\right) = -f(v^k) \tag{6.1}$$

which is presented graphically in Figure 6.2 [92].

With an initital value $v^{(0)}$, the simulator computes $f(v^{(0)})$ and linearizes the function about $v^{(0)}$ by taking the derivative of $f(v^{(0)})$ with respect to v (left graph). This generates the first iteration value, $v^{(1)}$ about which the function is linearized a second time (right graph). The process continues until two convergence criteria are met (in Spectre):

1. The difference between the last two iterations must be small, $\left|v_n^k - v_n^{k-1}\right| < \texttt{reltol}\cdot v_{n\max} + \texttt{abstol}$, where $v_{n\max} = \max\left(\left|v_n^k\right|, \left|v_n^{k-1}\right|\right)$, $\texttt{reltol} = 10^{-3}$, and $\texttt{abstol} = 10^{-6}$ (defaults)

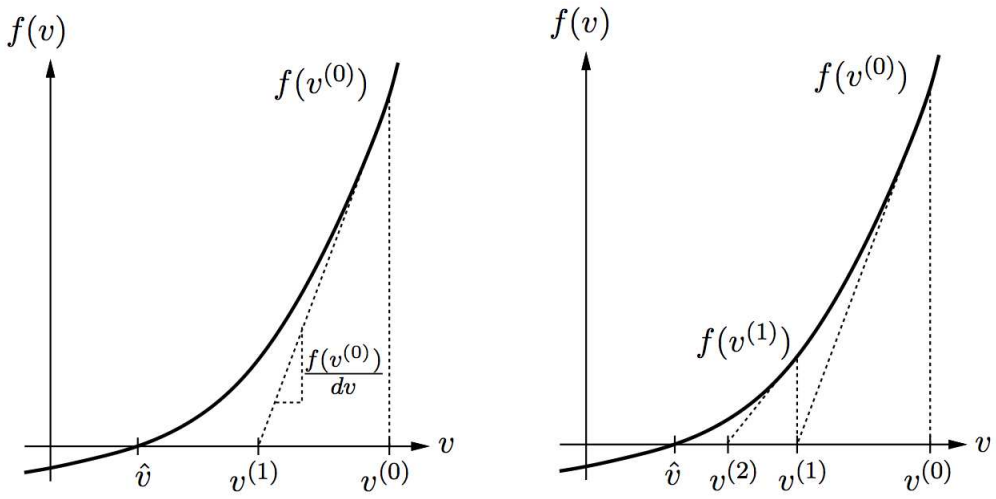

Figure 6.2: A graphical representation of Newton's method.

.

2. If $f_{n\max}$ is the absolute value of the largest Flow entering node n from any one branch, then the residue (or error) is converged if $\left|f_n(v^k)\right| < \texttt{reltol} \cdot f_{n\max} + \texttt{iabstol}$, where $\texttt{iabstol} = 10^{-12}$.

Criterion 1 assures that the iteration values have successively moved closer together in the same direction, and if the value at a node is close to zero, the simulator allows an update smaller than `vabstol` to be accepted. The second criterion requires that the value of the function at node n be very close to zero when converged, with `iabstol` present to allow the simulator to accept a value less than `iabstol` . As long as the initial solution guess or initial conditions are a good choice, and the model equations are continuously differentiable, convergence can occur.

Simulation choices

In the magnetic model simulations the Backward Euler integration method is used automatically by the simulator on the first time step and at changes in the input waveform (breakpoints). Backward Euler is ideal for a linear signal response, which for a slow startup response, is quite

reasonable. Also, both Backward Euler and Trapezoidal methods are "one-step," i.e., they compute the value of the current time point using the value of the one immediate predecessor, which means they are able to adapt quickly to abrupt signal changes. The Trapezoidal rule is ideal if the solution is quadratic, which is more like the expected magnetodynamic behavior. The Trapezoidal method was most often used in simulation because it is known to definitively report the stability of a system, to react fast to signal changes, and it does not exhibit artificial numerical damping. The latter is important to simulating to a more accurate magnetic moment switching time. The drawback to the Trapezoidal integration method is that it is very sensitive to errors made on previous timesteps, and so should not be used unless the relative step-to-step error tolerance (`reltol`) is set conservatively - this was always done, but this sometimes made it more difficult to converge.

Chapter 7 – Simulation results and discussion

7.1 2-D Spin valve

The 2-D Spin valve uses the free-layer single domain module in the system shown in Figure 7.1 (introduced in section 5.1). The single domain module uses the torque balance expression in equation 5.1. The simulations follow the movement of the free-layer moment, θ_{M1}, via the GMR-based output voltage across the electrical output ports, rp and rn. The GMR should behave as shown in Figure 1.1 and output a low resistance when the free and pinned layers are parallel in magnetization, and a high resistance when the layers are antiparallel. To sense the GMR voltage, the test circuit used a 1 A current source into the MR block and the voltage read across the output ports, V(rp,rn), allowed the calculation of the MR value in ohms. The output resistance is arbitrarily fixed in the range $500\Omega \leq R \leq 1000\Omega$ by setting $R_{min} = 500\Omega$ and $R_{max} = 1000\Omega$ in the Magnetoresistance (mr Listing 2 in Appendix 8.2) module's equation for the resistance across the junction,

$$R = R_{min} + \frac{1}{2}\left(R_{max} - R_{min}\right)\left(1 - cos\left(\theta_{M1} - \theta_{M2}\right)\right) .$$

The parameters used for the transient switching and hysteresis simulations that follow are given in Table 7.1 .

7.1.1 Transient simulations of the spin valve used as an MRAM cell

The block diagram and physical depiction of the spin valve cell in Figure 7.1 is representative of a single element (one free layer) MRAM cell. In a transient simulation a sequence of four current pulses was applied to the bit and word lines as shown in the plot of the results in Figure

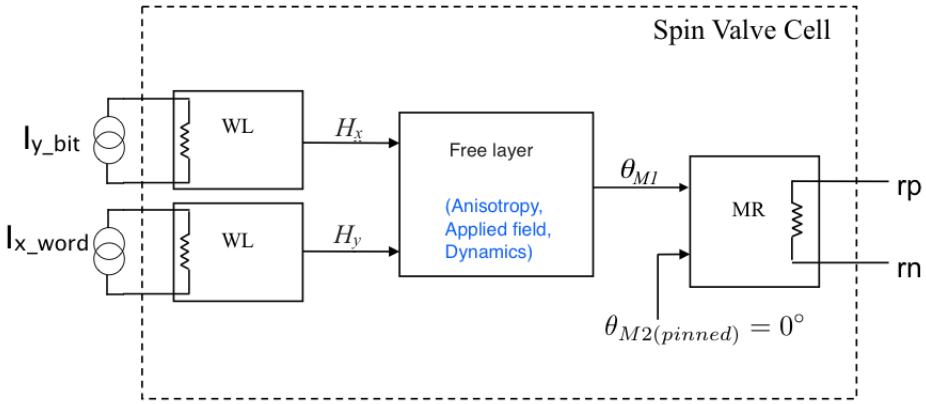

Figure 7.1: a) 2-D spin valve block diagram and b) physical multilayer representation of block diagram in (a).

2D spin valve	
Effective field terms included in simulation	*Parameter and field values*
uniaxial crystalline anisotropy (H_k)	$K_u = 300\ (J/m^3)$ $H_k \approx 300\ (\frac{A}{m})$
shape anisotropy (H_d)	$H_d = 0$
external applied field(s) (H_a) via $I_{x_{word}}$ and $I_{y_{bit}}$	Transient: $-1.2\ (\frac{kA}{m})$ and $0.5\ (\frac{kA}{m})$ Hysteresis: $-1.5\ (\frac{kA}{m})$ to $1.5\ (\frac{kA}{m})$ and back
interlayer exchange coupling (H_{ex})	N/A
dipole coupling (H_{dip})	N/A
spin transfer torque (H_{stt})	N/A
Other parameters	
Gilbert damping factor (α)	0.02
Easy axis direction	$\hat{\mathbf{x}}$ axis, EA=(1, 0, 0)

Table 7.1: Fields and parameter values used for the 2D spin valve transient and hysteresis simulations.

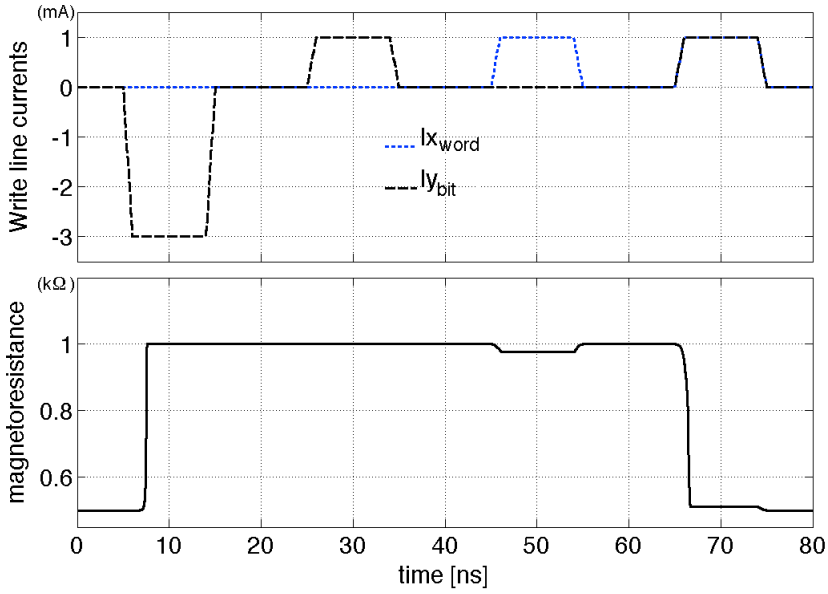

Figure 7.2: Spin valve simulated as an MRAM cell with word- and bit- line pulses.

7.2. The lower plot shows the resulting change in resistance of the spin valve. The sequence of pulses is as follows: first, a large negative current pulse exceeding the switching threshold is applied to the bit line ($-H_x$) to switch the free layer from the initial low resistance state at 0° to the high resistance state at 180°. The second pulse is a smaller positive current on the bit line ($+H_x$) which does not result in any resistance change because it does not exceed the switching threshold along the easy axis. The third pulse is a current pulse on the word line (H_y), also below the switching threshold. This pulse results in a small, temporary rotation of the magnetization (because the field was applied along the hard axis) and a small change in resistance for the duration of the pulse. Finally, a coincident pulse is applied on both the word and bit lines, resulting in a 45° field exceeding the switching threshold. The spin valve is switched backed to the original low resistance state by this pulse. This sequence illustrates situations that would occur in the addressing of a MRAM array. The second and third pulses are ones that would be seen by un-addressed bits on the same word or bit line as an addressed bit. The final pulse is that which would be experienced by the addressed bit. In addition to correctly modeling the switching,

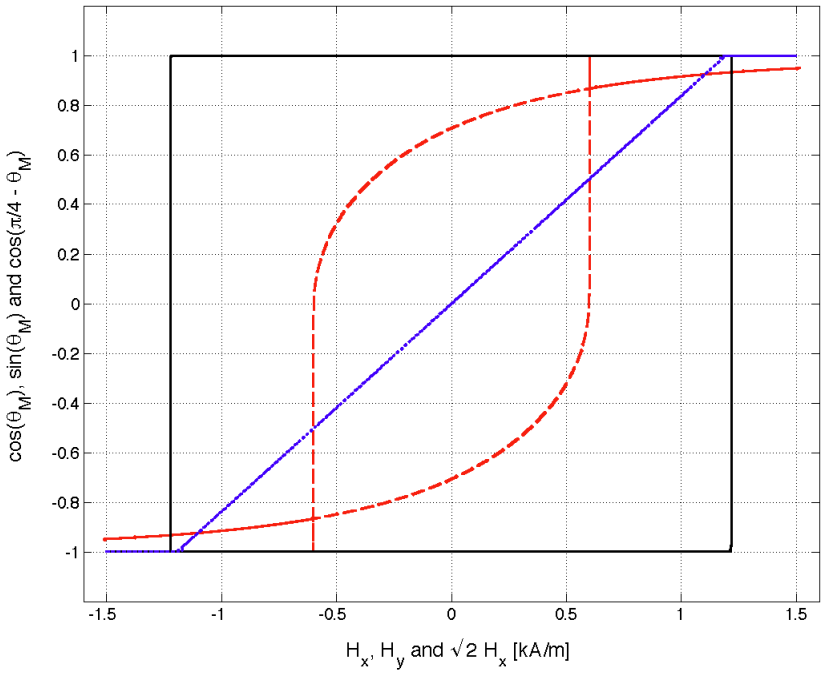

Figure 7.3: Hysteresis curves for field applied along the easy axis (square loop), hard axis (diagonal - no hysteresis) and at a 45° to both axes (rounded loop).

the resistance variations of the un-addressed bits are accurately represented. The model also captures time delays associated with the damped response of the magnetization, particularly in situations where large angle rotations are called for. Particularly notable is the long delay from the beginning of the first negative field pulse to when the magnetization finally reverses itself. The field from the bit line in this case is exactly opposite of the original magnetization direction, resulting in an unstable equilibrium which persists for almost one nanosecond. In fact, a small 1 μA current was required in the word line to get the spin valve model to switch at all.

7.1.2 Hysteresis loops

The single domain module was also tested for its hysteretic behavior. The model response for fields in the x direction, y direction and at 45° is shown in Figure 7.3. In each case, the field is

swept positive and then negative. As is traditional, only the component of magnetization in the applied field direction is plotted. The resulting hysteretic curves are identical to those calculated by Stoner and Wohlfarth in their 1948 work [88] on single-domain particles. The x-axis (easy axis) curve displays the expected square hysteresis loop while the y-axis (hard axis) response is hysteresis free. The 45° loop displays some hysteresis but with considerably lower switching field than the x-axis response. The spikes in the 45° degree loop are transients resulting from the time-stepped solution in Verilog.

7.2 2-D Toggle MRAM

The Toggle MRAM model is more complex in its behavior than the spin valve-based MRAM cell, and uses all the torque equations derived in Chapter 4, sections 4.2-4.3, and also the voltage bias-dependent TMR effect in section 2.5.2. The Spectre schematic connects the model blocks together as in Figure 5.4(b) for simulation.

The model was evaluated with stimuli that demonstrate the behavior of the coupled free layers in response to a 45° field and simulate the toggle MRAM writing sequence. Parameter values used in the simulations are those from Worledge's work, listed in Table 7.2 [35, 36, 93]. These parameters provide the conditions for spin flop and toggle switching and represent a realistic design point. Except in the case of the combined spintronic-CMOS read/write circuit simulation presented in Figure 7.7, the V_h parameter was set to the first, large value in Table 7.2 (1×10^6V) thus disabling the TMR bias voltage effect. The demagnetizing factors are determined by the shape of the bit and can be approximated by $N_x = \frac{2t}{\pi a}$ and $N_y = \frac{2t}{\pi b}$, where t is the layer thickness, and a and b are the length and width of the bit (a thin, rectangular layer). These approximate factors were used in the simulation of the toggle MRAM model and in some of the simulations that follow for the 3-D model. Otherwise the demagnetization factors used are published values for N_x , N_y and N_z from McMichael [83].

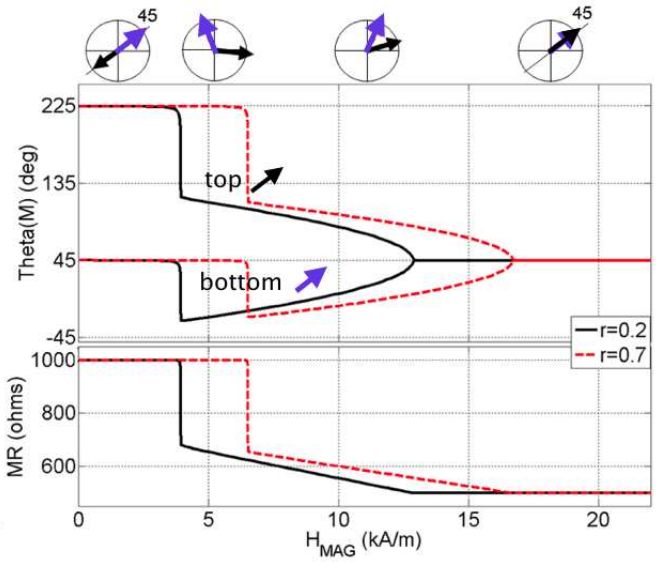

Figure 7.4: Response of free layer moments (bottom and top free layers) in the toggle MRAM model in response to a 45° field ($H_x = H_y$). The spin flop transition and saturation fields are smaller for the r=0.2 attenuation case and larger for the r=0.7 case.

7.2.1 Static response

The static response of the coupled free layers to a 45° applied field (i.e. $H_x = H_y$) is shown in Fig. 7.4. The equilibrium angles of both bottom and top free layers are plotted as a function of the magnetic field as this is increased from 0 to 20 $^{kA}/_{m}$. Orientation of the free layer moments is shown schematically in the circles above the plots at key transition points. At low fields, the anisotropy keeps the moments along the 45° easy axis. As the field is increased, there is a transition to the spin flop state at a critical field which depends on the strength of coupling between the free layers. At this point, the anisotropy is overcome and the magnetic moments turn perpendicular to the applied field. As the field is increased further, the magnetic moments gradually scissor towards the applied field until they are aligned parallel to the field at the saturation point. The changing angle of the bottom free layer is reflected in a corresponding change in magnetoresistance. The two curves are for two different dipole coupling attenuation factors, r. Higher values of r (thinner spacer layer) result in stronger anti-parallel coupling

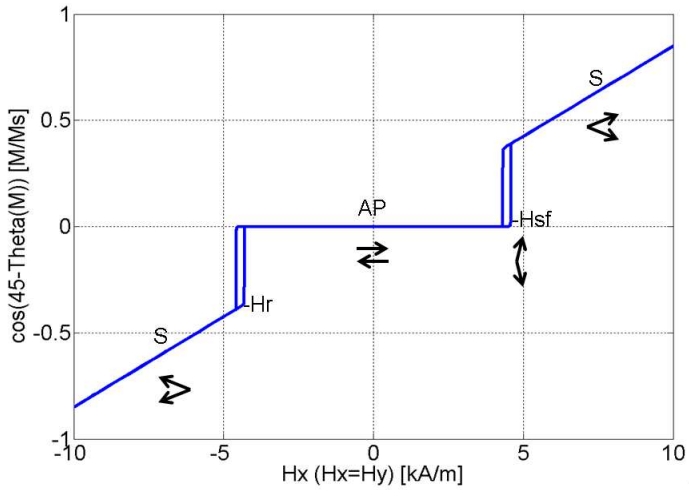

Figure 7.5: Hysteresis curve for the MRAM bit model stimulated by increasing and decreasing 45° field ($H_x = H_y$). P designates parallel moments in each layer, AP – anti-parallel, S – scissoring, → Hsf – going into spinflop field, → Hr – returning to AP state.

between the layers pushing the spin flop and saturation transitions to higher fields. A full hysteresis loop is shown in Figure 7.5 for a 45° applied field first increasing and then decreasing. The transitions to and from the spin flop transition occur at different fields depending on whether the applied field is increasing or decreasing. This hysteretic behavior is consistent with that predicted by Worledge [35, 36].

7.2.2 Dynamic response

The response of the model to a box field stimulus is shown in Figure 7.6. Three box field stimuli are applied with successively smaller transition delay times (2 ns, 300 ps, 50 ps), testing the speed at which the MRAM bit can toggle. The circle figures at the top indicate the orientations of the two free layers at each step in the sequence. The first, slow sequence shows the progression of the magnetic moments through the toggle sequence, moving to a spin flop state with application of the first H_y field (I_x) and rotating in step with the subsequent sequence. Following the first sequence after 10 ns, the orientation of the free layers has been reversed and the resistance of

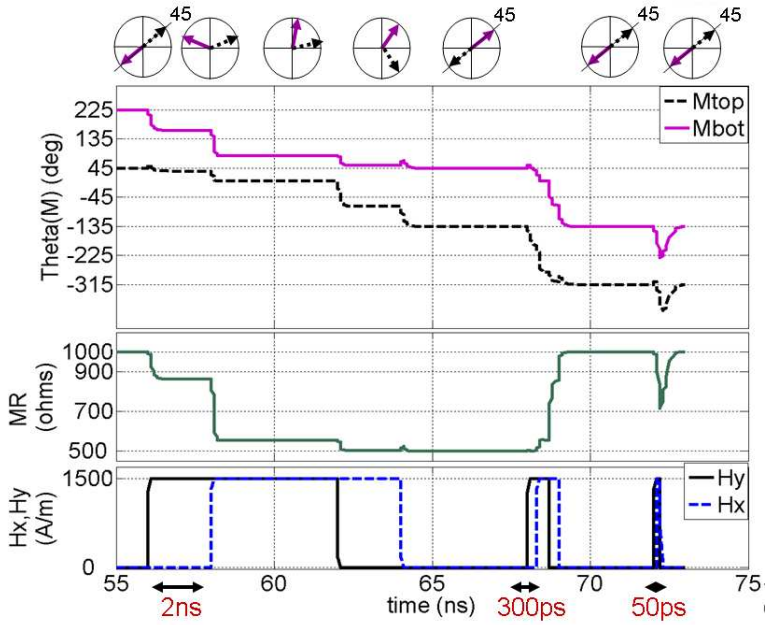

Figure 7.6: Response of the toggle MRAM model to three box field sequences with successively faster pulse edge timings: 2 ns, 300 ps and 50 ps. Circle figures at the top indicate directions of the free layer magnetizations at key time points in the sequence. The final pulse sequence fails to toggle the bit.

the device has changed from high to low. The dynamic response of the model is seen clearly in the first transition at 56 ns. The response of the magnetization is slow because it is initially in an unstable equilibrium in which there is very little net torque on the magnetic moments. In the second box field sequence starting at 68 ns the timing has been compressed so that there is only a 300 ps delay between the pulse edges. In the third sequence starting at 72.5 ns, the sequence has been further sped up so that the delay between the pulses is only 50 ps. The toggle operation fails in this case because the magnetic moments cannot respond fast enough.

7.2.3 Hybrid spintronic-CMOS circuit

The use of the Verilog-A MRAM model in a hybrid spintronic-CMOS circuit was demonstrated with a representative read/write circuit connected to the electrical ports of the Verilog-A model [circuit designed and simulation performed by colleague Michael Hall, Washington University, St. Louis, MO]. The circuit performs a read/write function with the wordline and bitline currents sourced by CMOS circuitry. A simple read amplifier is also included, providing a digital output. The schematic is shown on the left in Figure 7.7.

In this simulation, V_h has been set to 0.4 V, and the Read current through the tunnel junction is about 100 μA, resulting in a bias voltage, VMTJ1, of about 100 mV. As can be seen in the simulation results in Figure 7.8, the boxfield toggle sequence along the bottom row is repeated with three toggle cycles. Due to the initialization of the block in Verilog-A, the first toggle sequence does not begin with the top and bottom free layers exactly 180° apart in magnetization. However, by the beginning of the second toggle sequence at 20 ns, Mtop is at 45° and Mbot at 225° as expected. As the magnetoresistance, labeled ‘‘TMR,” steps up to its maximum value (only 970 Ω compared to Rmax = 1000 Ω due to the voltage bias effect) when the free layers become antiparallel in magnetization, the output of the sense amplifer, labeled as ‘‘Output (V)”, registers a ‘‘high” value or a ‘‘1”, and conversely for a low MR value when the free layers have parallel magnetizations. The second toggle sequence of Figure 7.8, beginning at 20 ns, mimics

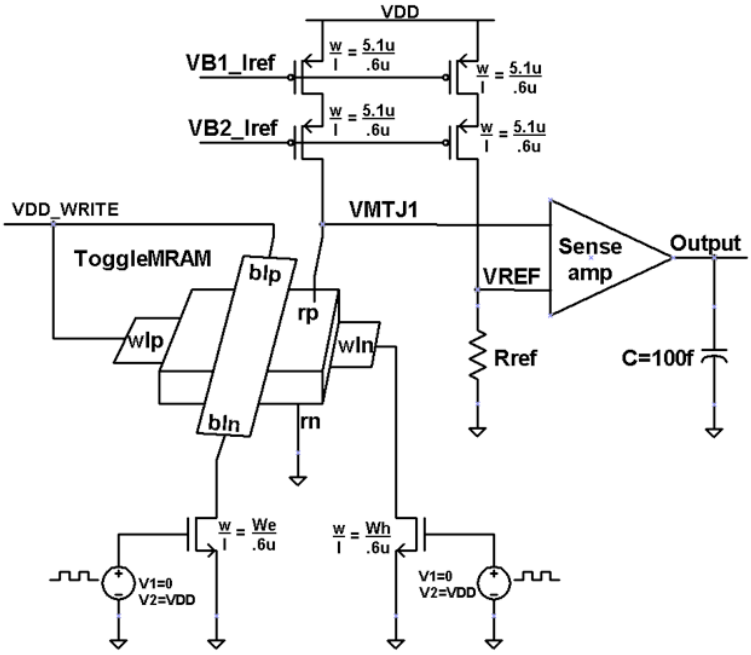

(a) Read/write circuit.

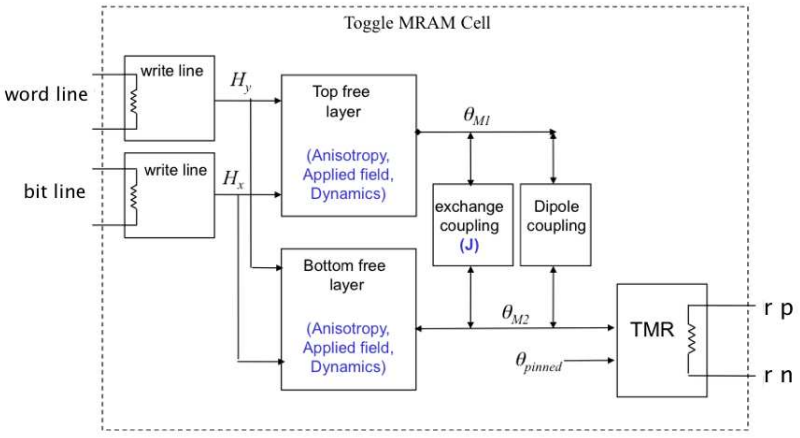

(b) Toggle MRAM cell block diagram.

Figure 7.7: (a) Hybrid spintronic-CMOS schematic of the read/write circuit used to simulate a set of boxfield toggle sequences. The toggle MRAM symbol contains the model shown in the block diagram of (b).

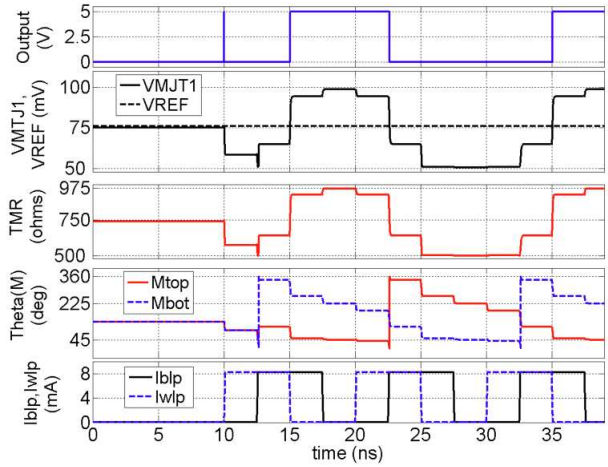

Figure 7.8: Simulation results for the spintronic-CMOS read/write circuit. Three repeated toggle sequences are shown, and in each sequence the magnetic moments of the top and bottom layers switch to directions opposite their starting angle and switch 180°. opposite each other. The sense amplifier output, "Output", is high for a high MR, and low for a low MR. The bias effect in the TMR module is enabled, consequently the TMR values are about 3% lower than with the bias effect disabled.

the first, slower boxfield sequence shown in Figure 7.6, except that the time between rising and falling edges of H_x and H_y is 2.5 ns in Figure 7.8, and only 2.0 ns in Figure 7.6.

7.3 3-D Spin valve with Oersted field switching

Several test situations were arranged using the 3-D single domain LLG block of Figure 4.5 as the core of the spin valve shown in Figure 7.9, to qualify the single domain model derived in section 4.5. In these simulations, I_z is a theoretical construct used to provide a field in the $\hat{\mathbf{z}}$ direction. The outputs of the single domain model are the polar and azimuthal angles of the magnetization θ and φ, and the output module is a magnetoresistive (MR) block (as opposed to TMR) appropriate for a non-magnetic spacer interlayer. The easy axis is set in both the single domain and MR modules, and is set to the $\hat{\mathbf{x}}$ axis in the figure, but this setting changes with the simulation cases. In most of the test cases that follow, only the field inputs and magnetization

Table 7.2: Toggle MRAM bit cell; model parameters and variables

Text symbol	Verilog symbol	Values used	Description
parameters			
w	w	1×10^{-6}	Write line width (m)
R	R	0	Write line resistance (Ω)
M_S	Ms	8×10^5	Sat. magnetization ($\frac{\mathrm{A}}{\mathrm{m}}$)
K_u	Ku	300	Uniaxial anisotropy ($^{\mathrm{J}}/_{m^3}$))
α	alpha	0.01	Gilbert damping parameter
θ_{EA}	M_ea	$^{\pi}/_4$	Easy axis angle (rad)
J	J	-1.8×10^{-5}	Exchange coupling ($^{\mathrm{J}}/_{m^2}$)
$a_{1,2}$	a1,2	300×10^{-9}	Length of long axis - free layer (m)
$b_{1,2}$	b1,2	150×10^{-9}	Length of short axis - free layer (m)
$t_{1,2}$	t1,2	3×10^{-9}	Free layer thickness (m)
$A_{1,2}$	A1,2	$a \cdot b \cdot \pi$	Area of elliptical bit (m^2)
R_{max}	R_max	1000	Maximum resistance (Ω)
R_{min}	R_min	500	Minimum resistance (Ω)
TMR	TMR	$\frac{R_{max}-R_{min}}{R_{min}}$	MTJ resistance ratio
$\mathrm{V_h}$	Vh	1×10^6, 0.4	MTJ bias at $^{TMR_0}/_2$ (V)
$N_{x1,2}$	Nx1,2	$^{2t}/_{\pi a}$	Demag. factor in-plane long axis
$N_{y1,2}$	Ny1,2	$^{2t}/_{\pi b}$	Demag. factor in-plane short axis
r	r	$0.2 - 0.7$	Dipole field atten. factor
J_{12} J_{21}	J_12 J_21	$\frac{1}{2}At\mu_0 M_S^2 r$	Dipole coupling (J)
Variables			
θ_{M1}	Theta(M1)		Top free layer magnetization angle (rad)
θ_{M2}	Theta(M2)		Bottom free layer magnetization angle (rad)
I	I(inn, inp)		Write line current (A)
$\mathrm{H_{x,y}}$	hout		Write line field ($\frac{\mathrm{A}}{\mathrm{m}}$)
	V(rp, rn)		Junction voltage (V)

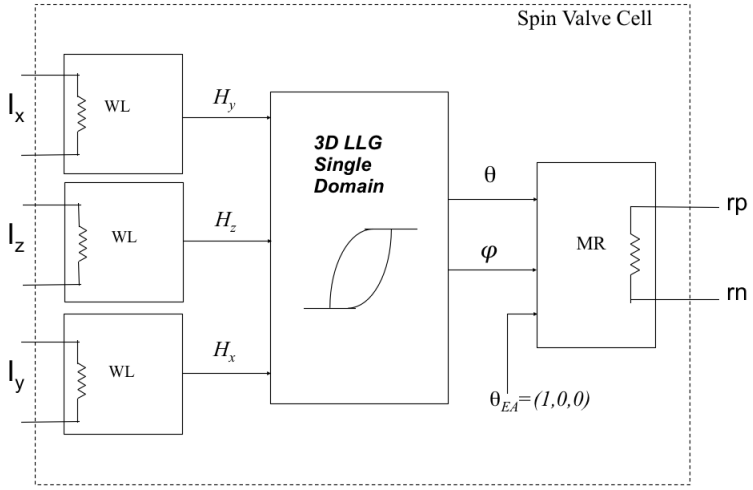

Figure 7.9: Spin valve cell using the 3D-single domain LLG block.

angle components θ and φ are plotted as outputs. In the Figures that follow, the red axis line in the 3-D xyz plots is always the easy axis, and is labeled "EA"; the dark (red) ball indicates the initial (θ, φ) setting - the starting point of the magnetization.

7.3.1 Oersted field sustained precession

Sustained precession tests for the correct precession frequency and dynamics in the absence of damping. The field was calculated to produce a precession cycle of the magnetic moment between 1 - 2 ns. When there is no damping torque ($\alpha = 0$), the gyromagnetic ratio $\gamma = 1.76 \times 10^{11}$ ($^{rad}/_{\mathrm{s}\cdot\mathrm{T}}$) will create a field-dependent precession of 35 $^{kHz}/_{\frac{\mathrm{A}}{\mathrm{m}}}$ according to equation 4.29 (the LLG equation). With $\hat{\mathbf{z}}$ set as the easy axis (0, 0, 1), and no crystalline anisotropy field, an applied field of 23 $^{\mathrm{kA}}/_{\mathrm{m}}$ in the $\hat{\mathbf{z}}$ direction should yield a precession frequency of 805 MHz, or a 1.242 ns cycle period. The test conditions are summarized in Table 7.3.

The initial angle for θ was set to 90° so that the precession would begin in the x-y plane (z=0), and φ began at 0°, which is (x,y,z) = (1,0,0) on the xyz plot. The simulated magnetization in Figure 7.10 is observed to remain in the x-y plane while φ rotates in a constant circle around the

3D spin valve: sustained precession	
Effective field terms included in simulation	*Parameter and field values*
uniaxial crystalline anisotropy (H_k)	$K_u = 300\ \left(\frac{J}{m^3}\right)$ $H_k \approx 300\ \left(\frac{A}{m}\right)$
shape anisotropy (H_d)	$H_d = 0$
external applied field(s) (H_a)	Transient: $23\ \frac{kA}{m}$ (46 mA)
Other parameters	
Gilbert damping factor (α)	0.02
Easy axis direction	$\hat{\mathbf{z}}$ axis, EA=(0, 0, 1)

Table 7.3: Field and parameter values used for the 3D spin valve transient simulation for sustained precession.

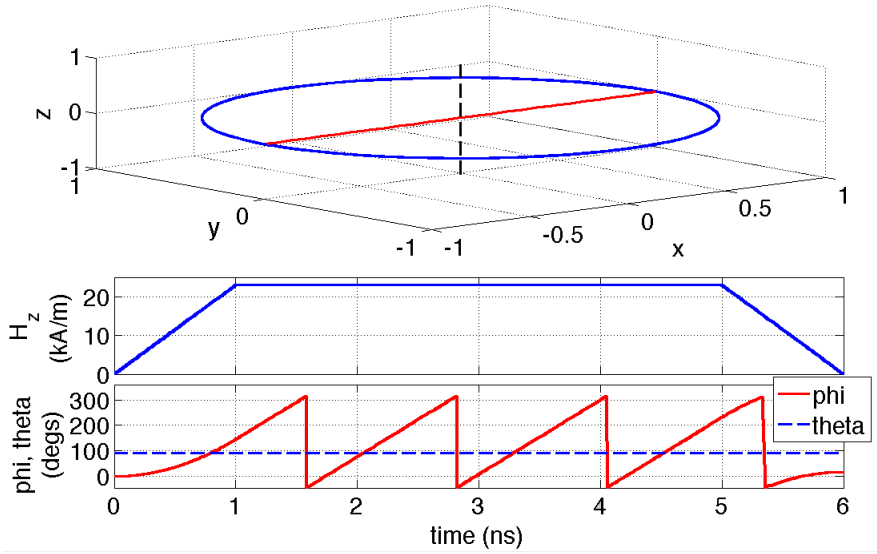

Figure 7.10: Top plot: 3-D xyz plot of sustained precession using applied field in the $\hat{\mathbf{z}}$ direction with easy axis set also in the $\hat{\mathbf{z}}$ direction (0, 0, 1); damping is set to zero. Bottom plot: H_z applied and the precession response of θ and φ over 4 precession cycles.

3D spin valve: uniaxial crystalline anisotropy	
Effective field terms included in simulation	*Parameter and field values*
uniaxial crystalline anisotropy (H_k)	$K_u = 300\ (J/m^3)$ $H_k \approx 300\ \left(\frac{A}{m}\right)$
shape anisotropy (H_d)	$H_d = 0$
external applied field(s) (H_a)	Transient: $H_y = 1.8\ \left(\frac{kA}{m}\right)$ and $2.5\ \left(\frac{kA}{m}\right)$
Other parameters	
Gilbert damping factor (α)	0.08
Easy axis direction	$\hat{\mathbf{x}}$ axis, EA=(1, 0, 0)

Table 7.4: Field and parameter values used for the 3D spin valve transient simulation for testing uniaxial anisotropy.

$\hat{\mathbf{z}}$ axis at a period of 1.242 ns per cycle as anticipated.

7.3.2 Applied field and uniaxial crystalline anisotropy

In this simulation, the uniaxial anisotropy code is tested. The easy axis was set to the $\hat{\mathbf{x}}$ direction (1, 0, 0) , uniaxial crystalline anisotropy was included ($H_k \approx 300\,\frac{A}{m}$) , and a hard-axis field (H_y) is applied and then removed so that the torque from the crystalline anisotropy could be shown to pull the magnetic moment back to the easy axis. To overcome the crystalline anisotropy and move the moment towards the hard axis, the applied field must be greater than the uniaxial anisotropy, H_k. The in-plane easy axis direction has $\theta = 90°$, $\varphi = 0°$, and for the moment $\mathbf{m}$ to point in the $\hat{\mathbf{y}}$ direction in the x-y plane, $\theta = 90°$, $\varphi = 90°$. Table 7.4 lists the test information. Two simulation plots are shown in Figure 7.11 to illustrate how the timing and field strength affect the results. In Figure 7.11(a) the field in the $\hat{\mathbf{y}}$ direction is applied for 50 ns and is 1.8 kA/m. Both the 3-D xyz plot and θ, φ vs. time plot show that the magnetization moves towards the H_y field but does not have time in the 50 ns field pulse to fully settle to $\theta = 90°$, $\varphi = 90°$. In both Figures 7.11(a) and (b) the magnetization dynamic in the xyz plots during the applied field pulse is indicated in green, and the blue portion of the curves indicate the magnetization precession when the applied field is zero, where the crystalline anisotropy field is pulling $\mathbf{M}$ back

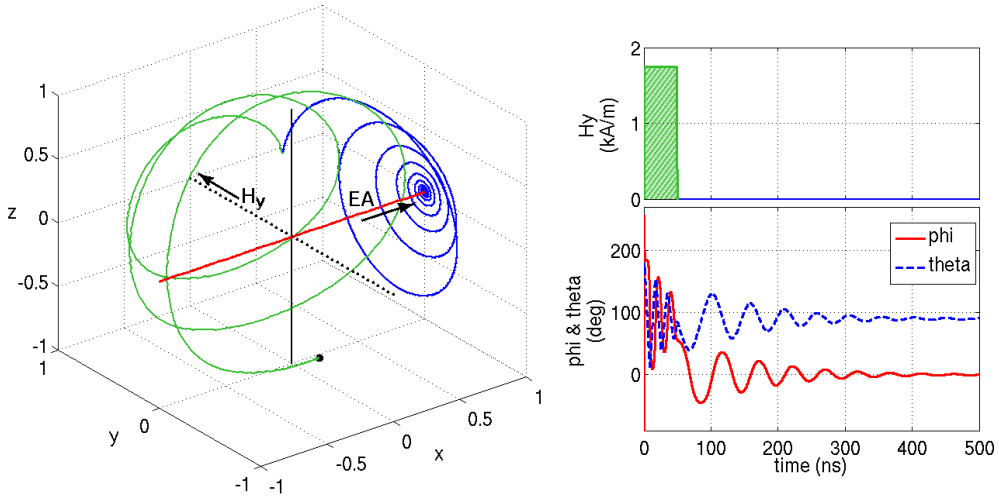

(a) Hard axis field applied for 50ns ($H_y = 1.8\,kA/m$).

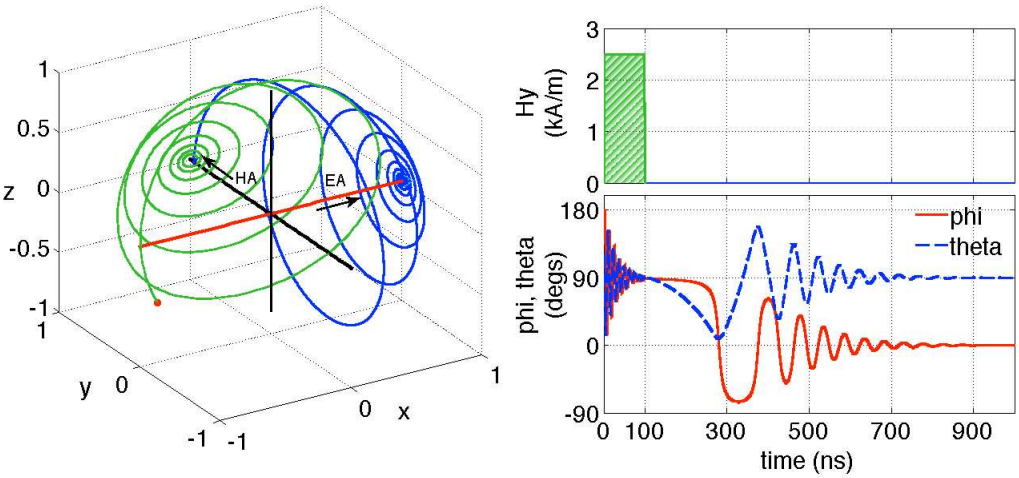

(b) Hard axis field applied for 100ns ($H_y = 2.5\,kA/m$).

Figure 7.11: 3D precession with applied field in the $\hat{\mathbf{y}}$ direction for (a) 50 ns, and (b) 100 ns, with easy axis set to the $\hat{\mathbf{x}}$ direction (1, 0, 0). In both (a) and (b), the magnetization dynamic in the xyz plot on the left, during the applied field pulse, is shown in green. The blue xyz curves occurs during the time that H_y=0. The H_y field pulse on the right is also shown in green.

3D spin valve: easy axis not a principle axis	
Effective field terms included in simulation	*Parameter and field values*
uniaxial crystalline anisotropy (H_k)	$K_u = 300\ (^J/_{m^3})$ $H_k \approx 300\ (\frac{A}{m})$
shape anisotropy (H_d)	$H_d = 0$
external applied field(s) (H_a)	Transient: $H_y = 5.0\ (\frac{kA}{m})$
interlayer exchange coupling (H_{ex})	
dipole coupling (H_{dip})	
spin transfer torque (H_{stt})	
Other parameters	
Gilbert damping factor (α)	0.08
Easy axis direction	EA=(1, 0, 1)

Table 7.5: Field and parameter values used for the 3D spin valve transient simulation for testing uniaxial anisotropy along a non-principle axis.

to the easy axis. If the field magnitude is increased and applied for a longer pulse duration (100 ns) as in Figure 7.11(b), the magnetization is able to reach the $\hat{\mathbf{y}}$ direction with $\theta = 90°$, $\varphi = 90°$ by the end of the applied field pulse. In both (a) and (b) it is apparent that when the field pulse goes to zero, θ remains in the x-y plane at 90°, and φ moves back to the easy axis at 0°. This is the expected behavior but it is noted that in Figure 7.11(a), the magnetization begins to precess back to the easy axis immediately as H_y goes to zero, while in Figure 7.11(b) there is a significant delay of about 100 ns. This occurs because in Figure 7.11(b) the magnetization has reached an unstable equilibrium at the y-axis and the torque moving the magnetization back to the easy axis is very small (almost zero) due to the very small angle of $\mathbf{M}$ relative to the y-axis. The anisotropy torque increases with the angle of $\mathbf{M}$ as it gradually moves away from the y-axis.

7.3.3 Easy axis not set to a principle axis

This test is similar to the preceeding test but further exercises the anisotropy code with a non-principle easy axis setting. The settings in Table 7.5 for this test are only slightly different from those in the previous simulation: Only uniaxial crystalline anisotropy is included ($H_k \approx 300\,\frac{A}{m}$) and the easy axis was set to the (1, 0, 1) direction. The applied field, $H_y = 5\,^{kA}/_{m} > H_k$ is applied

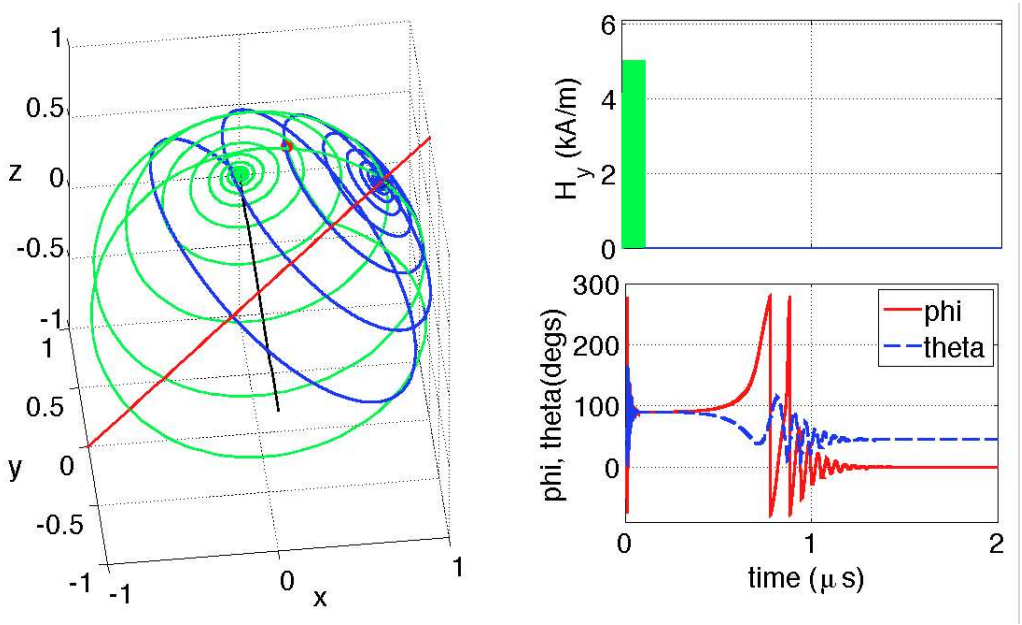

Figure 7.12: Easy axis set to (1, 0, 1) and applied field in $\hat{\mathbf{y}}$ direction, then removed. the magnetization dynamic in the xyz plot on the left, during the applied field pulse, is shown in green. The blue xyz curve occurs during the time that H_y=0. The H_y field pulse on the right is also shown in green.

for 100ns, then removed. The intent is to verify that when the applied field is removed, the easy axis setting is correctly followed, even though it is not along a principle axis; the anisotropy should force the magnetization back to the (1, 0, 1) direction. Just as in Figure 7.11 above, the green curve in the xyz plot indicates the precession dynamic during the applied field pulse, and the blue portion of the curve indicate the precession when the applied field is zero, where the crystalline anisotropy field is pulling $\mathbf{M}$ back to the easy axis. In Figure 7.12 the simulation begins at the dark (red) ball at the top of the plot where θ and φ were initialized to $\theta = 10°$, $\varphi = 15°$. The magnetization spirals towards the $\hat{\mathbf{y}}$ direction, bringing the moment all the way to the $\hat{\mathbf{y}}$ axis. When the H_y field is removed, the anisotropy gradually brings the magnetization back from its unstable equilibrium at the y-axis to the correct easy axis direction of $\theta = 45°$, $\varphi = 0°$.

3D spin valve: shape and uniaxial anisotropy	
Effective field terms included in simulation	*Parameter and field values*
uniaxial crystalline anisotropy (H_k)	$K_u = 300\ (J/m^3)$ $H_k \approx 300\ (A/m)$
shape anisotropy (H_d)	$N_y - N_x = 0.0333$ $H_{d(in-plane)} = M_S\,(N_y - N_x) = 26.6\,(kA/m)$
external applied field(s) (H_a)	Transient: $H_y = 6\ \left(\frac{kA}{m}\right)$ and $53.75\ \left(\frac{kA}{m}\right)$
Other parameters	
Gilbert damping factor (α)	0.08
Easy axis direction	$\hat{\mathbf{x}}$ axis, EA=(1, 0, 0)

Table 7.6: Field and parameter values used for the 3D spin valve transient simulation for testing uniaxial anisotropy.

7.3.4 Including the shape anisotropy, H_d

The demagnetization field is now included in simulations similar to those in section 7.3.2 in Figure 7.11. The intent and setup for the simulations are almost the same, except here the hard axis field in the $\hat{\mathbf{y}}$ direction has two settings,

1. $H_y = 6.0\,kA/m < H_k + H_d$ - not large enough to overcome the shape and uniaxial anisotropies, and

2. $H_y = 53.75\,kA/m > H_k + H_d$ - larger in order to overcome $H_k + H_d \approx 27\,kA/m$ with $H_{d(in-plane)} = M_S\,(N_y - N_x) = 26.6\,kA/m$.

The H_y field pulse is 600 ns to allow adequate settling time. The $H_{d\theta}$ field has a strong component due to the demagnetization factor N_z (see equation 4.51) which works to keep θ in the x-y plane at 90°. This should result in the magnetization following a more in-plane path. The two simulation cases are plotted in Figure 7.13 and the magnetization begins at the red ball near the bottom of the plot where θ and φ were initialized to $\theta = 150°$, $\varphi = -30°$. Table 7.6 lists the test conditions.

In Figure 7.13(a) the applied H_y field is only 6.0 kA/m, but the magnetization does approach the $\hat{\mathbf{y}}$ axis once $\mathbf{m}$ reaches the x-y plane. It is not expected that $\mathbf{m}$ should reach the $\hat{\mathbf{y}}$ axis because the field magnitude is less than the opposing fields, $H_k + H_d$. In Figure 7.13(b) the H_y

3D spin valve simulated as MRAM cell	
Effective field terms included in simulation	*Parameter and field values*
uniaxial crystalline anisotropy (H_k)	$K_u = 300\ (^{J}/_{m^3})$ $H_k \approx 300\ (^{A}/_{m})$
shape anisotropy (H_d)	$N_y - N_x = 0.0333$ $H_{d(in-plane)} = M_S\,(N_y - N_x) = 26.6\,(^{kA}/_{m})$
external applied field(s) (H_a)	Transient: $-80\ (\frac{kA}{m})$ and $40\ (\frac{kA}{m})$ Hysteresis: $-40\ (\frac{kA}{m})$ to $40\ (\frac{kA}{m})$ and back
Other parameters	
Gilbert damping factor (α)	0.02
Easy axis direction	$\hat{\mathbf{x}}$ axis, EA=(1, 0, 0)

Table 7.7: Fields and parameter values used for the 2D spin valve transient and hysteresis simulations.

field is almost 54 $^{kA}/_{m}$ and the magnetization just reaches the $\hat{\mathbf{y}}$ axis when the applied field is removed. Although these results are expected it is more interesting to compare these results with the simulations of section 7.3.2 which had $H_d = 0$. Compared to the large diameter spiral paths in the $\hat{\mathbf{z}}$ direction that $\mathbf{m}$ takes in Figure 7.11, $\mathbf{m}$ is constrained to more planar travel in Figures 7.13(a) and (b) due to the presence of the demagnetization field.

7.3.5 3-D static and dynamic response

Using the 3-D single domain model, hysteresis curves were generated for the three standard cases, 1) field applied along the easy axis, 2) field applied along the hard axis, and 3) a field applied at 45° to the easy and hard axes. Conditions are given in Table 7.7. These conditions are comparable to those used for the 2-D model simulations of section 7.1.1. The quasi-static curves have correct behavior and are shown in Figure 7.14. Each curve plots its magnetization component vs. its applied field direction. The square loop is created by a field along the easy axis ($\hat{\mathbf{x}}$), the diagonal line without hysteresis shows the coherent rotational response to the field in the $\hat{\mathbf{y}}$ direction, and the curved, dashed line shows the hysteretic response to a field 45° to the easy axis. This quasi-static simulation confirms that the dynamic 3-D LLG and the demagnetization

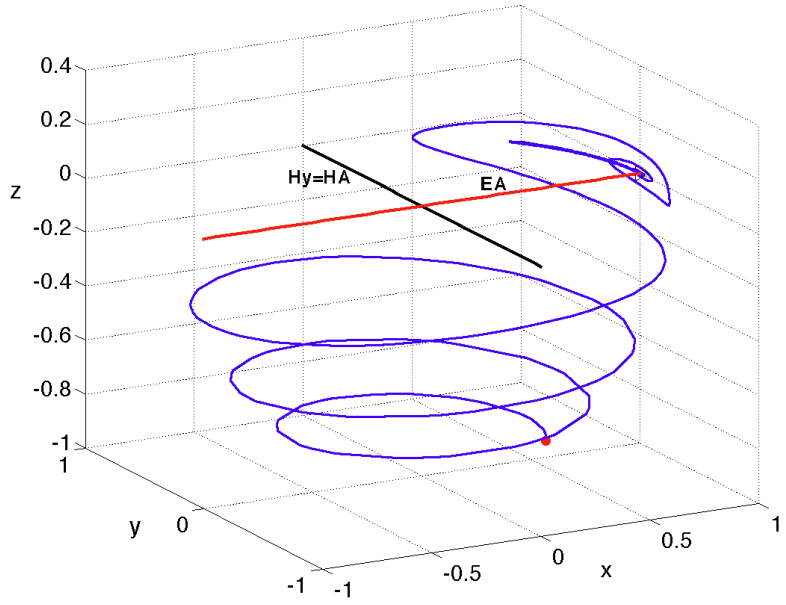

(a) 6kA/m field: $H_y < H_d + H_k$

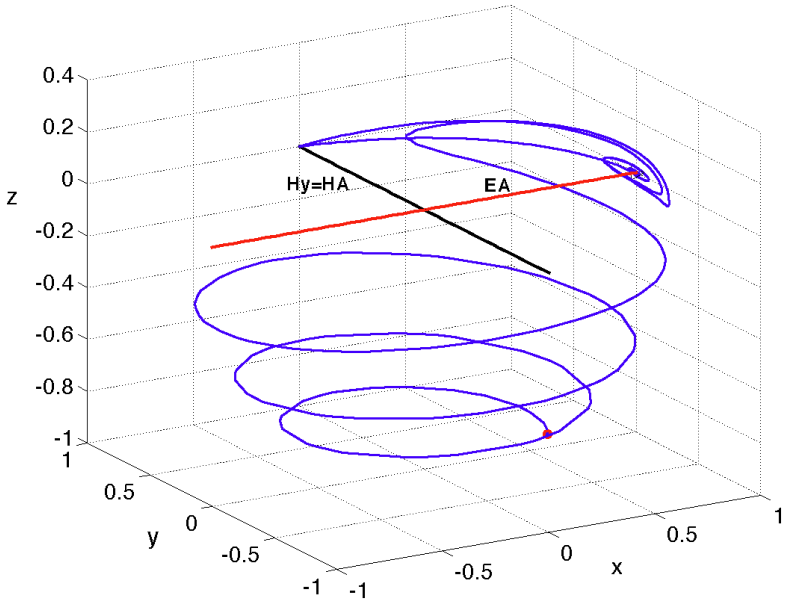

(b) 53.75kA/m field: $H_y > H_d + H_k$

Figure 7.13: Comparison of applied field (a) $H_y < H_d + H_k$ and (b) $H_y > H_d + H_k$.

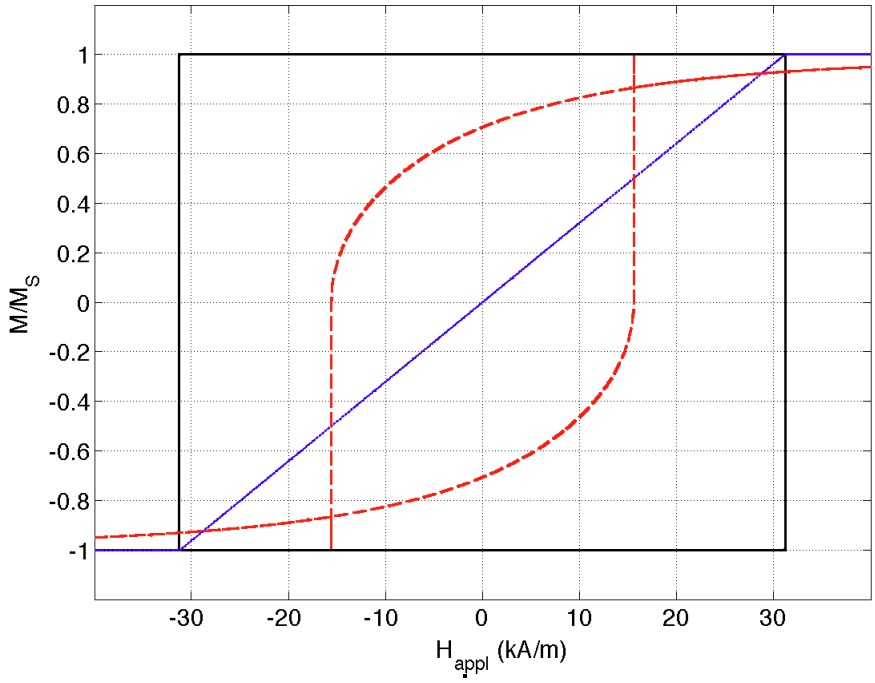

Figure 7.14: 3-D magnetostatic response. The black square magnetization loop is due to a field in the $\hat{\mathbf{x}}$ axis, the blue diagonal line without hysteresis is the response to an applied field in the $\hat{\mathbf{y}}$ direction, and the curved, dashed red line shows the magnetization response to a field 45° to the easy axis.

field code do not interfere with correct magnetostatic operation. For the dynamic response we once again plot the write line currents and their effect on the magnetoresistance in Figure 7.15(a). The results look similar to Figure 7.2 and use the same damping, but the out-of-plane precession appears here as oscillatory switching on the MR plot that is not present in the 2-D magnetoresistance curve. The write line pulses begin with a large, negative pulse on I_{y_word} to take the model out of equilibrium and force the free layer AP to the reference pinned layer. In the AP state, the MR changes from 500 Ω (low resistance state) to 1 kΩ (high resistance state). The next pulse is positve on I_{y_word} but at a half-select field level, and does not create sufficient field in the $\hat{\mathbf{x}}$ direction to switch the magnetization back to a P state. The third pulse on I_{x_bit} creates a half-select field in the $\hat{\mathbf{y}}$ direction which causes the magnetization to rotate toward the opposite direction but is not sufficient to completely switch it. Finally, both the write lines are

activated and the vector sum of their resultant fields at a 45° to the easy axis surpasses the switching field threshold and reverses the magnetization back to a P state with the pinned layer. This simulation scenario is also shown in an xyz plot in Figure 7.15(b). The simulation begins at the red dot (and also finishes at this point) which is (x, y, z) = (1, 0, 0) or the easy axis. With the reversal to the AP state, the magnetization undergoes a large-angle switching precession to (x, y, z) = (-1, 0, 0) . It remains at the negative easy axis until the third, H_y field pulse, when it moves slightly away from (-1, 0, 0) in a very small angle precession (hard to see) and then back to the negative $\hat{\mathbf{x}}$ axis. When the final, 45° field is presented, the magnetization makes another large angle precessional sweep towards the applied field and precesses around it (smaller loops near (1, 0, 0)), and switches back fully to the easy axis direction as the applied field vanishes.

An additional simulation of the dynamic response with the 3-D spin valve model was performed with $H_d = 0$. The simulation results are depicted in Figure 7.16. The time scale is much longer even using a larger damping factor compared to the 3-D simulation with H_d present (Figure 7.15); $\approx 1.1\,\mu s$ vs. $75\,ns$. When the demagnetizing field is disabled, the precession out-of-plane is unconstrained and takes longer to settle to a stable magnetization state, slowing the dynamic response dramatically.

7.4 3-D Spin valve using spin transfer torque

In this section a spin-polarized current is used in the model to apply spin transfer torque to an FM free layer. A means to supply the spin-polarized current to the 3-D single domain LLG module is needed as the MR output block only converts θ and φ into a magnetoresistance across the terminals rp and rn, yet these same terminals would also be used to conduct the STT current in a physical device. This requires the block diagram of Figure 7.9 to be updated to include the rp and rn terminals as in Figure 7.17. The outputs needed are only the angles θ and φ, so in these simulations, the rp and rn ports are used solely for the STT spin current, I_s. The goal of the following simulations is to show that the model equations will use the stimulus, I_s from

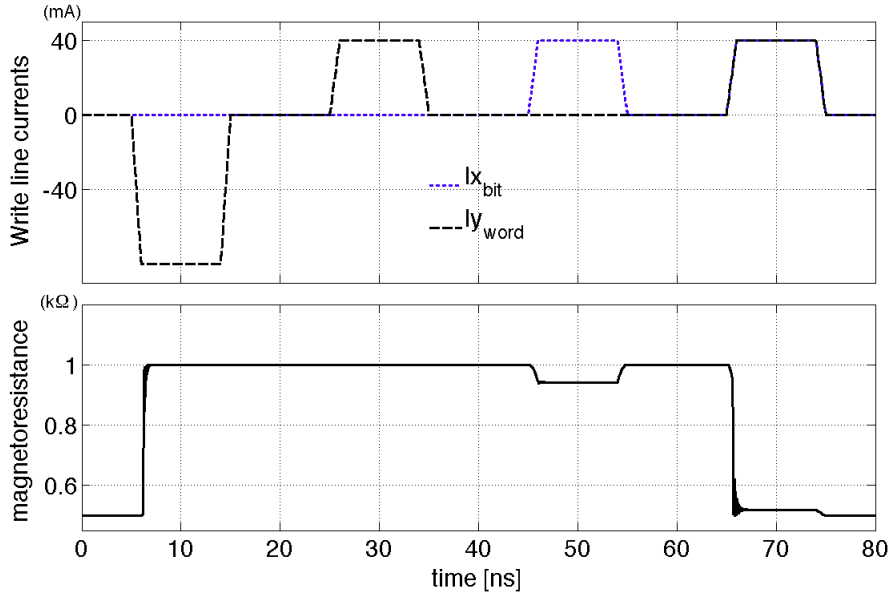

(a) Magnetoresistance as a function of H_a, ($H_k, H_d \neq 0$).

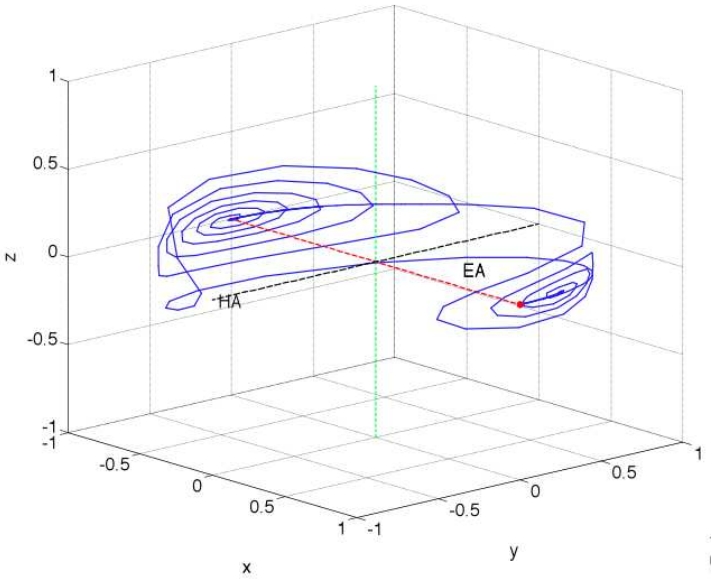

(b) xyz 3D plot of dynamic switching precession in (a).

Figure 7.15: 3-D dynamic response with shape anisotropy included, H_k,$H_d \neq 0$.

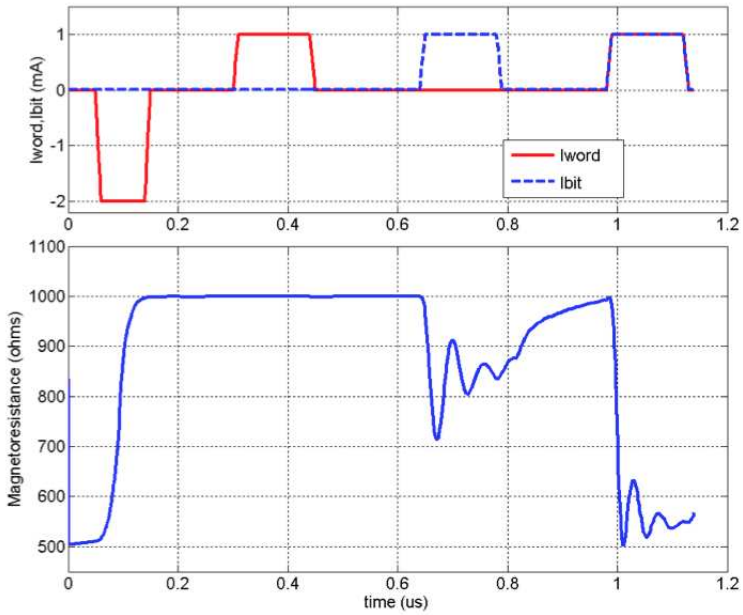

Figure 7.16: 3-D model dynamic response with $\alpha = 0.2$, but $H_d = 0$.

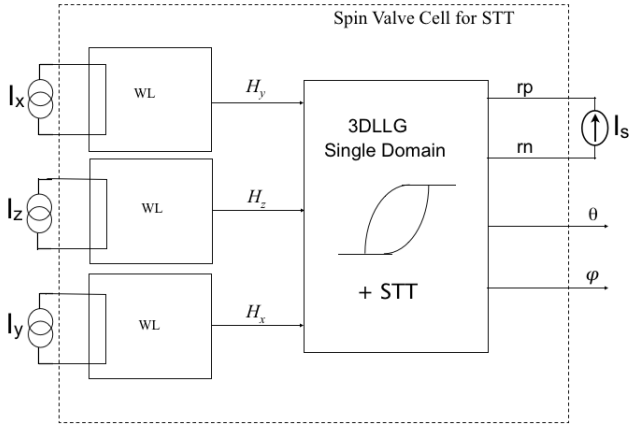

Figure 7.17: Spin valve block diagram using rp and rn ports to input spin current for STT simulation.

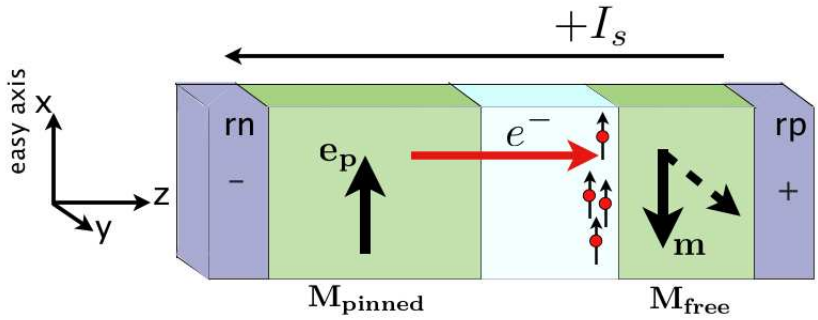

Figure 7.18: Spin valve layers with spin current (spin-polarizing electrons) originating from the polarizing layer, crossing to the NM spacer / free FM layer interface.

equations 4.57 and 4.58 to add a torque due to the spin current that will switch the free layer magnetization in a direction depending on the polarity of the applied current. There is a critical spin current to enable magnetization change predicted for this process

$$I_c = \frac{2e}{\hbar}\frac{\alpha}{G(\pi,0)}\mu_0 V M_S(\mathrm{H_{eff}}) \tag{7.1}$$

where $\frac{2e}{\hbar}$ is current per joules of energy, and the last term, $\mu_0 V M_S(\mathrm{H_{eff}})$, is the energy of the intrinsic and applied fields which need to be overcome for the magnetization switch to occur. The middle term, $\frac{\alpha}{G(\pi,0)}$, is the unitless spin transport factor which depends on the ratio of the damping factor, α, to the conductance of the layer stack as detailed in equation 4.59. $G(\pi)$ is proportional to the conductance of the device when the free and pinned layers are AP, and $G(0)$ when the layers are P. The critical current is not an exact switching value as it depends on the buildup of spin-polarized electrons at the interface; a longer current pulse with magnitude $\mathrm{I_s}$ may cause the free layer to switch whereas a shorter current pulse with the same magnitude may not.

7.4.1 Switching the FM free layer from AP to P with STT

A normal AP coupling for the spin valve is used as the initial state shown in Figure 7.18, and a positive spin current, $\mathrm{I_s}$ is produced from rp to rn such that a spin-polarized electron current

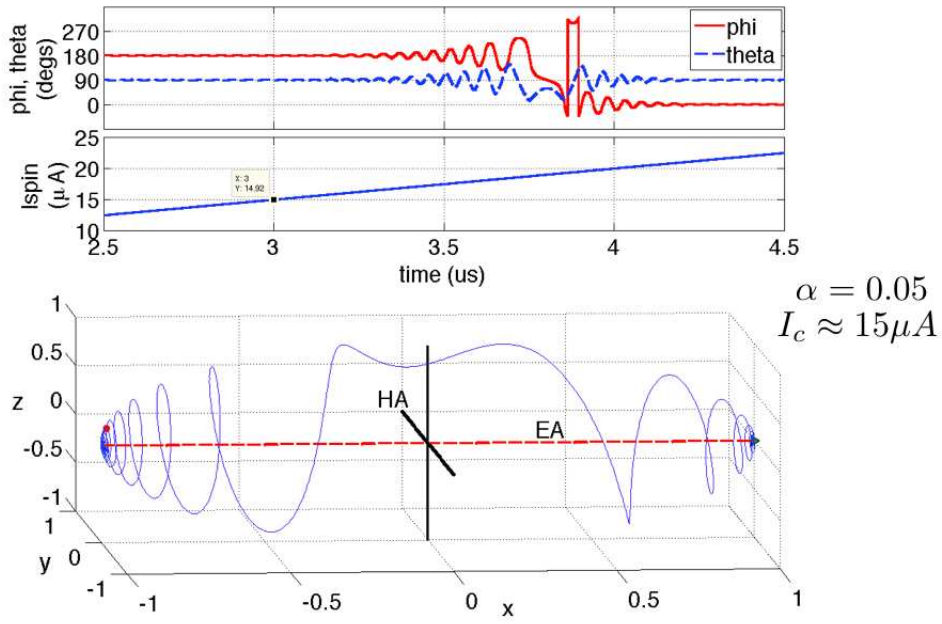

Figure 7.19: AP to P switching with I_s. Time domain graph (top) zoomed to switching region and 3-D xyz (bottom) plot.

flows from the polarizing/pinned layer through the spacer layer and exerts a torque on the free layer which will eventually flip the free layer magnetization to be parallel with that of the pinned layer. The torque will increase with the number of electrons at the spacer/FM interface whose spins are polarized in the direction of the pinned or polarizing layer, $\hat{\mathbf{e_p}}$. In order to find the approximate current at which the switching precession begins, a positive current ramp with a $^{5\,\mu A}/_{\mu s}$ slope was used for I_s. The results are shown in Figure 7.19. In the lower 3-D xyz plot, the simulation begins on the red ball at the left, close to the negative easy axis where θ and φ were initialized to $\theta = 80°$, $\varphi = 180°$ for an AP beginning state. The top time domain plot is zoomed in to show θ and φ changing with the spin current. There are no applied fields in this simulation with the exception of a very small 0.5 $^{kA}/_{m}$ field on H_z used to help the Spectre simulator with convergence, and only the anisotropy field H_k is present ($H_d = 0$) , so $H_{eff} \approx H_k$ (300 $^{A}/_{m}$). These conditions are summarized in Table 7.8.

When I_s is close to 0, **m** is influenced only by the anisotropy field and moves to the negative

3D spin valve: using STT for magnetization reversal AP → P	
Effective field terms included in simulation	*Parameter and field values*
uniaxial crystalline anisotropy (H_k)	$K_u = 300$ (J/m^3) $H_k \approx 300$ (A/m)
shape anisotropy (H_d)	$H_d = 0$
spin transfer torque (H_{stt})	$0\,\mu A \leq I_{spin} \leq 80\,\mu A$
Other parameters	
Gilbert damping factor (α)	0.05
spin-polarization factor (P)	0.35
Easy axis direction	$\hat{\mathbf{x}}$ axis, EA=(1, 0, 0)

Table 7.8: Field and parameter values used for the 3D spin valve using STT to reverse magnetization from AP to P.

easy axis ($\theta = 90°$, $\varphi = 180°$ or (x, y, z) = (-1, 0, 0)) completely AP with the polarizing layer. As I_s increases to around 8 μA (not shown), φ begins to oscillate on a small scale around 180°, and by 15 μA at 3 μs, both θ and φ show emergent oscillation. In the time between 3.3 - 4.3 μs the spin current has caused enough electron accumulation from the polarizing layer at the spacer/FM interface, to switch the magnetization in the free layer to $\theta = 90°$, $\varphi = 0°$ or (x, y, z) = (1, 0, 0). The angular changes in **m** in the time domain graph show the θ and φ rotations and in the xyz plot the 3-D precessional switching path followed by **m** is clearly indicated .

There is no exact spin current at which the switch in **m** takes place, but it is reasonable to place the critical current in the simulation between $8\,\mu A \leq I_c \leq 15\,\mu A$. If calculated with equation 7.1, $G(\pi) = 0.515$ is computed from equation 4.59 and $\alpha = 0.05$, giving $I_c = 4.5\,\mu A$. This is lower, but still in the approximate range of the observed critical current value.

7.4.2 Switching the FM free layer from P to AP with STT

The reverse situation from section 7.4.1 above is that the polarizing/pinned layer and the free layer begin in a P state. This case is not as intuitive as the former because now the spin current must be reversed ($-I_s$) , that is, the spin current will now flow from the free layer to the polarizing layer as in Figure 7.20. Because the layers are parallel in magnetization, the minority spin-down electrons

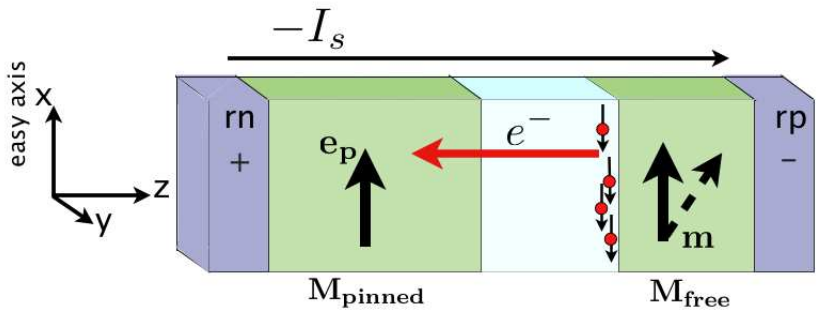

Figure 7.20: Layers with spin-polarizing electron current from the FM free layer.

will be confined in the spacer layer as discussed in section 2.3.2 and will transfer their change in angular momentum upon reflection to the electrons at each interface, until the free layer's magnetization is reversed. It is expected that this reflection process should require a larger spin current for the same switching period, which in the simulations is about 1 μs.

Two separate simulations were run in order to compare the effects of both damping factor and $G(\pi, 0)$ with the previous AP-to-P simulation. In the first simulation, $\alpha = 0.05$, which is the same α used in the AP-to-P simulation. The second simulation uses $\alpha = 0.08$. According to equation 7.1, the critical current is larger for larger α, and larger also if switching P-to-AP because beginning in the P state, $G(0) < G(\pi)$ by a factor of about 4. The test conditions are listed in Table 7.9.

The results shown in Figure 7.21(a) and (b) follow theory. In both figures (a) and (b), one observes the same kind of precessional switching in the time domain graphs as seen in Figures 7.19 and 7.11, with the comment that these are longer simulations and use larger timesteps so the angle changes in θ and φ look more discrete. However, comparing the I_c result from Figure 7.21(a) with the simulation of Figure 7.19 , both using $\alpha = 0.05$, it is clear that switching the free layer from a P to AP state requires more spin current than the reverse case, as predicted. In the P to AP test case of Figure 7.21(a), a maximum estimate for I_c is $\approx -65\,\mu$A (calculated value: 18 μA), while the AP to P test case of Figure 7.19 has a maximum estimate of $I_c \approx 15\,\mu$A (calculated value: 4.5 μA). Although these are higher values overall than the calculated values

3D spin valve: using STT for magnetization reversal P → AP	
Effective field terms included in simulation	*Parameter and field values*
uniaxial crystalline anisotropy (H_k)	$K_u = 300$ (J/m^3) $H_k \approx 300$ (A/m)
shape anisotropy (H_d)	$H_d = 0$
spin transfer torque (H_{stt})	a) $-80\,\mu A \leq I_{spin} \leq 0\,\mu A$ b) $-110\,\mu A \leq I_{spin} \leq 0\,\mu A$
Other parameters	
Gilbert damping factor (α)	a) 0.05 b) 0.08
spin-polarization factor (P)	0.35
Easy axis direction	$\hat{\mathbf{x}}$ axis, EA=(1, 0, 0)

Table 7.9: Field and parameter values used for the 3D spin valve using STT to reverse magnetization from P to AP.

of 18μA and 4.5μA of I_c for each case respectively, the correct trend is followed, and I_c is not being measured here with regards to a specific spin current pulse width.

Comparing Figures 7.21(a) and (b), it is also observed that a larger damping factor increases the magnitude of I_c also as predicted, with an $I_c = -65\,\mu$A for $\alpha = 0.05$, and $I_c = -92\,\mu$A for $\alpha = 0.08$. An interesting adjunct in the xyz plots of Figures 7.21(a) and (b) is the manner of the precessional characteristic: unlike the xyz plot of Figure 7.19 and other AP-to-P simulations, it seems that in P-to-AP STT switching, there is a very direct precession to the AP minimum energy state on the easy axis. In Figures 7.21(a) and (b) the simulations begin at the red ball at the right near the positive easy axis ($\theta = 80°$, $\varphi = 0°$) in which $\mathbf{m}$ is almost parallel with the magnetization of the pinned layer. At small negative values of I_s the anisotropy coerces $\mathbf{m}$ into the easy axis at (x, y, z) = (1, 0, 0) and is in a P magnetization state. As I_s increases in magnitude and approaches I_c, the data shows that $\mathbf{m}$ makes only two or three small-angle precessions and then switches directly to the AP state at $\theta = 90°$, $\varphi = 0°$, or (x, y, z) = (-1, 0, 0). The 3D switching characteristic indicates that the spin-dependent reflection process causes a build-up or large accumulation of minority-spin electrons at the spacer/FM interface very rapidly, causing an abrupt torque transfer and fast switching process. This is in contrast to the AP-to-P simulations which have all resulted in xyz plots like those of Figure 7.19, where the

magnetization precessional characteristic indicates a gradual torque transfer from a steady flow of electrons.

7.4.3 Steady-state precession initiated with STT from AP state.

Experiments were performed using the simulation model in Figure 7.17 and the simulation conditions suggested by Figure 5.7 (AP $\rightarrow$ IPP, low field and current case) in section 5.3.2 to cause steady-state precession with STT. The simulation setup is shown in Figure 7.22. Note that the axes have been rotated compared with those of previous simulations to facilitate graphing. The perpendicular direction to the multilayer is now along the $\hat{\mathbf{x}}$ axis and the easy axis is now $\hat{\mathbf{z}}$, and for θ to be in the thin-film plane, $\theta = 0^\circ$ or 180° (whereas before in-plane meant $\theta = 90^\circ$). The FM free layer begins AP to the polarizing/pinned layer, and a spin current is conducted through the multilayer such that the electron current will come from the polarizer. The applied field is in the -$\hat{\mathbf{z}}$ direction and needs only to be greater than the anisotropy field $H_k = 300\,{}^{A}/_{m}$, as H_d is set to zero. The H_z field keeps the magnetization of the free layer from directly switching P to M_{pinned}, opposing the spin torque. The steady-state precession frequency should increase with $|H_{eff}|$.

Two simulations are shown using the conditions listed in Table 7.10.

In the first simulation (case (a) in Table 7.10) shown in Figure 7.23, the initial settings for θ and φ are 179° and 90°, pointing $\mathbf{m}$ in the $-\hat{\mathbf{z}}$ direction. The H_z field is present from time 0, and φ begins immediately to rotate in the x-y plane. The spin current is not introduced for 2 μs, and at about 8 μs, θ begins to change to a larger precession cone angle in the positive $+\hat{\mathbf{z}}$ direction and φ simultaneously changes and slows its precession rate. By about 18 μs, θ has stabilized at an angle of 114°, and the precession frequency for φ is also stable, calculated from the lower φ (rad)-vs-time plot as

$$\frac{\Delta\varphi\,(rads)}{2\pi\Delta t} = 29.5\,\text{MHz}\ (33.9\,ns).$$

In the absence of the demagnetizing field, H_d, the Kittel relation [94] for ferromagnetic resonance

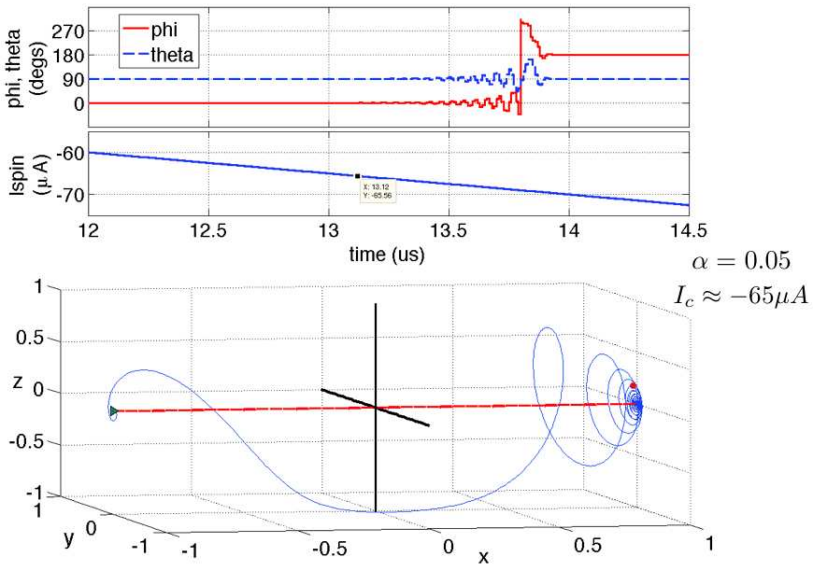

(a) $\alpha = 0.05$

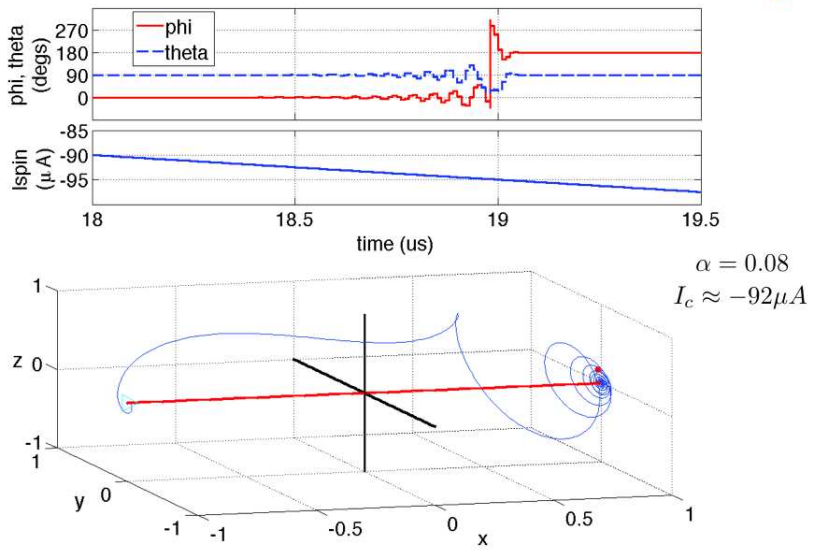

(b) $\alpha = 0.08$

Figure 7.21: P to AP switching with I_s.

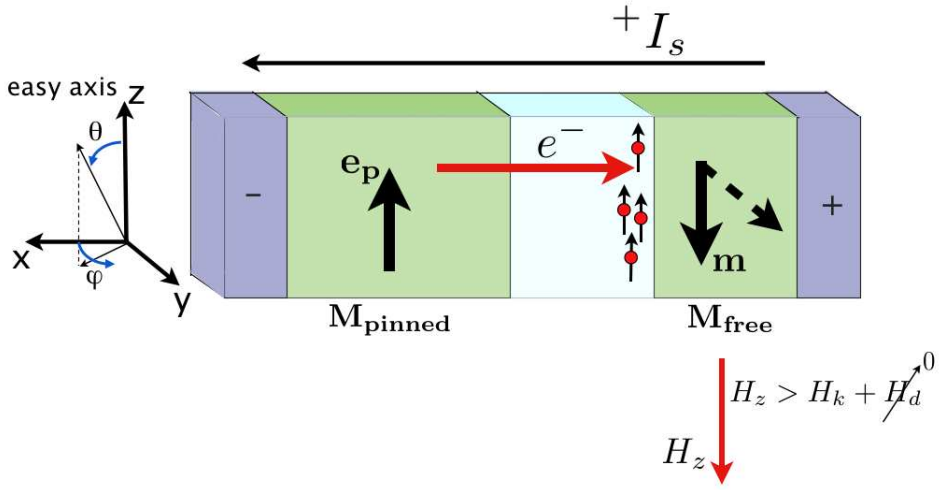

Figure 7.22: Conditions and setup for steady-state precession beginning in an AP state.

predicts the precession frequency with $H_{eff} = 900\,{}^{A}/_{m}$ as

$$f_{prec} = \frac{\gamma_0}{2\pi} H_{eff} = 31.6\,\text{MHz}\ (31.6\,ns).$$

The experimental result is different by about 7%, which can be due to the 0.1 ns (0.5 ns max) simulation timestep used. The precession slope was measured over approximately 277 cycles and it would take only 24 cycles to be off by .1ns to create the 2.405 ns difference between the calculated and experimental periods. The second simulation in Figure 7.24 was run with less accuracy (0.5 ns, 2 ns max timestep) and for only 20 μs. The purpose of this simulation was twofold - to verify the repeatability of entering the same dynamic phase region of the previous simulation, but with different parameters (case (b) in Table 7.10), and to show that the precession frequency does indeed increase with $|H_{eff}|$. For this purpose both I_s and H_z are increased as detailed above, but because a larger timestep is employed, the simulator does not converge without the addition of small $5\,{}^{A}/_{m}$ and $40\,{}^{A}/_{m}$ fields on H_x and H_y, respectively. These fields change the beginning of the simulation such that φ initially oscillates around its starting point of 90°, which is the $\hat{\mathbf{y}}$ direction, and settles at 90° until 2 μs when I_s is stepped to 11 μA. In the next

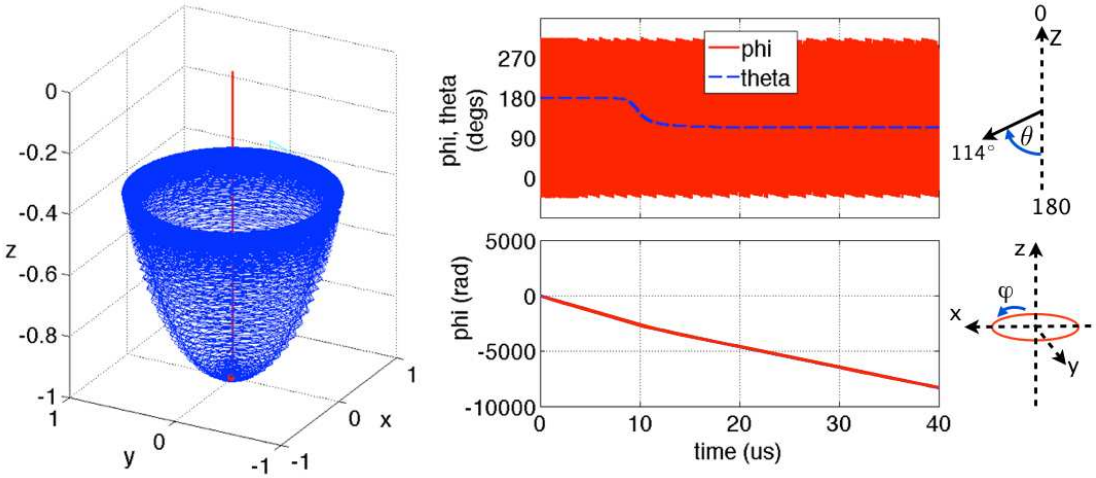

Figure 7.23: Steady-state precession AP -> IPP, $I_s = 9\,\mu A$.

Steady-state precession with 3D spin valve using STT, starting from AP state	
Effective field terms included in simulation	*Parameter and field values*
uniaxial crystalline anisotropy (H_k)	$K_u = 300$ ($^J/_{m^3}$) $H_k \approx 300$ ($^A/_m$)
shape anisotropy (H_d)	$H_d = 0$
effective applied fields (H_{eff})	$\lvert H_{eff}\rvert = \lvert H_k\rvert + \lvert H_z\rvert$ a) Figure 7.23: 900 ($^A/_m$) b) Figure 7.24: 1200 ($^A/_m$)
spin transfer torque (H_{stt})	a) $I_s = 9\,\mu$A step at 2 μs b) $I_s = 11\,\mu$A step at 2 μs
Other parameters	
Gilbert damping factor (α)	0.02
spin-polarization factor (P)	0.35
Easy axis direction	$\hat{\mathbf{z}}$ axis

Table 7.10: I_s and parameter values for a 3D spin valve using STT to operate in steady-state precession.

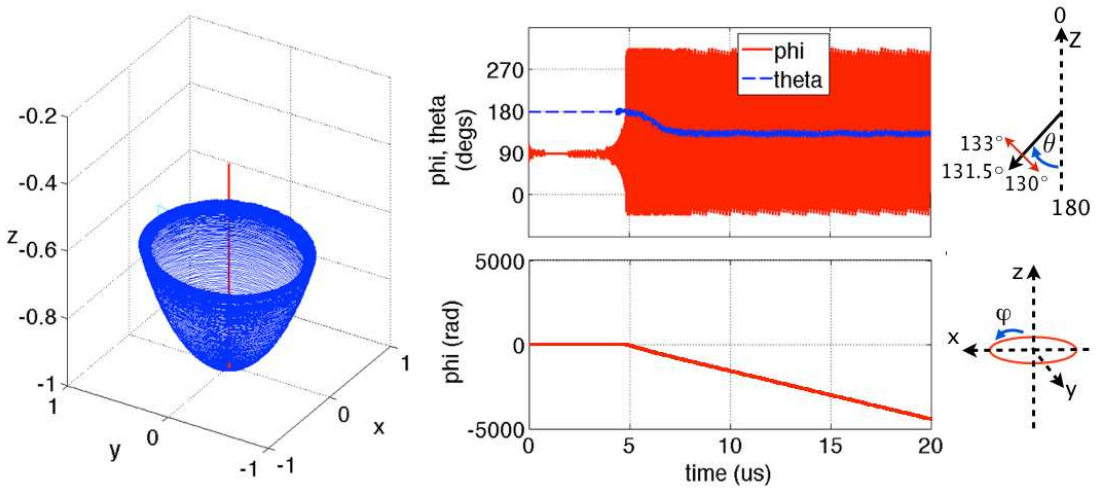

Figure 7.24: Steady-state precession AP -> IPP, $I_s = 11\,\mu A$.

4 μs, θ and φ change as before to reach a steady-state precession cone angle and frequency. It is interesting to note another effect of the H_x and H_y fields; they cause the precession angle to vary about its average value by $\pm 1.5°$ as φ makes a revolution around H_z. This total 3° difference in θ during a precession cycle can be seen as a slight tilt in the 3-D xyz plot of the precession cone angle, and also in the width of the θ line in the time domain plot, especially when compared to the constant θ vs. time line of Figure 7.23, where H_x and H_y were set to zero.

The measured average precession frequency is 45.6 MHz while the calculated frequency is 42.2 MHz, which is a difference of 8%. This is 1% more error than for case (a) in Table 7.10, but it is expected that the error would increase with increasing timestep. The simulation does show that the model's precession frequency does indeed increase with $|H_{eff}|$.

Simulations for the dynamic phase regions where steady-state precession occurs P -> AP have not been performed. Attempts to add the demagnetization field to the simulations in section 7.4 have had limited success due to convergence difficulties.

7.5 Model comparisons to published data

The simulation results above show that the model exhibits correct static and dynamic behavior, but many of the simulations have used an anisotropy field value that was unrealistically small whenever the shape anisotropy was not used in the simulation. This has kept the current levels for magnetic field switching and STT magnetization reversal in the 1 mA range and the 10 μA range for magnetic field and STT switching, respectively, which is about an order of magnitude too low for existing devices with the dimensions used. In this section we will compare the 3-D model's behavior to that of two research papers representative of published work which uses fabricated devices. For these examples, the dynamic magnetization reversal times will be compared using the papers' physical constants and intrinsic fields whenever they are reported.

7.5.1 Magnetization reversal using Oersted fields

The reference work is from [1] and uses a large 10 μm x 2 μm sample with a 15 nm thick NiFe free layer. The known parameters and test conditions are given in Table 7.11. The author's purpose is to demonstrate that although an applied field in-plane with the easy axis is used to reverse the magnetization of the free layer, the reversal occurs much faster if a small transverse field (H_y) is also applied. There are two simulations for the two field conditions. The first is shown in Figure 7.25(a) and has no transverse field applied, while the second simulation in Figure 7.25(b) has a transverse field of $H_y = 1.4 \left(\frac{kA}{m}\right)$ throughout the simulation.

The authors measure a forward (P to AP) switching time, τ_s, of 1.6 ns defining τ_s as the interval for 10% to 90% of the total change of $\mathbf{M}$ in the $\hat{\mathbf{x}}$ direction, M_x. They do the measurement physically using time-resolved scanning Kerr microscopy. We measure the model's time-domain output for the azimuthal, in-plane magnetization angle, φ, and use a straight line crossing at 180° and 0° to determine the magnetization reversal time. The approximate forward switching time from the model data is 1.74 ns. The reverse (AP to P) switching time measured on the physical device is 7.3 ns, slower than the forward τ_s due to the presence of only the small bias

3D spin valve: fields and parameters used in the model to match the reported physical parameters and conditions	
Effective field terms included in simulation	*Parameter and field values*
uniaxial crystalline anisotropy (H_k)	$K_{ueff} = 670\ (J/m^3)$ $H_k = 0\ \left(\frac{kA}{m}\right)$
shape anisotropy (H_d)	$N_y - N_x = 0.00463$ $H_{d(in-plane)} = M_S\,(N_y - N_x) = 3.68\ \left(\frac{kA}{m}\right)$ N_x, $N_y = \frac{2t}{\pi a}$, $\frac{2t}{\pi b}$, $a = 10\,\mu$m, $b = 2\,\mu$m, $t = 15\,$nm
external applied field(s) (H_a)	Simulation 1: $H_x = 4.8 - (-19.2)\ \left(\frac{kA}{m}\right)$ $H_y = 0\ \left(\frac{kA}{m}\right)$ Total switching field, $H_s = H_x = 24\ \left(\frac{kA}{m}\right)$ --- Simulation 2: $H_x = 4.8 - (-19.2)\ \left(\frac{kA}{m}\right)$, and $H_x = 7.65\ \left(\frac{kA}{m}\right)$, $H_y = 1.4\ \left(\frac{kA}{m}\right)$
Other parameters	
Gilbert damping factor (α)	0.02
Saturation Magnetization (M_S)	$820\ \left(\frac{kA}{m}\right)$
Gyromagnetic ratio (γ_0)	$1.41 \times 10^5\ \left(\frac{m}{As}\right)$
Easy axis direction	$\hat{\mathbf{x}}$ axis, EA=(1, 0, 0)

Table 7.11: Field and parameter values from [1] used for the 3D spin valve dynamic switching comparison simulation.

field in the positive easy axis direction of 4.8 $\left(\frac{\text{kA}}{\text{m}}\right)$. Of course, the physical device certainly has a crystalline anisotropy field, to assist the reversal. In the model, K_u was set to zero, letting the shape anisotropy term, H_d, determine the effective anisotropy. As a result, the model does not reverse switch (AP to P) after the 10 ns H_x pulse of -19.2 $\left(\frac{\text{kA}}{\text{m}}\right)$ unless the positive H_x field is raised from 4.8 to 7.65 $\left(\frac{\text{kA}}{\text{m}}\right)$. The reverse τ_s is measured from the data beginning where φ starts to change to where it just reaches a parallel condition. This is measured at 8.42 ns.

In Figure 7.25(b) the second case with a transverse field (H_y) applied is shown. Due to this field, reverse switching AP to P in the model simulation takes place immediately, without the need for increasing the positive H_x field. The measured reversal times from the physical data are given in the comparison table on the right. In case 1 (no H_y field) the percentage differences between the model and physical data for forward and reverse switching are 8% and 15%, respectively. For case 2 (with an H_y field) the forward and reverse differences are 23% and 3%, respectively. The percentages give only good agreement in the switching times of the physical device vs. the model simulation.

7.5.2 Magnetization reversal using an STT current

The published work used for this comparison is [40]. The physical device is a 100 nm x 50 nm thin film stack of Co/Cu/Co with a Co free layer, 3nm thick. The authors demonstrate a linear region for the switching time , τ_s, which is dependent on the amplitude of the pulsed STT current, I_s, and is indicative of spin angular momentum conservation. They also determine a curved onset for the thermal threshold of their device above which there is the linear dependence of τ_s on I_s, and below which the dynamics have a dependence on thermal perturbation. The threshold current they observed is between 10 and 11 mA. The conditions and parameters from this work used in the model simulation are listed in Table 7.12.

The results of the model simulation and physical device experimental data are shown together in Figure 7.26. The authors' experimental data has many hundreds of averaged data points over

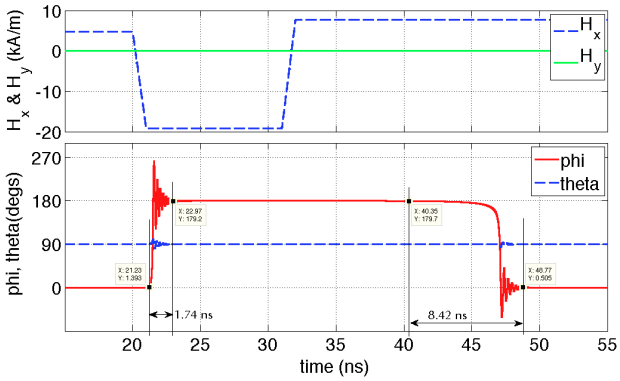

$H_y = 0$	Forward τ_s	Reverse τ_s
Physical device	1.6 ns	7.3 ns
model	1.74 ns	8.42 ns

(a) Magnetization reversal with no transverse field ($H_y = 0$). Reversal times compared with those of a physical device.

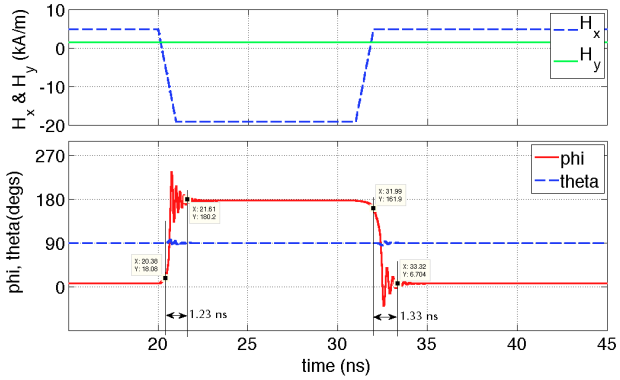

$H_y = 1.4 \left(\frac{kA}{m}\right)$	Forward τ_s	Reverse τ_s
Physical device	1 ns	1.3 ns
model	1.23 ns	1.33 ns

(b) Magnetization reversal using transverse field. Reversal times compared with those of a physical device.

Figure 7.25: Magnetization reversal (P to AP to P) experiments using parameters and fields of a reported physical device. (a) Reversal using a bias field along the easy axis ($\hat{\mathbf{x}}$ axis) of 4.8 $\left(\frac{kA}{m}\right)$, with a switching field of $H_x = -19.2$ $\left(\frac{kA}{m}\right)$ used to reverse $\mathbf{M}$ antiparallel. $H_y = 0$. After the 10 ns switching pulse, the positive H_x field must be raised to 7.65 $\left(\frac{kA}{m}\right)$ to get $\mathbf{M}$ to reverse again parallel with the easy axis, in the absence of a crystalline anisotropy field. The physical device switches back parallel without additional field. The vertical lines indicate approximate switching times, also reported in the accompanying table. (b) Reversal with a transverse field applied, H_y =1.4 $\left(\frac{kA}{m}\right)$. Switching times P to AP and AP to P are very similar.

3D spin valve: using STT for magnetization reversal AP → P	
Effective field terms included in simulation	*Parameter and field values*
uniaxial crystalline anisotropy (H_k)	$K_u = 0$ (J/m^3) $H_k = 0$ (A/m)
shape anisotropy (H_d)	$H_d = 3.66 \times 10^4$ (A/m) $N_y - N_x = 0.0254$
spin transfer torque (H_{stt})	$6\,mA \leq I_s \leq 12\,mA$
external applied field(s) (H_a)	$H_x = 14.65$ $\left(\frac{kA}{m}\right)$ $H_y = 0.05$ $\left(\frac{A}{m}\right)$
Other parameters	
Gilbert damping factor (α)	0.0326
spin-polarization factor (P)	0.38
spin transport and polarizing factor (η) or G(ψ)	0.5 (typical value for switching AP to P with $0.35 \leq P \leq 0.4$)
I_s pulse width, (τ_s)	100 ns
Saturation Magnetization (M_S)	1.44×10^6 $\left(\frac{A}{m}\right)$
Gyromagnetic ratio (γ_0)	1.76×10^{11} $\left(\frac{m}{As}\right)$
Easy axis direction	$\hat{\mathbf{x}}$ axis, EA=(1, 0, 0)

Table 7.12: Field and parameter values used for the 3D spin valve using STT to reverse magnetization from AP to P in Co/Cu/Co nanopillars.

thousands of current sweeps, so only a few points are displayed here that represent the physical device curve for comparison. The switching frequency, $\frac{1}{\tau_s}$, was found to be linear with I_s above 10 mA (10 MHz, $\tau_s \geq 100$ ns). The model data was taken only for current pulses with 100 ns widths. The 3-D model curve compares well with the experimental curve only at the 11 mA data point. There are two main reasons for the difference in the curves. The first is that model does not include thermal effects, which have the effect of adding a curvature onset at the zero-temperature threshold current, I_{c0}, rescaling the current threshold, I_c , by a factor of $[1 - (k_B T/E)\, ln\, (\tau/\tau_0)]$ where $k_B T$ is the thermal activation energy, τ is the thermal activation lifetime, τ_0 is the inverse of the nanomagnet's attempt frequency (the frequency at which the nanomagnet's moment attempts to reverse it's direction by overcoming its thermal energy barrier) , and E is the actual barrier height of the nanomagnet determined by its size, shape, intrinsic anisotropy and applied field strength. The second reason concerns the paper's choice of the

barrier height, $E = E_0 \left(1 + \frac{\mathrm{H}}{\mathrm{H_d}}\right)^2$ where E_0 is the zero-applied-field energy of the nanomagnet. In their work, the authors choose a value for the ratio of E_0 to the thermal energy based on their experimental data, ie., $\frac{E_0}{k_B T} = 120$. This choice determines important parameter values for the system such as the applied field, H, and the effective anisotropy field, $\mathrm{H_d}$, which are back-calculated for use in the model and simulation. The authors show that the slope of the curves in Figure 7.26 are dependent on the ratio, $\frac{\mathrm{H}}{\mathrm{H_d}}$. Their data follows a curve with $-0.4 \leq \frac{\mathrm{H}}{\mathrm{H_d}} \leq -0.3$ whereas the model simulation curve matches more closely a curve with $\frac{\mathrm{H}}{\mathrm{H_d}} \approx -0.6$. For each of the six points plotted from the model simulation, the reversal time measured was from the onset of the current pulse to full reversal of the magnetization angle, φ. This measurement method may not be comparable to what was used experimentally (not disclosed), generating possibly longer reversal time values compared to the paper's data.

In general, the model's simulation data is only valid in the linear region above $10\,\mathrm{mA} \leq I_s \leq 12\,\mathrm{mA}$, where the reversal times are around $4.2 \pm 0.03\,\mathrm{ns}$ with an average switching frequency calculated as $\tau^{-1} = 237.72\,\mathrm{MHz}$. In the same range for the experimental data, there is a higher slope and much more variation with $2.0 \leq t_{rev} \leq 14.3\,\mathrm{ns}$. Because the authors do not specify actual values for their shape anisotropy and applied field terms, it is difficult to make a one-to-one comparison of the model settings to a device.

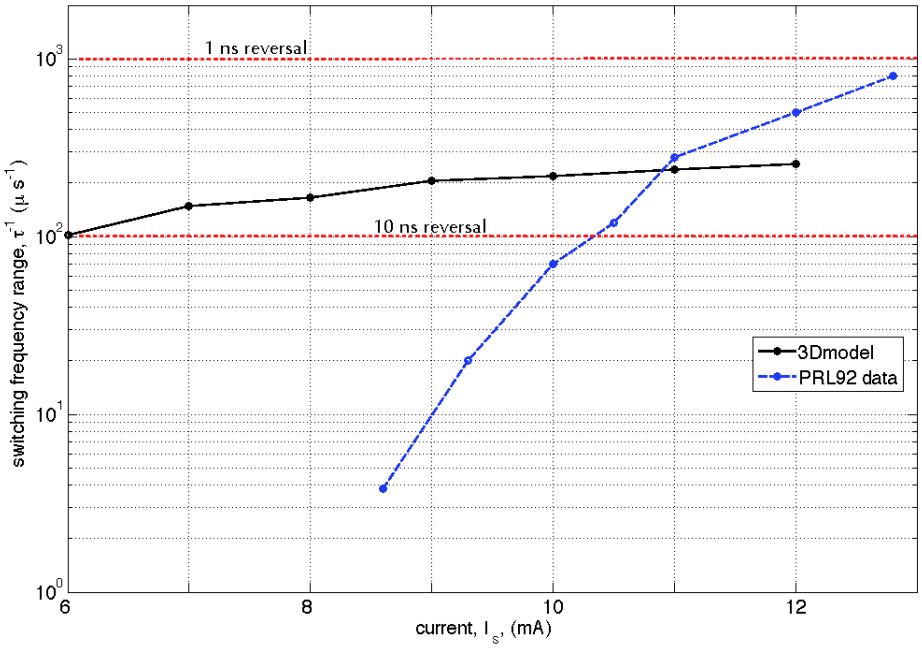

Figure 7.26: Experimental and model simulation data of the switching frequency, $\frac{1}{\tau_s}$, in reversing the magnetization of a Co/Cu/Co nanopillar AP to P, using an STT current, I_s.

Chapter 8 – Conclusion

This work has covered several important phenomena in nanoscale magnetics. I have attempted to qualitatively describe these phenomena and show their bearing in models of currently relevant device structures. To this end each behavior has been described mathematically in both two and three dimensions, as either a torque or an effective field (which is proportional to the torque by $\mu_0 V M_S$). The implementation language, Verilog-A, accepts the mathematical description directly, but the choice of how to describe the system so that the equations are efficiently solved is an important aspect of the modeling process. The models presented here rely on the equations of torque or field (proportional to torque), being solved for the equilibrium condition where the torques sum to zero at the magnetization node(s), θ (two dimensions), or θ and φ (three dimensions), where the system energy is minimized. This algorithm has been shown to be a successful procedure in solving for the time-domain change of the magnetic moment(s) in a thin film free layer(s) subject to internal and external fields. The model that has been developed has an advantage over currently reported models [27, 95] because it is executed in spherical coordinates maintaining a constant magnetization magnitude in keeping with a macrospin system. The model allows simulation of magnetization precession in three dimensions which is important to the accuracy of switching dynamics.

Further, nanoscale device structures of a spin valve, Toggle MRAM bit, and a spin valve using spin transfer torque, have been modeled and successfully demonstrated in two operational modes; magnetic moment reversal using Oersted fields and STT, and steady-state precession (STT), using the torques/fields and parameters significant to each. There is validation for the toggle MRAM device model. The parameters used in the simulation of this model were derived from Worledge's magnetic phase diagram of coupled nanomagnets [93] which included details of the exchange coupling parameter vs. intrinsic anisotropy (dimensions and demagnetization factors)

for the synthetic antiferromagnetic free layers. With the addition of dipole coupling between the coupled free layers, the model used material constants, fields, and dimensional parameters from Worledge's MRAM modeling paper [35]. Our simulations, using realistic intrinsic and applied field values, successfully reproduced Worledge's hysteresis results for free layers of the same thickness as shown in Figure 7.5. Although no numerical field values were reported with Worledge's hysteresis result, the detailed switching and spin-flop phases are exactly as in his model. Worledge's model is verified by early toggle MRAM work done by [34, 37].

With regard to magnetic moment reversal, the model's dynamic performance has been compared to work published on physical devices where Oersted fields and STT currents were used to stimulate switching. In these comparisons, all physical parameters and test conditions given in the papers were included in the model and simulation setup. The spin valve, switched with Oersted fields [1] from currents in the plane of the device, showed good agreement between the model's reversal times and those of the physical device. The comparison performed for magnetization reversal using STT currents [40] was not as clear, due to 1) the model's lack of a thermal effect, 2) not having a measured value for the anisotropy constant of the physical devices, and 3) not knowing if the field calculated from the paper's energy constant was actually applied in the physical experiment. With these shortcomings, the three valid simulated reversal times from the model were only within 4 ns of the analogous physical device data points. Even though these points are in the linear (high frequency) region of operation, the resulting model curve is in disagreement with the physical device measurement. It is very likely that the experimental parameters were misunderstood, since the model using STT, as shown in the simulation figures throughout section 7.4, behaves correctly. The thermal effect is very important at longer switching times and is work yet to be done to complete this model.

The structures emulated in this work are fundamental devices for the development of future spintronic elements. The model components may be reused in different physical layer arrangements in the construction of a new device (the Toggle MRAM device is a good example of this). The present state of the three dimensional single domain LLG module introduced in section 4.4,

requires that the model be updated with any new fields that may be required for a new structure. This is a drawback to the 3-D model, however, the module code may be changed to allow blocks with additional fields to be schematically- or port-connected and summed within the core LLG module in which the final sum and integration of all the field terms takes place.

The models presented in this work will be published [The 2-D spin valve and Toggle MRAM models already are. [96, 97]] making them publicly available. The availability will serve to assist research in testing new device structures without complex and lengthy micromagnetic simulations. The models will also make it easier for IC design companies to try incorporating magnetic devices in electronic systems, thus encouraging innovation with these devices.

8.1 Appendix 1: Symbols used in manuscript

V	Volume $\left[\mathrm{m}^3\right]$
A	Area $\left[\mathrm{m}^2\right]$
I	Current [A]
V	Volt [V]
n	Number of states
wb	Weber $[\mathrm{V}\cdot\mathrm{s}]$
P	Spin polarization $[\uparrow\downarrow]$
T	Tesla $\left[\frac{\mathrm{wb}}{\mathrm{m}^2}\right]$
J	Joule (Energy)
A_{ex}	Material exchange stiffness $\left[\frac{\mathrm{J}}{\mathrm{m}}\right]$
μ_0	Permeability of free space $\left[4\pi\times10^{-7}\frac{\mathrm{wb}}{\mathrm{A}\cdot\mathrm{m}}\right]$
$\mu_{\mathbf{m}}$	Atomic magnetic moment $\left[\mathrm{Am}^2\right]$

μ_B	Bohr magneton (Atomic spin magnetic moment) $= 0.927 \times 10^{-23}$ $\left[\mathrm{Am}^2\right]$
γ	Gyromagnetic ratio of material $\left[common: 1.76 \times 10^{11} \frac{\mathrm{c}}{\mathrm{Kg}}\ or\ \frac{\mathrm{rad}}{\mathrm{s \cdot T}}\right]$
γ_0	Gyromagnetic ratio $\left[\gamma_0 = \mu_0 \cdot \gamma,\ 2.21 \times 10^5\ \frac{\mathrm{m}}{\mathrm{A \cdot s}}\right]$
e	Electron charge, coulombs $\left[1.602 \times 10^{-19}\,\mathrm{c}\right]$
$\hbar$	Planck's constant divided by 2π $\left[1.005 \times 10^{-34}\ \mathrm{J \cdot s}\right]$
ω	Angular frequency $\left[\frac{\mathrm{rad}}{\mathrm{s}}\right]$
J_{ex}	Exchange integral or constant $\left[\frac{\mathrm{J}}{\mathrm{m}^2}\right]$
$\mathbf{L}$	Orbital angular momentum, $\hbar\sqrt{l(l+1)}$ $\quad[\mathrm{J \cdot s}]$
$\mathbf{M}$	Magnetization vector $\left[\frac{\mathrm{A}}{\mathrm{m}}\right]$
$\mathbf{m}$	magnetic moment $\left[\mathrm{Am}^2\right]$
$\mathbf{B}$	Magnetic flux density vector $\left[\mathrm{T\ or}\ \frac{\mathrm{wb}}{\mathrm{m}^2}\right]$
$\mathbf{H}$	Magnetic field vector $\left[\frac{\mathrm{A}}{\mathrm{m}}\right]$
$\mathbf{T}$	Torque vector $\left[\frac{J}{\mathrm{rad}}\right]$
$\mathbf{S}$	Spin angular momentum, $\hbar\sqrt{s(s+1)}$ $\quad[\mathrm{J \cdot s}]$
$\mathbf{J}$	Total angular momentum, $\mathbf{J} = \mathbf{L} + \mathbf{S}$, $\hbar\sqrt{j(j+1)}$ $\quad[\mathrm{J \cdot s}]$
θ_M	In-plane (2D) or polar (3D) angle of magnetization [degrees, °]
θ_{Pinned}	Angle of magnetization of pinned FM layer [degrees, °]

8.2 Appendix 2: Verilog-A module code

The following code modules may be schematically connected as in Figures 5.3, 5.4(b), 7.9, or 7.17, or may be instantiated by module name in a single top-level cell (as in Listing 7 below) if using Verilog-AMS. Listings 1 - 7 are for the 2-D model dynamics approximation. The 3-D single domain module is in Listing 8 and must be used with the 3-D magnetoresistance block in Listing 10 if a magnetoresistive output is desired. Likewise with the 3-D single domain block with STT, Listing 9, the 3-D magnetoresistance block must also be used. The parameters to be set in each file are at the beginning of the file with existing values. Some "strobe" (print) commands have been left in the longer modules to allow the user to observe certain signals of interest.

Listing 1. Write Line module (writeline)

```
'include ''constants.vams''
'include ''disciplines.vams''
module writeline(vp,vn,hwrite);
inout vp, vn;
output hwrite;
electrical vp, vn;
sig_flow_H hwrite;
parameter real W = 1.0u; // write line width [m]
parameter real R = 0; // line resistance [ohms]
analog begin

    V(vp,vn) <+ R*I(vp,vn);
    H(hwrite) <+ I(vp,vn)/(2*W);

end
endmodule
```

Listing 2. Magnetoresistance module (mr)

```
'include ''constants.vams"
'include ''disciplines.vams"
module mr(M1,M2,rp,rn) ;
inout M1,M2,rp,rn ; rotational M1,M2 ;
electrical rp,rn ;
parameter real R_max = 1000 ; // High resistance [ohm]
parameter real R_min = 500 ; // Low resistance [ohm]
analog begin

    V(rp,rn) <+ I(rp,rn)*(R_min+0.5*(R_max-R_min)*(1-cos(Theta(M1)-Theta(M2))));

end
endmodule
```

Listing 3. Single Domain module (single_domain)

```
'include ''constants.vams"
'include ''disciplines.vams"
nature Magnetic_Induction

    abstol = 1e - 12;
    access = H;
    units = ''A/m";

endnature
discipline sig_flow_H

    potential Magnetic_Induction ;

enddiscipline
'define P_gamma 1.76e11 // Gyromagnetic constant [Hz/tesla]
module single_domain(hx, hy, M ) ;
```

```
input hx, hy ; // magnetic field vector components
inout M ; // magnetization angle and torque
sig_flow_H hx, hy ; // port discipline for H-field vector components
rotational M ; // port discipline for magnetization angle
parameter real Area = 14.14e-14 ;// [m^2] surface area (PI*a*b)
parameter real thickness = 3.0e-9 ;// [m]
parameter real Ms = 8e5; // saturation magnetization [A/m]
parameter real Ku = 500; // uniaxial anisotropy [J/m^3]
parameter real alpha = 0.02; // LLG damping factor [unitless]
parameter real M_ea = 0 ; // easy axis angle [rads]
analog begin

    // Torque due to applied field:
    Tau(M) <+ -`P_U0*Ms*Area*thickness*(H(hx)*sin(Theta(M))- H(hy)*cos(Theta(M)));

    // Torque due to crystalline anisotropy energy:
    Tau(M) <+ -Ku*Area*thickness*sin(2*(Theta(M)- M_ea)) ;

    //damping torque = angular velocity * damping :
    Tau(M) <+ -Area*thickness*ddt(Theta(M))* Ms/((alpha+1/alpha)*`P_gamma);

end
endmodule
```

Listing 4. Dipole Coupling module (dipole_coupling)

```
'include ''constants.vams''
'include ''disciplines.vams''
module dipole_coupling (M1,M2);
inout M1,M2; rotational M1,M2;
parameter real t1 = 3.0e-9; //thickness top [m]
parameter real t2 = 3.0e-9; //thickness top [m]
parameter real a1 = 300e-9; //length of long_axis top [m]
parameter real a2 = 300e-9; //length of long_axis bottom [m]
parameter real b1 = 150e-9; //length of short_axis top [m]
parameter real b2 = 150e-9; //length of short_axis bottom [m]
parameter real A1 = a1*b1*'M_PI; //top_area_ellipse [m^2]
parameter real A2 = a2*b2*'M_PI; //bottom_area_ellipse [m^2]
parameter real Ms = 8e5;
parameter real Ny1 = (2*t1/'M_PI)*1/b1;
parameter real Nx1 = (2*t1/'M_PI)*1/a1;
parameter real Ny2 = (2*t2/'M_PI)*1/b2;
parameter real Nx2 = (2*t2/'M_PI)*1/a2;
parameter real r = 0.2; //attenuation factor Hij/Hdi
parameter real J_12 = A1*t1*'P_U0*pow(Ms,2)*r/2; //dipole prefactor [J]
parameter real J_21 = A2*t2*'P_U0*pow(Ms,2)*r/2; //dipole prefactor [J]
analog begin

    Tau(M1) <+ J_12*(Ny1*sin(Theta(M1) - 'M_PI/4)*cos(Theta(M2) - 'M_PI/4)
    - Nx1*cos(Theta(M1) - 'M_PI/4)*sin(Theta(M2) - 'M_PI/4));

    Tau(M2) <+ J_21*(Ny2*cos(Theta(M1) - 'M_PI/ 4)*sin(Theta(M2) - 'M_PI/
    4) - Nx2*sin(Theta(M1) - 'M_PI/ 4)*cos(Theta(M2) - 'M_PI/4));

end
endmodule
```

Listing 5. Exchange coupling module (exchange)

```
'include ''constants.vams"
'include ''disciplines.vams"
module exchange (M1,M2);
inout M1,M2;
rotational M1,M2;
parameter real J = -1.8e-5; //Exchange coupling constant [J/m^2]
parameter real a1 = 300e-9; //length of long_axis top [m]
parameter real a2 = 300e-9; //length of long_axis bottom [m]
parameter real b1 = 150e-9; //length of short_axis top [m]
parameter real b2 = 150e-9; //length of short_axis bottom [m]
parameter real A1 = a1*b1*'M_PI; //top_area_ellipse [m^2]
parameter real A2 = a2*b2*'M_PI; //bottom_area_ellipse [m^2]
parameter real Ms = 8e5;
analog begin

    @(initial_step)begin

        Theta(M1) <+ 'M_PI/4; Theta(M2) <+ 'M_PI*5/4;

    end
    Tau(M1) <+ -A1*J*sin(Theta(M1) - Theta(M2));
    Tau(M2) <+ -A2*J*sin(Theta(M2) - Theta(M1));

end
endmodule
```

Listing 6. TMR module (tmr)

```
'include ''constants.vams''
'include ''disciplines.vams''
module tmr(M1,rp,rn);
input M1;
inout rp,rn;
rotational M1;
electrical rp,rn;
parameter real R_max = 1000; //High resistance [ohm]
parameter real R_min = 500; //Low resistance [ohm]
parameter real TMR = (R_max - R_min)/R_min;
parameter real M_ea; //Pinned angle = easy axis angle
parameter real Vh = 0.4; //Bias effect parameter [volts]
real BE; //bias effect value based on Vh
analog begin

    BE = 1 + pow((V(rp,rn)/Vh), 2);
    I(rp,rn) <+ V(rp,rn)/(R_min * (1 + 0.5 * (TMR/BE) (1 - cos(Theta(M1) -
    M_ea))));

end
endmodule
```

Listing 7. ToggleMRAM_bit [top level] (toggle_mram_top)

```
'define ANGLE_ABSTOL 1e - 6
'define ANGULAR_FORCE_ABSTOL 1e - 6
'include ''constants.vams''
'include ''disciplines.vams''
nature Magnetic_Induction

    abstol = 1e - 6;
    access = H;
    units = ''A/m'';

endnature
discipline sig_flow_H

    potential Magnetic_Induction;

enddiscipline
'define P_gamma 1.76e11 //Gyromagnetic const. [rad/s/tesla]
module toggle_mram_top (wlp, wln, blp, bln, rp, rn);

    inout wlp, wln, blp, bln, rp, rn;
    rotational M1, M2;
    electrical wlp, wln, blp, bln, rp, rn;
    sig_flow_H hx, hy;
    writeline WLbit (.inp(blp), .inn(bln), .hout(Hy));
    writeline WLword (.inp(wlp), .inn(wln), .hout(Hx));
    single_domain Top (.hx(Hx),.hy(Hy),.M(Mtop));
    single_domain Bottom (.hx(Hx),.hy(Hy),.M(Mbot));
    exchange X1 (.M1(Mtop),.M2(Mbot));
    dipole_coupling DC1 (.M1(Mtop),.M2(Mbot)); //Pinned layer is set inside
    TMR block as M_ea
    tmr MR1 (.M1(Mbot), .rp(MRv),.rn(ntest));

endmodule
```

Listing 8. 3D Single Domain module (sd_3d)

```
'include ''constants.vams''
'include ''disciplines.vams''
nature Magnetic_Induction

    abstol = 1e - 12;
    access = H;
    units = ''A/m'';

endnature
discipline sig_flow_H

    potential Magnetic_Induction;

enddiscipline
'define P_gamma 1.76e11 //Gyromagnetic const. [rad/s/tesla]
//-----------------------------------------
// Module sd_3d
//-----------------------------------------
module sd_3d(hx, hy, hz,Mpol,Maz,Mea );
input hx, hy, hz ;
inout Maz, Mpol, Mea ;
sig_flow_H hx, hy, hz, hMpol, hMaz ; // H-field vector components
rotational Mea, Maz, Mpol, Anis; // port discipline for easy axis angle and
// magnetization angles(spherical)
//----------- free layer parameters ---------------------------
parameter real a1 = 300e-9 ; // length of long_axis top [m]
parameter real b1 = 150e-9 ; // length of short_axis top [m]
parameter real Area = a1*b1*'M_PI ; // top_area_ellipse [m^2]
parameter real t1 = 3.0e-9 ; // [m]
parameter real Ms = 8e5 ; // saturation magnetization (A/m)
parameter real Ku = 300.0 ; // uniaxial anisotropy (J/m^3)
parameter real alpha = 0.02 ; // LLG damping factor (unitless)
parameter real Vol = Area*t1 ; // volume [m^3]
parameter real C1 = 1/(1+pow(alpha,2));
parameter real C2 ='P_U0*Vol*Ms ; // [wb*m] note: J/(wb*m) = A/m
parameter real G0 = 'P_gamma*'P_U0; // (1.76e11 Hz/T*1.26e-6 wb/Am) = [2.21e5
m/As]
```

```
parameter real Nx = 0.0182; //for NiFe [JAP97 10J901, McMichael & Stiles (2005)]
parameter real Ny = 0.0515;
parameter real Nz = 0.931;
// set easy axis vector components EA, in cart. coord.; |EA|=1
// EA with i,j,&k components has comp. value = 0.57735, 2 comps. => 0.707
parameter real EAi = 1;
parameter real EAj = 0;
parameter real EAk = 0;
real ThetaMpol, ThetaMaz, TauMpol,TauMaz ;
real Mi, Mj, Mk, u ;
real ddu_acos, dd_Anis, du_dMpol, du_dMaz;
//-------------------------------------------------
analog begin

    @(initial_step)begin

        Theta(Mpol) <+ 80*`M_PI/180 ; // [rad] start polar angle non-zero
        Theta(Maz) <+ 0*`M_PI/180 ; // [rad] start azimuth. angle non-
        zero
        $strobe("Mpol_init = %5.2f rad", Theta(Mpol) );
        $strobe("Maz_init = %5.2f rad", Theta(Maz) );

    end
    Theta(Mea) <+ 0; // use when not connected to "EA gnd" at higher level
    Mi = sin(Theta(Mpol))*cos(Theta(Maz));
    Mj = sin(Theta(Mpol))*sin(Theta(Maz));
    Mk = cos(Theta(Mpol));
    //*************************************************************
    u = (EAi*Mi)+(EAj*Mj)+(EAk*Mk); //dot prod. of M and EA.
    //*************************************************************
    //-------------- Anistropy eqns ----------------------
    $strobe("u = %5.2f rad", u );
    Theta(Anis) <+ acos(u); // angle between M and EA:[M'dot'EA]=cos(u)
    ddu_acos = -1/sqrt(1-pow(u,2));
    du_dMpol = (EAi*cos(Theta(Mpol))*cos(Theta(Maz))

        + EAj*cos(Theta(Mpol))*sin(Theta(Maz))- EAk*sin(Theta(Mpol)));

    du_dMaz = sin(Theta(Mpol))*(EAj*cos(Theta(Maz)) - EAi*sin(Theta(Maz)));
    dd_Anis = Ku*Vol*sin(2*Theta(Anis));
    //-------------------------------------------------
    // Field components of angular velocity due to applied field, uniaxial
    // crystalline anisotropy and magnetostatic(shape) free energies:
```

```
//————————————————————————————————
//H(hMpol) = (dEa_dmpol + dEk_dmpol + dEd_dmpol) / C2 :
H(hMpol) <+ (H(hx)*cos(Theta(Mpol))*cos(Theta(Maz))

    + H(hy)*cos(Theta(Mpol))*sin(Theta(Maz))-H(hz)*sin(Theta(Mpol)))
    - (dd_Anis * ddu_acos * du_dMpol)/C2
    - Ms*sin(2*Theta(Mpol))*((Nx-Nz) + (Ny-Nx)*pow(sin(Theta(Maz)),2));

//H(hMaz)=(dEa_dmaz + dEk_dmaz + dEd_dmaz) / (C2*sin(Theta(Mpol))):

H(hMaz) <+ (H(hy)*cos(Theta(Maz)) - H(hx)*sin(Theta(Maz)))

    - (dd_Anis * ddu_acos * du_dMaz)/(C2*sin(Theta(Mpol)))
    - Ms*sin(Theta(Mpol))*sin(2*Theta(Maz))*(Ny-Nx);

//————————————————————————————————
// complete 3D dynamic equations in H(theta) and H(phi); integrate d(theta)/dt
and d(phi)/dt:
Theta(Mpol) <+ idt((C1*G0)*(H(hMaz) + alpha*H(hMpol)),1.396) ;
Theta(Maz) <+ idt(((C1*G0)/sin(Theta(Mpol)))*(alpha*H(hMaz)- H(hMpol)),0);
//————————————————————————————————
$strobe("Anis = %5.2f rad", Theta(Anis));
$strobe("Mpol_2 = %5.2f rad, Maz_2 = %5.2f rad",Theta(Mpol), Theta(Maz));

end
endmodule
```

Listing 9. 3D Single Domain module with STT (sd_3dstt)

```
'include ''constants.vams''
'include ''disciplines.vams''
nature Magnetic_Induction

    abstol = 1e - 12;
    access = H;
    units = ''A/m'';

endnature
discipline sig_flow_H

    potential Magnetic_Induction;

enddiscipline
'define P_gamma 1.76e11 //Gyromagnetic const. [rad/s/tesla]
'define P_hbar 1.054e-34 // Plancks const./2pi [J*s]
//-------------------------------------------
// Module sd_3dstt
//-------------------------------------------
module sd_3dstt (hx, hy, hz,Mpol,rp,rn,Maz,Mea );
input hx, hy, hz ;
inout rp, rn, Mea, Maz, Mpol ;
sig_flow_H hx, hy, hz, hMpol, hMaz ; // H-field vector components
rotational Mea, Maz, Mpol, Anis; // port discipline for easy axis angle and magnetization
angles(spherical)
electrical rp,rn ;
//----------- free layer parameters ----------------------------
parameter real a1 = 100e-9 ; // length of long_axis top [m]
parameter real b1 = 50e-9 ; // length of short_axis top [m]
parameter real Area = a1*b1*'M_PI ; // top_area_ellipse [m^2]
parameter real t1 = 3.0e-9 ; // [m]
parameter real Ms = 8e5 ; // saturation magnetization (A/m)
parameter real Ku = 300.0 ; // uniaxial anisotropy (J/m^3)
parameter real alpha = 0.02 ; // LLG damping factor (unitless)
parameter real Vol = Area*t1 ; // volume [m^3]
parameter real C1 = 1/(1+pow(alpha,2));
parameter real C2 ='P_U0*Vol*Ms ; // [wb*m] note: J/(wb*m) = A/m
```

```
parameter real G0 = `P_gamma*`P_U0; // (1.76e11 Hz/T*1.26e-6 wb/Am) = [2.21e5 m/As]
parameter real Nx = 0.0182; //for NiFe [JAP97 10J901, McMichael & Stiles (2005)]
parameter real Ny = 0.0515;
parameter real Nz = 0.931;
// set easy axis vector components EA, in cart. coord.; |EA|=1
// EA with i,j,&k components has comp. value = 0.57735, 2 comps. => 0.707
parameter real EAi = 0;
parameter real EAj = 0;
parameter real EAk = 1;
parameter real P = 0.35; // [unitless,~0.3-0.4 pg236 Bertotti] polarization factor
//—— reals for Magnetization and anisotropy field ———
real Mi, Mj, Mk, u, epoli, epolj, epolk, eazi, eazj, eazk ;
real ddu_acos, dd_Anis, du_dMpol, du_dMaz;
//——- reals for spin injection field, Hs ————————
real G, g, Is, Ff, Ffi, Ffj, Ffk ;
real dG_dMpol, dG_dMaz, dFf_dMpol, dFf_dMaz ;
//————————————————————————————————
analog begin

    @(initial_step)begin

        Theta(Mpol) <+ 179 * `M_PI/180; // intialize theta
        Theta(Maz) <+ 90 * `M_PI/180; // initialize phi
        $strobe("Mpol_init = %5.2f rad", Theta(Mpol) ); // print initial
        theta
        $strobe("Maz_init = %5.2f rad", Theta(Maz) ); // print initial phi

    end
    Theta(Mea) <+ 0; // use when not connected to gnd at higher level
    Mi = sin(Theta(Mpol))*cos(Theta(Maz));
    Mj = sin(Theta(Mpol))*sin(Theta(Maz));
    Mk = cos(Theta(Mpol));
    //************************************************************
    u = (EAi*Mi)+(EAj*Mj)+(EAk*Mk); // dot prod. of M and EA.
    //unit vector components in the theta(polar) and phi(azimuthal) directions:
    epoli = cos(Theta(Mpol))*cos(Theta(Maz));
    epolj = cos(Theta(Mpol))*sin(Theta(Maz));
    epolk = -sin(Theta(Mpol));
    eazi = -sin(Theta(Maz));
    eazj = cos(Theta(Maz));
    eazk = 0 ;
```

```
//************************************************************
// calculate the angle between Easy axis and M:
//————————- Anistropy eqns ————————————————
$strobe("u = %5.2f rad", u );
Theta(Anis) <+ acos(u); // angle between M and EA:[M'dot'EA]=cos(u)
ddu_acos = -1/sqrt(1-pow(u,2));
du_dMpol = (EAi*cos(Theta(Mpol))*cos(Theta(Maz))

    + EAj*cos(Theta(Mpol))*sin(Theta(Maz))- EAk*sin(Theta(Mpol)));

du_dMaz = sin(Theta(Mpol))*(EAj*cos(Theta(Maz)) - EAi*sin(Theta(Maz)));
dd_Anis = Ku*Vol*sin(2*Theta(Anis));
//—— functions and derivatives for spin injection field, Hs ——
g = (-4 + pow((1+P),3)*(3+u)/(4*pow(P,1.5))) ;
G = 1/g ;
// Ff = ep x M = -M x ep
Ffi = EAj*cos(Theta(Mpol)) - EAk*sin(Theta(Mpol))*sin(Theta(Maz)) ;
Ffj = -EAi*cos(Theta(Mpol)) + EAk*sin(Theta(Mpol))*cos(Theta(Maz)) ;
Ffk = EAi*sin(Theta(Mpol))*sin(Theta(Maz))


    - EAj*sin(Theta(Mpol))*cos(Theta(Maz)) ;
Ff = ( Ffi + Ffj + Ffk );
Is = I(rp,rn) ;
//————————————————————————————————
//Field components of angular velocity due to applied field, uniaxial crystalline
// anisotropy and magnetostatic(shape) free energies:
//————————————————————————————————
// H(hMpol) = (dEk_dmpol + dEs_dmpol + dEd_dmpol + dEa_dmpol )
/ C2
H(hMpol) <+ - (dd_Anis * ddu_acos * du_dMpol)/C2

    - ((Is*'P_hbar/(2*'P_Q*g*C2))*((epoli*Ffi)+(epolj*Ffj)+(epolk*Ffk)))
    - Ms*sin(2*Theta(Mpol))*((Nx-Nz) + (Ny-Nx)*pow(sin(Theta(Maz)),2))
    + ((H(hx)*cos(Theta(Mpol))*cos(Theta(Maz))
    + H(hy)*cos(Theta(Mpol))*sin(Theta(Maz))-H(hz)*sin(Theta(Mpol))))
    ;

//H(hMaz)=(dEk_dmaz + dEs_dmaz + dEd_dmaz + dEa_dmaz)*
// 1/ (C2*sin(Theta(Mpol)))
H(hMaz) <+ - (dd_Anis * ddu_acos * du_dMaz)/(C2*sin(Theta(Mpol)))

    - ((Is*'P_hbar/(2*'P_Q*g*C2))*((eazi*Ffi)+(eazj*Ffj)))
    - Ms*(Ny-Nx)*sin(Theta(Mpol))*sin(2*Theta(Maz))
    + (H(hy)*cos(Theta(Maz)) - H(hx)*sin(Theta(Maz))) ;
```

```
//————————————————————————————————
// complete 3D dynamic equations in H(theta) and H(phi); integrate d(theta)/dt
and d(phi)/dt:
//————————————————————————————————
Theta(Mpol) <+ idt((C1*G0)*(H(hMaz) + alpha*H(hMpol)),3.1239) ;
Theta(Maz) <+ idt(((C1*G0)/sin(Theta(Mpol)))*(alpha*H(hMaz)- H(hMpol)),1.57);
//————————————————————————————————
// view theta & phi
$strobe("Mpol_2 = %5.2f rad, Maz_2 = %5.2f rad", Theta(Mpol), Theta(Maz)
);
$strobe("————————————————————");

end
endmodule
```

Listing 10. 3D Magnetoresistive module (mr3d)

```
'include ''constants.vams''
'include ''disciplines.vams''
module mr3d(Mpol,Maz,rp,rn);
input Mpol,Maz ;
inout rp,rn ;
rotational Mpol,Maz,Mdiff ;
electrical rp,rn ;
real Mi, Mj, Mk, uMR;
// set easy axis vector components in cartesian coordinates:
parameter real EAi = 1;
parameter real EAj = 0;
parameter real EAk = 0;
parameter real R_max = 1000 ; // High resistance [ohm]
parameter real R_min = 500 ; // Low resistance [ohm]
analog begin

    Mi = sin(Theta(Mpol))*cos(Theta(Maz));
    Mj = sin(Theta(Mpol))*sin(Theta(Maz));
    Mk = cos(Theta(Mpol));
    uMR = (EAi*Mi)+(EAj*Mj)+(EAk*Mk); //dot prod. of M and EA.
    //————————- diff. angle between M and EA ————————
    Theta(Mdiff) <+ acos(uMR);
    //———- Calculate GMR with Mdiff ————————————
    V(rp,rn) <+ I(rp,rn)*(R_min+ 0.5*(R_max-R_min)*(1-cos(Theta(Mdiff))));

end
endmodule
```

Bibliography

[1] B. C. Choi, M. Belov, W. K. Hiebert, G. E. Ballentine, and M. R. Freeman. Ultrafast Magnetization Reversal Dynamics Investigated by Time Domain Imaging. *Physical Review Letters*, 86(4):728, January 2001.

[2] Cadence. Cadence Virtuoso Spectre Circuit Simulator, http://www.cadence.com.

[3] A. Fert, M. Baibich, J. Broto, N. Van Dau, F. Petroff, P. Eitenne, G. Creuzet, A. Friederich, and J. Chazelas. Giant magnetoresistance of (001)fe/(001)cr magnetic superlattices. *Phys. Rev. Lett.*, 61:2472, 1988.

[4] E. E. Fullerton and I. K. Schuller. The 2007 Nobel Prize in Physics: Magnetism and Transport at the Nanoscale. *ACS Nano*, 1(5):384 – 389, 2007.

[5] G. Binasch, P. Grünberg, F. Saurenbach, and W. Zinn. Enhanced magnetoresistance in layered magnetic structures with antiferromagnetic interlayer exchange. *Physical Review B*, 39(7):4828, March 1989.

[6] J. Lenz and A. S. Edelstein. Magnetic Sensors and Their Applications. *IEEE Sensors Journal*, 6(3):631–649, June 2006.

[7] A. Ney, C. Pampuch, R. Koch, and K. H. Ploog. Programmable computing with a single magnetoresistive element. *Nature*, 425(6957):485–487, October 2003.

[8] Hao Meng, Jianguo Wang, and Jian-Ping Wang. A spintronics full adder for magnetic CPU. *Electron Device Letters, IEEE*, 26(6):360–362, 2005.

[9] William C. Black and Bodhisattva Das. Programmable logic using giant-magnetoresistance and spin-dependent tunneling devices (invited). *Journal of Applied Physics*, 87(9):6674–6679, 2000.

[10] H. Dery, P. Dalal, L. Cywinski, and L. J. Sham. Spin-based logic in semiconductors for reconfigurable large-scale circuits. *Nature*, 447(7144):573–576, May 2007.

[11] J. M. Slaughter, R. W. Dave, M. Durlam, G. Kerszykowski, K. Smith, K. Nagel, B. Feil, J. Calder, M. DeHerrera, B. Garni, and S. Tehrani. High speed toggle MRAM with mgO-based tunnel junctions. Number 9071905, pages 873 – 876, 2005.

[12] Weisheng Zhao, Eric Belhaire, Claude Chappert, Bernard Dieny, and Guillaume Prenat. TAS-MRAM-Based Low-Power High-Speed Runtime Reconfiguration (RTR) FPGA. *ACM Transactions on Reconfigurable Technology and Systems (TRETS)*, 2:8:1–8:19, June 2009. ACM ID: 1534918.

[13] G. Prenat, M. El Baraji, Wei Guo, R. Sousa, L. Buda-Prejbeanu, B. Dieny, V. Javerliac, J.-P. NoziERES, Weisheng Zhao, and E. Belhaire. CMOS/Magnetic Hybrid Architectures. In *Electronics, Circuits and Systems, 2007. ICECS 2007. 14th IEEE International Conference on*, pages 190–193, 2007.

[14] J. C. Slonczewski. Theory of Magnetic Hysteresis in Films and Its Application to Computers. *IEEE Transactions on Magnetics*, 45(1):8–14, 2009.

[15] J. Z. Sun. Spin-current interaction with a monodomain magnetic body: A model study. *Physical Review B*, 62(1):570–578, July 2000.

[16] Z. Li and S. Zhang. Magnetization dynamics with a spin-transfer torque. *Physical Review B*, 68(2):024404, July 2003.

[17] Jiang Xiao, A. Zangwill, and M. D. Stiles. Macrospin models of spin transfer dynamics. *Physical Review B*, 72(1):014446, July 2005.

[18] B. Das and W.C. Black. A generalized HSPICETM macro-model for pinned spin-dependent-tunneling devices. *Magnetics, IEEE Transactions on*, 35(5):2889–2891, 1999.

[19] B. Das, W.C. Black, and A.V. Pohm. Universal HSPICE macromodel for giant magnetoresistance memory bits. *Magnetics, IEEE Transactions on*, 36(4):2062–2072, 2000.

[20] Seungyeon Lee, Seungjun Lee, Hyungsoon Shin, and Daejung Kim. Advanced HSPICE Macromodel for Magnetic Tunnel Junction. *Japanese Journal of Applied Physics*, 44(No. 4B):2696–2700, 2005.

[21] Jonathan D. Harms, Farbod Ebrahimi, Xiaofeng Yao, and Jian-Ping Wang. SPICE Macromodel of Spin-Torque-Transfer-Operated Magnetic Tunnel Junctions. *IEEE Transactions on Electron Devices*, 57(6):1425–1430, 2010.

[22] Nano Science and Technology Institute. *Changing the Paradigm for Compact Model Integration in Circuit Simulators Using Verilog-A*, volume 2, 2003.

[23] J.B. Kammerer, L. Hebrard, M. Hehn, F. Braun, P. Alnot, and A. Schuhl. Compact modeling of a magnetic tunnel junction using VHDL-AMS: computer aided design of a two-axis magnetometer. In *Sensors, 2004. Proceedings of IEEE*, pages 1558–1561 vol.3, 2004.

[24] W. Zhao, E. Belhaire, Q. Mistral, C. Chapped, V. Javerliac, B. Dieny, and E. Nicolle. Macro-model of Spin-Transfer Torque based Magnetic Tunnel Junction device for hybrid Magnetic-CMOS design. In *Behavioral Modeling and Simulation Workshop, Proceedings of the 2006 IEEE International*, pages 40–43, 2006.

[25] Takeaki Sugimura, Jun Deguchi, Hoon Choi, Takeshi Sakaguchi, Hyuckjae Oh, Takafumi Fukushima, and Mitsumasa Koyanagi. Low-Power and High-Sensitivity Magnetoresistive Random Access Memory Sensing Scheme with Body-Biased Preamplifier. *Japanese Journal of Applied Physics*, 45(No. 4B):3321–3325, 2006.

[26] M. Madec, J.-B. Kammerer, F. Pregaldiny, L. Hebrard, and C. Lallement. Compact modeling of magnetic tunnel junction. In *Circuits and Systems and TAISA Conference, 2008. NEWCAS-TAISA 2008. 2008 Joint 6th International IEEE Northeast Workshop on*, pages 229–232, 2008.

[27] L.-B. Faber, Weisheng Zhao, J.-O. Klein, T. Devolder, and C. Chappert. Dynamic compact model of Spin-Transfer Torque based Magnetic Tunnel Junction (MTJ). In *Design & Technology of Integrated Systems in Nanoscal Era, 2009. DTIS '09. 4th International Conference on*, pages 130–135, 2009.

[28] M. Madec, J.-B. Kammerer, and L. Hébrard. Compact Modeling of a Magnetic Tunnel Junction—Part II: Tunneling Current Model. *Electron Devices, IEEE Transactions on*, 57(6):1416–1424, June 2010.

[29] B. Dieny, V. S. Speriosu, S. S. P. Parkin, B. A. Gurney, D. R. Wilhoit, and D. Mauri. Giant magnetoresistive in soft ferromagnetic multilayers. *Physical Review B*, 43(1):1297, January 1991.

[30] J. S. Moodera, Lisa R. Kinder, Terrilyn M. Wong, and R. Meservey. Large Magnetoresistance at Room Temperature in Ferromagnetic Thin Film Tunnel Junctions. *Physical Review Letters*, 74(16):3273, April 1995.

[31] Shinji Yuasa, Taro Nagahama, Akio Fukushima, Yoshishige Suzuki, and Koji Ando. Giant room-temperature magnetoresistance in single-crystal Fe/MgO/Fe magnetic tunnel junctions. *Nat Mater*, 3(12):868–871, December 2004.

[32] Stuart S. P. Parkin, Christian Kaiser, Alex Panchula, Philip M. Rice, Brian Hughes, Mahesh Samant, and See-Hun Yang. Giant tunnelling magnetoresistance at room temperature with MgO (100) tunnel barriers. *Nat Mater*, 3(12):862–867, December 2004.

[33] Chin-Lung Su, Chih-Wea Tsai, Cheng-Wen Wu, Chien-Chung Hung, Young-Shying Chen, Ding-Yeong Wang, Yuan-Jen Lee, and Ming-Jer Kao. Write Disturbance Modeling and Testing for MRAM. *Very Large Scale Integration (VLSI) Systems, IEEE Transactions on*, 16(3):277–288, 2008.

[34] M. Durlam, D. Addie, J. Akerman, B. Butcher, P. Brown, J. Chan, M. DeHerrera, B.N. Engel, B. Feil, G. Grynkewich, J. Janesky, M. Johnson, K. Kyler, J. Molla, J. Martin, K. Nagel, J. Ren, N.D. Rizzo, T. Rodriguez, L. Savtchenko, J. Salter, J.M. Slaughter, K. Smith, J.J. Sun, M. Lien, K. Papworth, P. Shah, W. Qin, R. Williams, L. Wise, and S. Tehrani. A 0.18 um 4Mb toggling MRAM. In *Electron Devices Meeting, 2003. IEDM '03 Technical Digest. IEEE International*, pages 34.6.1–34.6.3, 2003.

[35] D. C. Worledge. Spin flop switching for magnetic random access memory. *Applied Physics Letters*, 84(22):4559, 2004.

[36] D. C. Worledge. Single-domain model for toggle MRAM. *IBM J Res 'l&' Dev*, 50(1):69–79, 2006.

[37] B. N. Engel, J. Akerman, B. Butcher, R. W. Dave, M. DeHerrera, M. Durlam, G. Grynkewich, J. Janesky, S. V. Pietambaram, N. D. Rizzo, J. M. Slaughter, K. Smith, J. J. Sun, and S. Tehrani. A 4-Mb Toggle MRAM Based on a Novel Bit and Switching Method. *IEEE Transactions on Magnetics*, 41(1):132–136, January 2005.

[38] J. A. Katine, F. J. Albert, R. A. Buhrman, E. B. Myers, and D. C. Ralph. Current-Driven Magnetization Reversal and Spin-Wave Excitations in Co /Cu /Co Pillars. *Physical Review Letters*, 84(14):3149–3152, April 2000.

[39] M. Tsoi, A. G. M. Jansen, J. Bass, W.-C. Chiang, M. Seck, V. Tsoi, and P. Wyder. Excitation of a Magnetic Multilayer by an Electric Current. *Physical Review Letters*, 80(19):4281, May 1998.

[40] R. H. Koch, J. A. Katine, and J. Z. Sun. Time-Resolved Reversal of Spin-Transfer Switching in a Nanomagnet. *Physical Review Letters*, 92(8):088302, February 2004.

[41] Alexey A. Kovalev, Arne Brataas, and Gerrit E. W. Bauer. Spin transfer in diffusive ferromagnet-normal metal systems with spin-flip scattering. *Physical Review B*, 66(22):224424, December 2002.

[42] E. B. Myers, D. C. Ralph, and et al. J. A. Katine. Current-induced switching of domains in magnetic multilayer devices. *Science*, 285:867–870, August 1999.

[43] M. Tsoi, A. G. M. Jansen, J. Bass, W.-C. Chiang, V. Tsoi, and P. Wyder. Generation and detection of phase-coherent current-driven magnons in magnetic multilayers. *Nature*, 406(6791):46–48, July 2000.

[44] S. I. Kiselev, J. C. Sankey, I. N. Krivorotov, N. C. Emley, R. J. Schoelkopf, R. A. Buhrman, and D. C. Ralph. Microwave oscillations of a nanomagnet driven by a spin-polarized current. *Nature*, 425(6956):380–383, September 2003.

[45] Haiwen Xi and Zhi Lin. In-plane magnetization dynamics driven by spin-polarized currents in magnetic nanostructures. *Physical Review B*, 70(9):092403, 2004.

[46] I. N. Krivorotov, N. C. Emley, J. C. Sankey, S. I. Kiselev, D. C. Ralph, and R. A. Buhrman. Time-Domain Measurements of Nanomagnet Dynamics Driven by Spin-Transfer Torques. *Science*, 307(5707):228–231, January 2005.

[47] F. Tabrizi. The future of scalable STT-RAM as a universal embedded memory. *EE Times Design (online)*, February 2007.

[48] R. C. O'Handley. *Modern Magnetic Materials: Principles and Applications*. Wiley-Interscience, 1999.

[49] J. F. Nye. *Physical Properties of Crystals - Their Representation by Tensors and Matrices*. Oxford University Press, 2 edition, July 1985.

[50] J. C. Slater. Cohesion in Monovalent Metals. *Physical Review*, 35(5):509–529, March 1930.

[51] W. H. Meiklejohn and C. P. Bean. New Magnetic Anisotropy. *Physical Review*, 102(5):1413, June 1956.

[52] S. S. P. Parkin, N. More, and K. P. Roche. Oscillations in exchange coupling and magnetoresistance in metallic superlattice structures: Co/Ru, Co/Cr, and Fe/Cr. *Physical Review Letters*, 64(19):2304, May 1990.

[53] M. D. Stiles. Interlayer exchange coupling. *cnst.nist.gov/epg/Pubs/pdf/epg734.pdf*, page 32, 2002.

[54] M. D. Stiles. Interlayer exchange coupling. *Journal of Magnetism and Magnetic Materials*, 200(1-3):322–337, October 1999.

[55] M. Julliere. Tunneling between ferromagnetic films. *Physics Letters A*, 54(3):225–226, September 1975.

[56] S. S. P. Parkin, R. Bhadra, and K. P. Roche. Oscillatory magnetic exchange coupling through thin copper layers. *Physical Review Letters*, 66(16):2152, April 1991.

[57] S. Ikeda, J. Hayakawa, Y. Ashizawa, Y. M. Lee, K. Miura, H. Hasegawa, M. Tsunoda, F. Matsukura, and H. Ohno. Tunnel magnetoresistance of 604diffusion in CoFeB/MgO/CoFeB pseudo-spin-valves annealed at high temperature. *Applied Physics Letters*, 93(8):082508, 2008.

[58] S. S. P. Parkin. Dramatic enhancement of interlayer exchange coupling and giant magnetoresistance in Ni81Fe19/Cu multilayers by addition of thin Co interface layers. *Applied Physics Letters*, 61(11):1358–1360, September 1992.

[59] Ph. Mavropoulos, N. Papanikolaou, and P. H. Dederichs. Complex Band Structure and Tunneling through Ferromagnet /Insulator /Ferromagnet Junctions. *Physical Review Letters*, 85(5):1088, July 2000.

[60] W.H. Butler, X.-G. Zhang, S. Vutukuri, M. Chshiev, and T.C. Schulthess. Theory of tunneling magnetoresistance for epitaxial systems. *Magnetics, IEEE Transactions on*, 41(10):2645–2648, October 2005.

[61] W. F. Brinkman. Tunneling Conductance of Asymmetrical Barriers. *Journal of Applied Physics*, 41(5):1915, 1970.

[62] John G. Simmons. Generalized Formula for the Electric Tunnel Effect between Similar Electrodes Separated by a Thin Insulating Film. *Journal of Applied Physics*, 34(6):1793, 1963.

[63] Fei fei Li. Bias dependent tunneling in ferromagnetic junctions and inversion of the tunneling magnetoresistance from a quantum mechanical point of view. *Journal of Applied Physics*, 95(11):7243, 2004.

[64] M. C. Hickey and J. S. Moodera. Origin of Intrinsic Gilbert Damping. *Physical Review Letters*, 102(13):137601, March 2009.

[65] T.L. Gilbert. A phenomenological theory of damping in ferromagnetic materials. *Magnetics, IEEE Transactions on*, 40(6):3443–3449, 2004.

[66] J. C. Slonczewski. Conductance and exchange coupling of two ferromagnets separated by a tunneling barrier. *Physical Review B*, 39(10):6995–7002, April 1989.

[67] L. Berger. Emission of spin waves by a magnetic multilayer traversed by a current. *Physical Review B*, 54(13):9353–9358, October 1996.

[68] J. C. Slonczewski. Current-driven excitation of magnetic multilayers. *Journal of Magnetism and Magnetic Materials*, 159(1-2):L1 – L7, June 1996.

[69] J. C. Slater. Electronic Structure of Alloys. *Journal of Applied Physics*, 8(6):385, 1937.

[70] R. M. Bozorth. Atomic Moments of Ferromagnetic Alloys. *Physical Review*, 79(5):887, 1950.

[71] W. Li, Y. Sun, and C. R. Sullivan. High-Frequency Resistivity of Soft Magnetic Granular Films. *IEEE Transactions on Magnetics*, 41(10):3283–3285, October 2005.

[72] S. Ohnuma, H. Fujimori, S. Mitani, and T. Masumoto. High-frequency magnetic properties in metal–nonmetal granular films (invited). *Journal of Applied Physics*, 79(8):5130, 1996.

[73] Li Gao, Xin Jiang, See-Hun Yang, J. D. Burton, Evgeny Y. Tsymbal, and Stuart S. P. Parkin. Bias Voltage Dependence of Tunneling Anisotropic Magnetoresistance in Magnetic Tunnel Junctions with MgO and Al_2O_3 Tunnel Barriers. *Physical Review Letters*, 99(22):226602, November 2007.

[74] W. F. Brown. *Micromagnetics*. New York, Interscience Publishers, 1963.

[75] M. C. Hickey. Analytical solution of the equation of motion for a rigid domain wall in a magnetic material with perpendicular anisotropy. *Physical Review B*, 78(18):180412, November 2008.

[76] H. Fujiwara, S.-Y. Wang, and M. Sun. Critical-field curves for switching toggle mode magnetoresistance random access memory devices (invited). *Journal of Applied Physics*, 97(10):10P507, 2005.

[77] S.-Y. Wang and H. Fujiwara. Orthogonal shape/intrinsic anisotropy toggle-mode magnetoresistance random access memory. *Journal of Applied Physics*, 98(2):024510, 2005.

[78] L. Landau and E. Lifshitz. Theory of the dispersion of magnetic permeability in ferromagnetic bodies. *Phys. Z. Sowjetunion*, 8:153, 1935.

[79] C. J. Garcia-Cervera and E. Weinan. Effective dynamics for ferromagnetic thin films. *Journal of Applied Physics*, 90(1):370–374, July 2001.

[80] R. V. Kohn and V. V. Slastikov. Effective dynamics for ferromagnetic thin films: a rigorous justification. *Proceedings of the Royal Society A*, 461:143 – 154, 2005.

[81] P. R. Gillette and K. Oshima. Magnetization Reversal by Rotation. *Journal of Applied Physics*, 29(3):529–531, 1958.

[82] D. Cimpoesu, A. Stancu, and L. Spinu. The reversible susceptibility tensor of synthetic antiferromagnets. *Journal of Applied Physics*, 101(09D112):1–3, 2007.

[83] R. D. McMichael and M. D. Stiles. Magnetic normal modes of nanoelements. *Journal of Applied Physics*, 97(10):10J901, 2005.

[84] J. C. Slonczewski. Excitation of spin waves by an electric current. *Journal of Magnetism and Magnetic Materials*, 195(2):261 – 268, May 1999.

[85] J. Z. Sun. Spin angular momentum transfer in current-perpendicular nanomagnetic junctions. *IBM Journal of Research and Development*, 50(1):81–100, January 2006.

[86] Jiang Xiao, A. Zangwill, and M. D. Stiles. Boltzmann test of Slonczewski's theory of spin-transfer torque. *Physical Review B*, 70(17):172405, November 2004.

[87] Giorgio Bertotti, I. D. Mayergoyz, and Claudio Serpico. *Nonlinear magnetization dynamics in nanosystems*. Elsevier, 2009.

[88] E. C. Stoner and E. P. Wohlfarth. A mechanism of magnetic hysteresis in heterogeneous alloys. *Phil. Trans. R. Soc. London A*, 240(826):599 – 642, 1948.

[89] D. C. Worledge, P. L. Trouilloud, and W. J. Gallagher. Theory for symmetric toggle magnetic random access memory. *Applied Physics Letters*, 90(22):222506, 2007.

[90] Ya. B. Bazaliy. Precession states in planar spin-transfer devices: The effective one-dimensional approximation. *Physical Review B*, 76(14):140402, October 2007.

[91] K. Kundert and O. Zinke. *The Designer's Guide to Verilog-AMS*. The Designer's Guide. Springer, first edition, 2007.

[92] K. Kundert. *The Designer's Guide to SPICE and Spectre®*, volume 1995 of *The Designer's Guide Book Series*. Springer, first edition, 1995.

[93] D. C. Worledge. Magnetic phase diagram of two identical coupled nanomagnets. *Applied Physics Letters*, 84(15):2847, 2004.

[94] Charles Kittel. *Introduction to Solid State Physics*. Wiley, eighth edition, 2005.

[95] J.-B. Kammerer, M. Madec, and L. Hébrard. Compact Modeling of a Magnetic Tunnel Junction—Part I: Dynamic Magnetization Model. *Electron Devices, IEEE Transactions on*, 57(6):1408–1415, June 2010.

[96] A. Jander, L. Engelbrecht, and P. Dhagat. Dynamic verilog-a model of a magnetoresistive spin valve. In *IEEE International conference on Behavioral Modeling and Simulation (BMAS08)*, pages 50–54. IEEE, September 2008.

[97] L. Engelbrecht, A. Jander, P. Dhagat, and M. Hall. A toggle mram bit modeled in verilog-a. *Solid-State Electronics*, 54:1135–1142, July 2010.